JOURNAL OF PETROLOGY

Journal of Petrology, 2021, Vol. 62, No. 9, 1–41
doi: 10.1093/petrology/egab043
Advance Access Publication Date: 29 May 2021
Original Manuscript

OXFORD

The Generation of Arc Andesites and Dacites in the Lower Crust of a Cordilleran Arc, Fiordland, New Zealand

Kendra Carty[1], Joshua J. Schwartz[1]*, John Wiesenfeld[1], Keith A. Klepeis[2], Harold H. Stowell[3], Andy J. Tulloch[4] and Calvin G. Barnes[5]

[1]Department of Geological Sciences, California State University Northridge, Northridge, CA 91330, USA; [2]Department of Geology, The University of Vermont, Burlington, VT 05405, USA; [3]Department of Geological Sciences, University of Alabama, Tuscaloosa, AL 35487, USA; [4]GNS Science, Private Bag 1930, Dunedin, New Zealand; [5]Department of Geosciences, Texas Tech University, Lubbock, TX 79409, USA

*Corresponding author. Telephone: 818-677-5813. E-mail: joshua.schwartz@csun.edu

Received 22 August 2020; Accepted 23 May 2021

ABSTRACT

We present microbeam major- and trace-element data from 14 monzodiorites collected from the Malaspina Pluton (Fiordland, New Zealand) with the goal of evaluating processes involved in the production of andesites in lower arc crust. We focus on relict igneous assemblages consisting of plagioclase and amphibole with lesser amounts of clinopyroxene, orthopyroxene, biotite and quartz. These relict igneous assemblages are heterogeneously preserved in the lower crust within sheeted intrusions that display hypersolidus fabrics defined by alignment of unstrained plagioclase and amphibole. Trace-element data from relict igneous amphiboles in these rocks reveal two distinct groups: one relatively enriched in high field strength element concentrations and one relatively depleted. The enriched amphibole group has Zr values in the range of ~25–110 ppm, Nb values of ~5–32 ppm, and Th values up to 2·4 ppm. The depleted group, in contrast, shows Zr values <35 ppm and Nb values <0·25 ppm, and Th is generally below the level of detection. Amphibole crystallization temperatures calculated from major elements range from ~960 to 830 °C for all samples in the pluton; however, we do not observe significant differences in the range of crystallization temperatures between enriched (~960–840 °C) and depleted groups (~940–830 °C). Bulk-rock Sr and Nd isotopes are also remarkably homogeneous and show no apparent difference between enriched ($\varepsilon Nd_i = 0{\cdot}1$ to –0·1; $^{87}Sr/^{86}Sr_i = 0{\cdot}70420$–$0{\cdot}70413$) and depleted groups ($\varepsilon Nd_i = 0{\cdot}3$ to –0·4; $^{87}Sr/^{86}Sr_i = 0{\cdot}70424$–$0{\cdot}70411$). Calculated amphibole-equilibrium melt compositions using chemometric equations indicate that melts were highly fractionated (molar Mg# <50), andesitic to dacitic in composition, and were much more evolved than bulk lower continental crust or primitive basalts and andesites predicted to have formed from hydrous melting of mantle-wedge peridotite beneath an arc. We suggest that melts originated from a common, isotopically homogeneous source beneath the Malaspina Pluton, and differences between enriched and depleted trace-element groups reflect varying contributions from subducted sediment-derived melt and sediment-derived fluid, respectively. Our data demonstrate that andesites and dacites were the dominant melts that intruded the lower crust, and their compositions mirror middle and upper bulk-continental crust estimates. Continental crust-like geochemical signatures were acquired in the source region from interaction between hydrous mantle-wedge melts and recycled subducted sediment rather than assimilation and/or remelting of pre-existing lower continental crust.

Key words: MASH zone; hot zone; Cordilleran arc; amphibole; lower crust; and esite

INTRODUCTION

Modern petrological studies of magmatic reservoirs in continental arcs show that they are complex regions of melt, volatiles, and crystals, and when magmatism is robust, they can form transcrustal networks of mush-rich (crystals + melt) and melt-rich reservoirs that are widely distributed from the lower to upper crust (Fig. 1) (Cashman *et al.*, 2017; Edmonds *et al.*, 2019). Magma chambers are particularly important because they are the primary locations where continental crust is constructed via the geochemical diversification of primitive arc melts into more felsic compositions (Taylor & McLennan, 1985, 1995; Rudnick, 1995; Kelemen, 1995; Hawkesworth & Kemp, 2006; Kelemen *et al.*, 2014). In a pioneering study, Hildreth & Moorbath (1988) proposed that geochemical diversification occurred primarily at the crust–mantle boundary where intracrustal remelting functions to chemically enrich depleted mantle-wedge melts. Since its inception in the late 1980s, the so-called 'MASH' ('Melting, Assimilation, Storage, and Homogenization') zone hypothesis has had a profound impact on volcanological, petrological, and tectonic thinking regarding the evolution of continental arc systems, and it is commonly invoked to explain the geochemical and isotopic diversification of magmas in continental arcs.

In more recent numerical simulations and field observations of lower arc crust, the efficiency of intracrustal melting as a primary mechanism for melt diversification has been challenged (Bergantz, 1992; Petford & Gallagher, 2001; Dufek & Bergantz, 2005; Annen *et al.*, 2006; Solano *et al.*, 2012; Walker *et al.*, 2015). Numerical studies in particular have emphasized that fractional crystallization is a dominant process in the differentiation of arc melts, and the efficiency of intracrustal melting depends on a number of factors such as the H_2O content of the parental basalt, emplacement rate, emplacement style, and the composition of the surrounding crust (lower-crustal amphibolite, upper-crustal graywacke, etc.) (Solano *et al.*, 2012). In addition, field studies commonly document little evidence for intracrustal partial melting in the lower crust (Allibone *et al.*, 2009*a*; Walker *et al.*, 2015); consequently, other processes have been invoked to produce lower-crustal melts with continental crust geochemical characteristics such as crustal contributions from delaminated lower-crustal rocks (Ducea *et al.*, 2017), melting of relaminated subducted sediments (Plank, 2005; Hacker *et al.*, 2011), and/or interaction with enriched mantle reservoirs (Pearce, 1983; Hawkesworth *et al.*, 1990; Gazel *et al.*, 2015; Turner *et al.*, 2017).

In addition to problems with understanding the geochemical diversification of lower-crustal MASH zones, we also know relatively little about the architecture of lower-crustal melt-storage regions in arcs, the mechanisms by which melts were emplaced, and the degree of homogenization that occurs in the lower crust. Studies of shallow to mid-crustal plutons have recognized that magma reservoirs are constructed by incremental injections of multiple compositionally diverse magma pulses (e.g. Bergantz, 2000; Glazner *et al.*, 2004; Memeti *et al.*, 2010; Miller *et al.*, 2011; Caricchi *et al.*, 2012; Coint *et al.*, 2013*a*, 2013*b*; Barboni *et al.*, 2015; Barnes *et al.*, 2016*a*, 2016*b*, 2017; Paterson *et al.*, 2016), and studies of lower-crustal magma reservoirs indicate that melts are assembled in a similar fashion, by incremental emplacement of magma batches that range up to 2 km thick (Klepeis *et al.*, 2016). The growth of magma reservoirs by incremental injection raises a number of questions about the fate of melts entering the lower crust and the processes that result in their homogenization and diversification. For example, are individual magma batches related to one another and derived from the same source, or are they chemically distinct and require distinct sources and/or reservoirs? Do magma batches follow similar chemical diversification trends, and what MASH or hot zone processes are dominantly responsible for magma evolution (e.g. crustal assimilation and melting, fractional crystallization, and/or magma mixing)? To what degree do individual magma batches chemically communicate, and is there evidence for kilometer-scale magma mixing or is mixing localized to individual 100 m thick (or less) magma batches? Finally, to what degree do open-system processes including recharge, rejuvenation of cumulates, and melt extraction affect the magmatic evolution of lower arc crust? Understanding the answers to these questions is important for evaluating how arc magmas diversify and how continental crust is created in the roots of arcs.

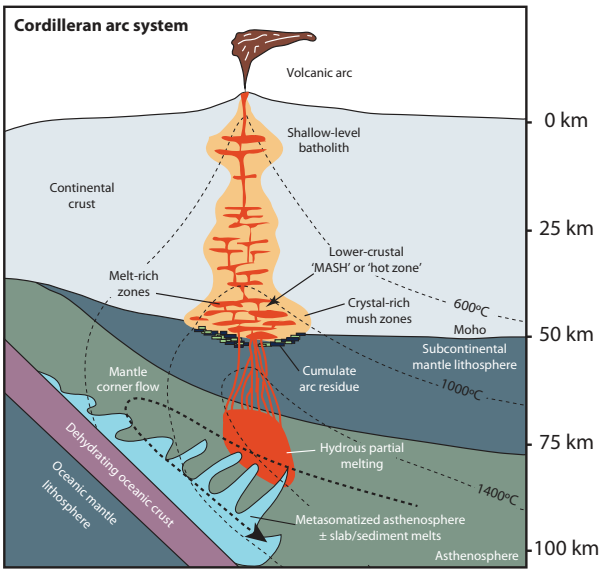

Fig. 1. Schematic cross-section of a Cordilleran arc system illustrating a transcrustal magma system that extends from the lower to upper crust. Magmatism throughout the crust consists of melt-rich regions (red) and mush-rich (crystal + melt) regions (yellow). This study focuses on geochemical diversification in lower arc crust. Modified after Winter (2001) and Cashman *et al.* (2017).

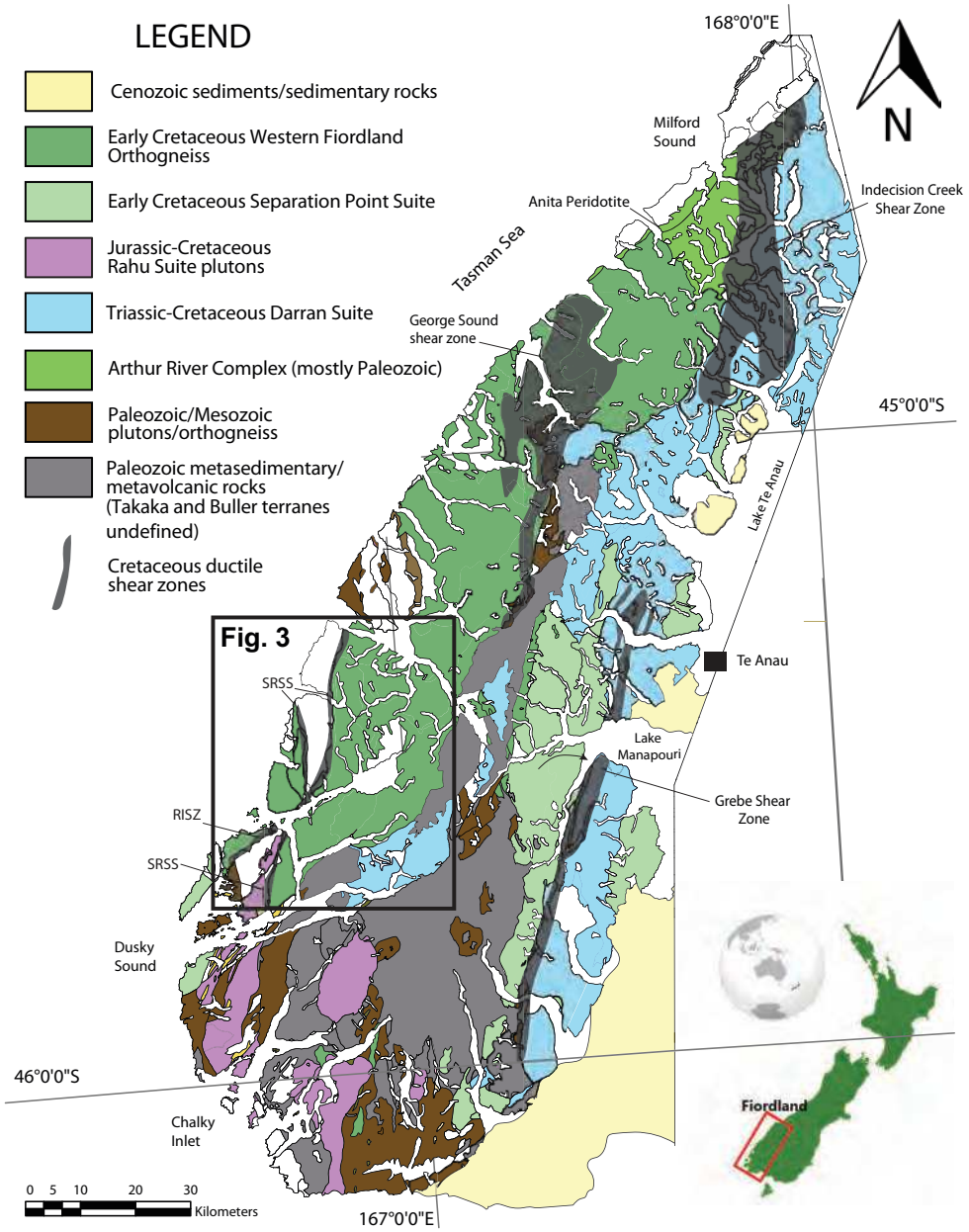

Fig. 2. Geological map of Fiordland [adapted from Turnbull *et al.* (2010) and Buriticá *et al.* (2019)]. The lower crust of the Median Batholith is indicated by the Western Fiordland Orthogneiss and Arthur River Complex (dark green). Box shows location of Malaspina Pluton (Fig. 3). Inset shows location of Fiordland in New Zealand. SRSS, Straight River shear zone; RISZ, Resolution Island shear zone.

Here, we examine the Malaspina Pluton (Fiordland, New Zealand), which is exposed over ~550 km^2 and represents the exhumed lower-crustal portion of a continental arc emplaced at ~40 km paleodepth (Figs 2 and 3) (Allibone *et al.*, 2009*a*, 2009*b*; De Paoli *et al.*, 2009; Stowell *et al.*, 2014, 2017). We use prior field mapping of igneous structures (Klepeis *et al.*, 2016) and igneous amphibole geochemistry to investigate the diversification of melts in lower arc crust as well as the physical and chemical architecture of a lower-crustal magma reservoir system. Our results demonstrate that a broad spectrum of andesitic to dacitic melts were emplaced into the lower crust and their compositions mirror middle to upper continental crust estimates. Fractionation at the level of emplacement was minor and we see little evidence for mixing between individual melt sheets during pluton construction. Whereas melts were not well homogenized in terms of major or trace elements, they are indistinguishable in terms of Sr and Nd isotopes. We propose that isotopic signatures of the melts

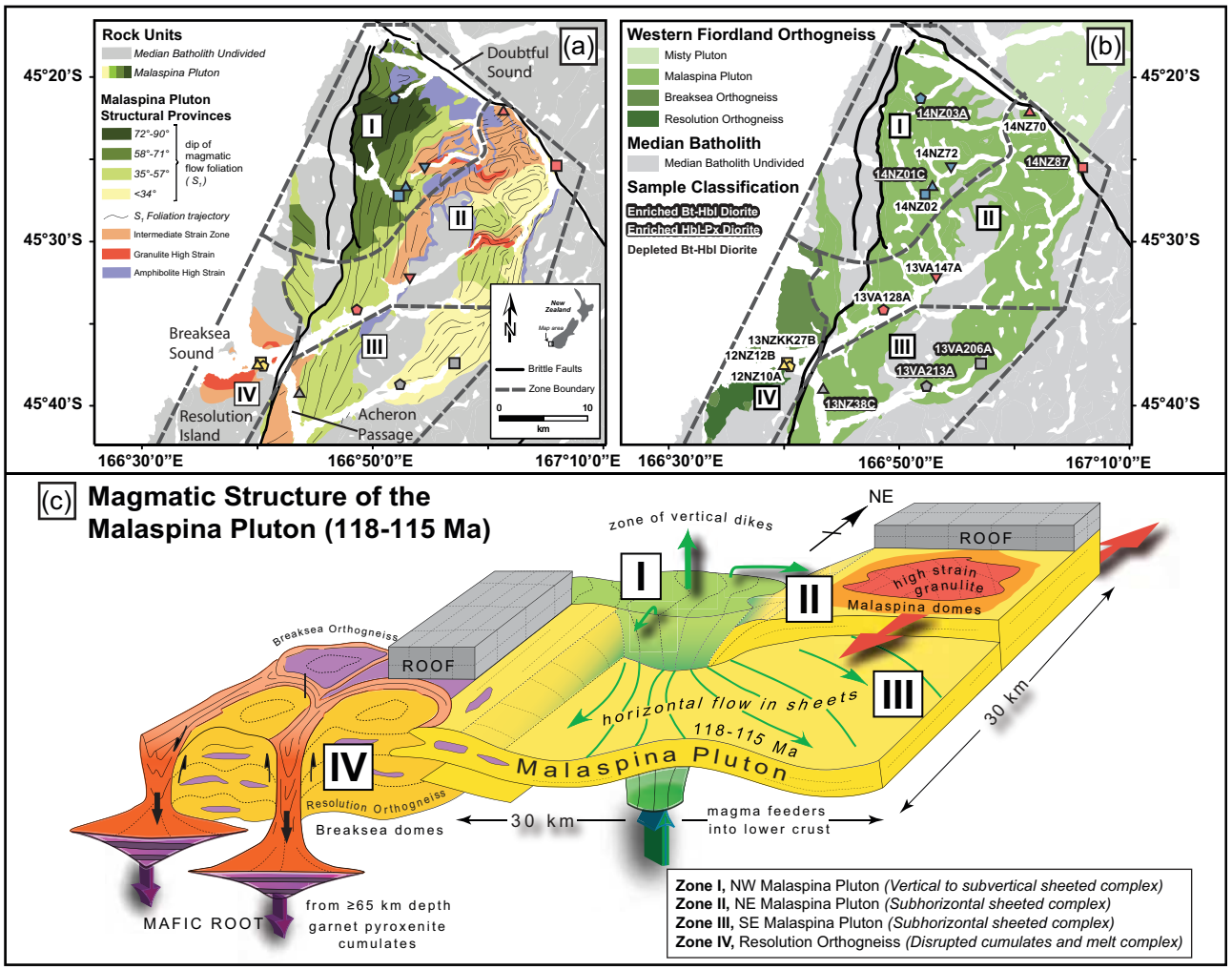

Fig. 3. Structure within the Malaspina Pluton from Klepeis *et al.* (2016). (a) Magmatic domains of the Malaspina Pluton. Steep foliations (>58°) occur in the NW, whereas shallower foliations characterize the NE and SE domains. Magmatic fabrics are overprinted by granulite (red or pink) and amphibolite (purple) high- and intermediate-strain zones. Dashed black lines show the four magmatic zones. (b) Map of the Malaspina Pluton identifying sample collection locations. (c) Three-dimensional schematic illustration showing the magmatic domains during construction of the Malaspina Pluton. The 6 km wide feeder zone (green) and subhorizontal sheets (yellow) should be noted.

were acquired in the source region through mixing between a hydrous mantle wedge melt and sediment-derived fluids and melts.

GEOLOGICAL BACKGROUND

The Malaspina Pluton, a deep-crustal melt reservoir

The Malaspina Pluton is located within the lower crust of the Median Batholith, which encompasses 10 000 km^2 of arc crust and was part a large continental-margin subduction system that extended from Gondwana to Laurentia in the Mesozoic (Mortimer *et al.*, 1999; Tulloch & Kimbrough, 2003). The lower crust of the Median Batholith is exposed in western Fiordland where it consists of Early Cretaceous mafic to intermediate gneisses and Paleozoic metasedimentary and meta-igneous host rocks (Allibone *et al.*, 2009*a*) (Fig. 2). Early Cretaceous lower-crustal arc rocks are dominated by the Western Fiordland Orthogneiss of the Separation Point Suite, and consist of variably metamorphosed diorite, monzodiorite, and minor gabbro emplaced and metamorphosed at 30–65 km depth (Oliver, 1977; 1980; Mattinson *et al.*, 1986; Bradshaw, 1989, 1990; Klepeis *et al.*, 2004, 2007; Allibone *et al.*, 2009*a*; De Paoli *et al.*, 2009; Stowell *et al.*, 2014).

The Western Fiordland Orthogneiss occupies over 2300 km^2 (more than half of the exposed lower crust) and consists of three large plutonic bodies including the Malaspina, Misty and Worsely Plutons as well as several other smaller bodies (Allibone *et al.*, 2009a). They were collectively emplaced during a brief, ~14 Myr 'flare-up' of high-Sr/Y (>40) magmas that lasted from 128 to 114 Ma and peaked at *c.* 118–115 Ma, during which time nearly 90 % of the Cretaceous lower crust was emplaced (Milan *et al.*, 2017; Schwartz *et al.*, 2017; Ringwood *et al.* in press). Allibone *et al.* (2009b)

provided a detailed description of these plutons and here we focus on the Malaspina Pluton (118–115 Ma) and associated rocks including the coeval Resolution Orthogneiss (115 Ma) and the slightly older, Breaksea Orthogneiss (124 Ma). The latter is unique in that it consists of interlayered garnet-granulite and garnet-pyroxenite and was metamorphosed deep within the arc at *c.* 1·8 GPa (De Paoli *et al.*, 2009; Klepeis *et al.*, 2016; Stowell *et al.*, 2017). Construction of these lower-crustal plutons was closely followed by heterogeneously distributed granulite- to amphibolite-facies metamorphism and crystal-plastic deformation at *c.* 112 Ma (De Paoli *et al.*, 2009; Stowell *et al.*, 2014; Klepeis *et al.*, 2016; Schwartz *et al.*, 2016).

Previous studies of the Western Fiordland Orthogneiss and more felsic granites of the Separation Point Suite have recognized that the Early Cretaceous magmatic surge was characterized by bulk-rocks with high Na, Al, Sr, and low Y concentrations, and these features have been interpreted to reflect either deep-crustal partial melting of a mafic, garnet-bearing arc root (McCulloch *et al.*, 1987; Muir *et al.*, 1995; Tulloch & Kimbrough, 2003; Milan *et al.*, 2017) or fractionation of igneous garnet from lower-crustal mafic melts (Chapman *et al.*, 2016). Geochemical modeling of bulk-rocks has also led to the interpretation that Mesozoic magmatism produced a thick, garnet-bearing arc root beneath Fiordland in the Early Cretaceous (McCulloch *et al.*, 1987; Muir *et al.*, 1995; Tulloch & Kimbrough, 2003; Chapman *et al.*, 2016; Milan *et al.*, 2017). Our data bear on these prior interpretations and we specifically investigate the role of garnet fractionation and discrepancies between amphibole-equilibrium melts and bulk-rocks in this study.

Characteristics of Malaspina Pluton

The Malaspina Pluton is one of the deepest and best-preserved igneous bodies in the lower crust of the Median Batholith (Fig. 2). The pluton spans >550 km^2 and consists of diorite, hornblende diorite, and monzodiorite with scarce hornblendite and garnet pyroxenite (Oliver, 1976, 1977, 1980; Allibone *et al.*, 2009*a*; Klepeis *et al.*, 2016). It was emplaced during *c.* 118–115 Ma and igneous assemblages consist primarily of hornblende + plagioclase + orthoclase + magnetite + ilmenite + apatite + zircon ± clinopyroxene ± orthopyroxene ± Ti-rich biotite (Mattinson *et al.*, 1986; Tulloch & Kimbrough, 2003; Hollis *et al.*, 2004; Klepeis *et al.*, 2007; Allibone *et al.*, 2009a; Klepeis *et al.*, 2016). Mapping of magmatic fabrics in the Malaspina Pluton reveals that it was assembled by numerous intrusions of dioritic sheets that were fed from a 6 km wide subvertical feeder zone (Zone I) from which melts mainly flowed east- and southeastward (Fig. 3a and c) (Klepeis *et al.*, 2016). Sheets of diorite are interlayered with rafts of metasedimentary rock, which are aligned parallel to the margins of the magmatic sheets (Klepeis *et al.*, 2016). In the feeder zone, located in the NW portion of the Pluton (Zone I in Fig. 3), steeply dipping magmatic foliations (>72–90°) record flow of magma from deeper structural levels. Zones II and III represent subhorizontal sheeted dioritic intrusions ranging from 100 m to 2 km thick that emanated from the subvertical feeder zone.

Zone IV is the most structurally complex portion and consists of coeval diorites and metadiorites, termed the Resolution Orthogneiss, which possess both hypersolidus and metamorphic foliations. The Resolution Orthogneiss intruded into a disrupted cumulate zone consisting of garnet-pyroxenite and plagioclase-rich garnet granulite, termed the Breaksea Orthogneiss (Allibone *et al.*, 2009*a*; De Paoli *et al.*, 2009; Klepeis *et al.*, 2016; Stowell *et al.*, 2017). Field and microstructural observations indicate that layering of garnet and clinopyroxenes in the Breaksea Orthogneiss reflects an original igneous cumulate fabric, and geochemical studies of garnets also support the interpretation that some of the garnets are igneous in origin as well (Clarke *et al.*, 2013). High-pressure/temperature metamorphism of the Breaksea Orthogneiss occurred at 1·8 GPa and was followed by decompression to 1·0–0·8 GPa prior to emplacement of the Resolution Orthogneiss and Malaspina Pluton at 118–115 Ma (De Paoli *et al.*, 2009; Clarke *et al.*, 2013; Chapman *et al.*, 2015; Klepeis *et al.*, 2016). Igneous rocks related to emplacement in this zone comprise steep-sided domes that also record vertical emplacement of magmas and entrainment of garnet-pyroxenite and related rocks from the Breaksea Orthogneiss (Betka & Klepeis, 2013). A 3-D diagram after Klepeis *et al.* (2016) shown in Fig. 3c illustrates these four magmatic zones and their relationship to assembly of this lower-crustal magmatic complex.

Host rocks to the Malaspina Pluton in Zones I–III consist of Deep Cove Gneiss, a heterogeneous assemblage of Late Neoproterozoic to Early Paleozoic quartzofeldspathic paragneiss, marble, calc-silicate, and hornblende–plagioclase gneiss (Oliver, 1980; Gibson, 1992). Less abundant orthogneisses are also present and consist of Late Devonian–late Carboniferous I-type and S-type granitic rocks ranging from 371 to 305 Ma (Tulloch *et al.*, 2009), and minor Ordovician orthogneiss (Gibson & Ireland, 1995). Magmatic contacts are exceedingly rare, but, where preserved, contact aureoles in metasedimentary host rocks are 500–1000 m wide and formed at conditions estimated at >750 °C and 1·0–1·5 GPa (Allibone *et al.*, 2009*b*).

In the southern portion of the Malaspina Pluton (west side of Zone III along Acheron Passage), the Malaspina Pluton includes rare, meter-scale xenoliths of garnet clinopyroxenite and hornblendite, which are probably rafts of the older Breaksea Orthogneiss (Oliver, 1980; Allibone *et al.*, 2009*a*; Chapman *et al.*, 2016). The rafts of garnet pyroxenite are cut by intrusions of the Malaspina Pluton (e.g. sample 13NZ38C), and indicate that garnet pyroxenites predated and are not genetically related to the Malaspina Pluton. Similar garnet pyroxenites occur as ultramafic lenses, layers,

Table 1: Summary of petrography

Sample	Zone	Rock type	Igneous mineral assemblage	Location
14NZ01C	I	Hbl–Px diorite	Plag, Opx, Cpx, Hbl, Ilm, Ap, Zrn	Dagg Sound
14NZ02	I	Bt–Hbl diorite	Plag, Hbl, Bt, Ilm, Ap, Zrn	Dagg Sound
14NZ03A	I	Hbl–Px diorite	Plag, Cpx, Hbl, Opx, Bt, Ilm, Ap, Zrn, Mag	First Arm
14NZ72	I	Bt–Hbl diorite	Plag, Hbl, Bt, Ilm, Ap, Zrn	Crooked Arm
14NZ70	II	Bt–Hbl diorite	Plag, Hbl, Bt, Ap, Ilm, Zrn	Doubtful Sound
14NZ87	II	Bt–Hbl diorite	Plag, Hbl, Bt, Cpx, Ilm, Ap, Zrn, Mag	Doubtful Sound
13VA128A	II	Bt–Hbl diorite	Plag, Hbl, Bt, Ilm, Ap, Zrn	Breaksea Sound
13VA147A	II	Bt–Hbl diorite	Plag, Hbl, Bt, Ilm, Ap, Zrn	Vancouver Arm
13NZ38C	III	Hbl–Px diorite	Plag, Cpx, Hbl, Bt, Ilm, Ap, Zrn	Acheron Passage
13VA206A	III	Hbl diorite	Plag, Hbl, Ilm, Bt, Ap, Zrn	Wet Jacket Arm
13VA213A	III	Hbl–Px diorite	Plag, Opx, Cpx, Hbl, Bt, Ilm, Ap, Zrn, Mag	Wet Jacket Arm
12NZ10A	IV	Hbl diorite	Hbl, Plag, Ap, Ilm, Zrn, Mag	Resolution Island
12NZ12B	IV	Bt–Hbl diorite	Plag, Hbl, Bt, Ap, Ilm, Zrn	Resolution Island
13NZKK27B	IV	Bt–Hbl diorite	Plag, Hbl, Bt, Ap, Ilm, Zrn	Resolution Island

Brief petrographic description of analyzed samples including textural descriptions and mineral assemblages observed. Mineral abbreviations after Whitney and Evans (2010); Hbl, hornblende; Px, pyroxene; Bt, biotite; Plag, plagioclase; Opx, orthopyroxene; Cpx, clinopyroxene; Ilm, ilmenite; Ap, apatite; Zrn, zircon; Mag, magnetite. Alignment refers to orientation of mafic minerals.

and pods in the Resolution Orthogneiss, suggesting that melts from both the Malaspina Pluton and Resolution Orthogneiss intruded and disrupted high-pressure cumulates of the Breaksea Orthogneiss during emplacement (Fig. 3c) (Allibone *et al.*, 2009*a*; De Paoli *et al.*, 2009).

Metamorphism of the Malaspina Pluton and Western Fiordland Orthogneiss commenced shortly after igneous emplacement and lasted until 102 Ma (Gibson & Ireland, 1995; Daczko *et al.*, 2001, 2002; Hollis *et al.*, 2004; Klepeis *et al.*, 2004, 2007, 2016; Clarke *et al.*, 2005; Betka & Klepeis, 2013; Stowell *et al.*, 2014, 2017; Miranda & Klepeis, 2016; Schwartz *et al.*, 2016). This phase of metamorphism led to local recrystallization of the Malaspina Pluton at granulite-facies (>800 °C, *c.* 1·2–1·4 GPa) and then upper amphibolite-facies conditions (550–600 °C, *c.* 0·7–0·9 GPa) during retrograde cooling (Klepeis *et al.*, 2007, 2016; De Paoli *et al.*, 2009; Stowell *et al.*, 2014, 2017; Schwartz *et al.*, 2016). Garnet granulite assemblages often form diffuse and gradational contacts with relict igneous assemblages and are characterized by porphyroblastic garnet commonly associated with trondhjemitic leucosomes (Clarke *et al.*, 2005; Stowell *et al.*, 2014). Both metamorphic events were accompanied by crystal-plastic deformation along distributed and localized shear zones. The distribution of granulitic (red) and amphibolitic (blue) high- and intermediate-strain zones is shown in Fig. 3a, and we specifically avoided sampling metamorphosed rocks and instead focused on the relict igneous assemblages.

METHODS

We divide the Malaspina Pluton into four magmatic zones based on the dip of magmatic foliations observed by Klepeis *et al.* (2016) (Fig. 3). The four zones are as follows: Zone I (Dagg Sound, Anchorage Arm, First Arm, and W. Crooked Arm), Zone II (N. Breaksea Sound, Vancouver Arm, E. Crooked Arm, and Hall Arm), Zone III (Acheron Passage, S. Breaksea Sound, Wet Jacket Arm, and Broughton Arm), and Zone IV (Resolution Island) (Table 1). We focus on relict igneous assemblages, which have been well documented by Klepeis *et al.* (2007, 2016). These relict igneous assemblages consist of plagioclase and amphibole with lesser amounts of clinopyroxene, orthopyroxene, biotite and quartz. Although the region has undergone high-grade metamorphism, relict igneous assemblages are heterogeneously preserved in the lower crust as sheeted intrusions with hypersolidus fabrics defined by alignment of unstrained plagioclase and amphibole. Thus, we focused on samples showing no obvious evidence of crystal-plastic deformation, microfaulting, hydrothermal alteration, or neomineralization. We also avoided samples showing microtextural evidence for melt–rock interaction such as extensive subsolidus deformation, recrystallization, and metamorphic overprints. In particular, we avoided any samples with probably metamorphic hornblende, which includes: (1) assemblages that include a combination of metamorphic garnet, clinozoisite, titanite and epidote; (2) hornblende grains and hornblende rims in reaction relationship with primary pyroxene grains (e.g. Smith, 2014); (3) hornblende grains associated with grain boundary melt–flux reactions as described by Stuart *et al.* (2017, 2018). Representative samples and textures are illustrated in Fig. 4.

Whole-rock geochemistry

Whole-rock samples were powdered in an alumina ceramic shatterbox at California State University, Northridge. Powders were mixed with a 2:1 ratio of SpectroMelt A10 lithium tetraborate flux and melted in graphite crucibles at 1000 °C for *c.* 20 min to create glass beads. Beads were re-powdered, re-fused following the initial melting parameters, and polished to remove carbon from the flat bottom where analysis occurs. Following procedures outlined by Lackey *et al.* (2012), glass beads were analyzed at Pomona College for major (SiO_2, TiO_2, Al_2O_3, Fe_2O_3, MnO, MgO, CaO, Na_2O, K_2O,

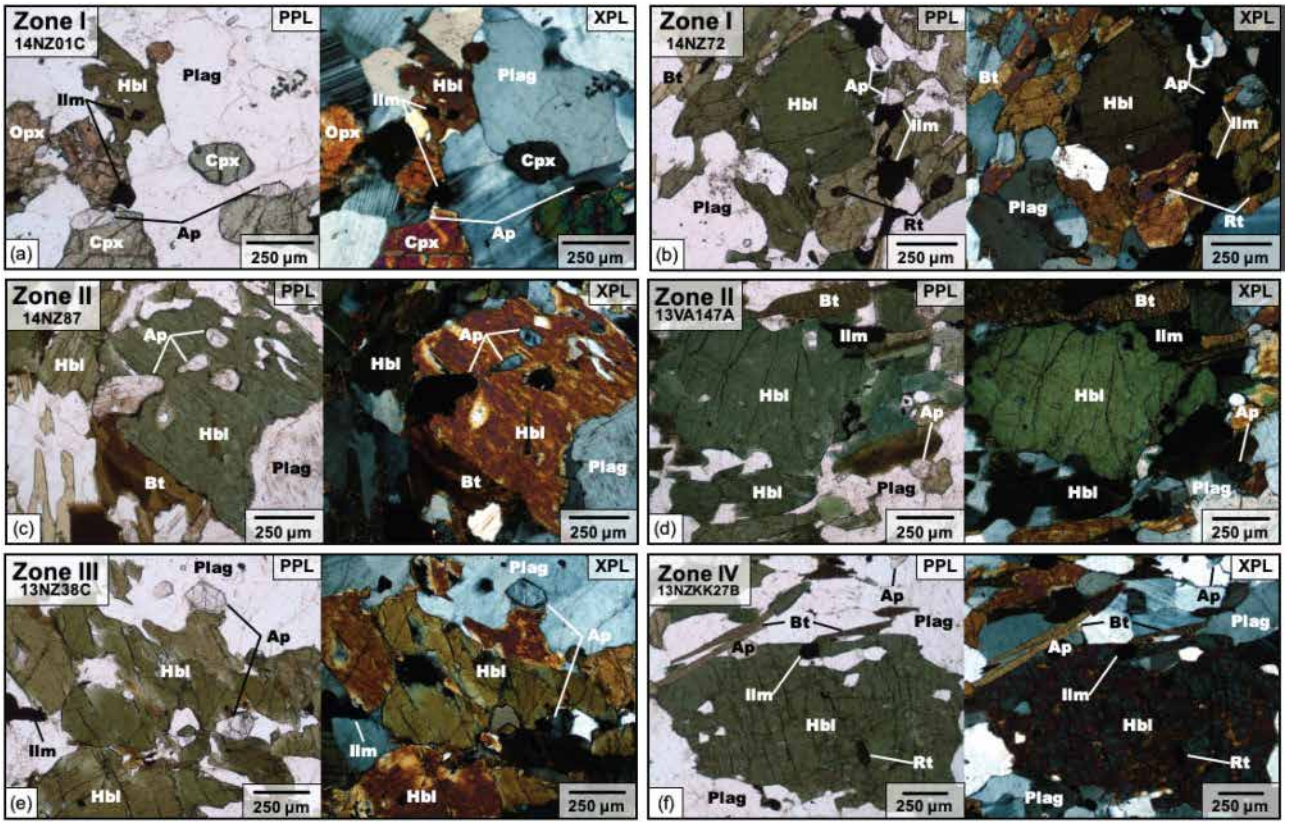

Fig. 4. Photomicrographs of representative samples from each zone demonstrating common mineral assemblages and textures in plane-polarized light (PPL; left) and cross-polarized light (XPL; right). Mineral abbreviations after Whitney & Evans (2010); Hbl, hornblende; Bt, biotite; Plag, plagioclase; Opx, orthopyroxene; Cpx, clinopyroxene; Ilm, ilmenite; Ap, apatite; Rt, rutile.

P_2O_5) and trace (Rb, Sr, Ba, Zr, Y, Nb, Cs, Sc, V, Cr, Ni, Cu, Zn, Ga, La, Ce, Pr, Nd, Hf, Pb, Th, U) elements by X-ray fluorescence (XRF). Beads were analyzed with a 3·0 kW Panalytical Axios wavelength-dispersive XRF spectrometer with PX1, GE, LiF 220, LiF 200, and PE industrial crystals. Whole-rock geochemistry values are reported in Table 2.

Electron microprobe geochemistry

Major elements were analyzed at the Mineral and Microchemical Analysis Facility at Stanford University using a JEOL JXA-8230 SuperProbe electron microprobe in wavelength-dispersive spectrometry mode with the following conditions: 15 kV accelerating voltage, 20 nA current, and a 3 μm beam. Additional samples were analyzed at the Earth, Planetary, and Space Sciences Department at the University of California, Los Angeles using a JEOL JXA-8200 SuperProbe electron microprobe. Conditions were 15 kV accelerating voltage, 15 nA current, and a 5 μm beam. We selected two to five amphibole grains per sample for core-to-rim traverses to detect any potential zonation patterns that could indicate magma mixing and/or secondary alteration. We carefully documented the position of spots used for electron microprobe analysis (EMPA). For each analyzed amphibole grain in eight of the samples, one to three adjacent plagioclase grains were also analyzed. For calibration, we used matrix-matched natural standards, and microprobe data were corrected using the ZAF correction scheme using coefficients from the FFAST (NIST 2005) database. We then filtered the analyses, marking oxide values that show >30 SD% error as below the level of detection (below LOD), as these values may not be accurate or reliable. Amphiboles were classified using the AMPH-CLASS spreadsheet created by Esawi (2004) and according to the Leake *et al.* (1997) classification scheme. Structural formulae were calculated with cation site occupancies estimated on the basis of 23 oxygen atoms and all Ca in the M4 site, as the H_2O and halogen contents are not well constrained (Leake *et al.*, 1997).

LA-SF-ICP-MS geochemistry

Each spot analyzed by EMPA was also analyzed by *in situ* laser ablation, sector-field inductively coupled plasma mass spectrometry (LA-SF-ICP-MS) for trace elements. Analyses were performed on a Teledyne Cetec Analyte G2 193 nm Excimer laser system paired with a Thermo Scientific Element2 high-resolution sector field ICP-MS in the Department of Geological Sciences laser ablation facility at California State University, Northridge. Ablation was conducted in a helium atmosphere dual-volume cell. We conducted a blank run lasting ~20 min at the beginning of each data

Table 2: Whole-rock major element oxide data (wt%) and sample locations

Sample	Zone	Latitude	Longitude	Fiord name	SiO_2	TiO_2	Al_2O_3	Fe_2O_3	MnO	MgO	CaO	Na_2O	K_2O	P_2O_5	Sum
14NZ01C	I	45°25′35·65"S	166°54′26·97"E	Dagg Sound	54·78	1·03	18·39	8·45	0·13	4·00	6·95	4·65	1·22	0·40	100·00
14NZ02	I	45°26′11·55"S	166°53′55·43"E	Dagg Sound	51·37	1·11	19·86	9·22	0·12	4·11	7·55	5·27	0·96	0·44	100·01
14NZ03A	I	45°20′21·38"S	166°54′10·88"E	First Arm	54·57	1·11	18·37	8·63	0·13	3·86	6·79	4·59	1·51	0·45	100·01
14NZ72	I	45°24′39·95"S	166°56′20·01"E	Crooked Arm	49·78	1·50	19·07	10·03	0·16	4·85	8·06	4·72	1·26	0·57	100·00
14NZ70	II	45°21′38·70"S	167° 3′29·71"E	Doubtful Sound	53·72	1·06	18·31	8·58	0·13	4·33	7·61	5·03	0·82	0·41	100·00
14NZ87	II	45°25′4·46"S	167° 7′36·94"E	Doubtful Sound	58·84	0·92	17·61	6·82	0·10	2·92	5·46	4·41	2·58	0·34	100·00
13VA128A	II	45°33′6·17"S	166°49′32·73"E	Breaksea Sound	49·83	1·46	19·89	9·29	0·16	4·34	8·63	4·41	1·16	0·51	99·66
13VA147A	II	45°32′25·99"S	166°52′24·24"E	Vancouver Arm	50·88	1·36	20·50	8·25	0·12	3·88	7·54	5·28	1·36	0·49	99·65
13NZ38C	III	45°37′39·73"S	166°43′46·88"E	Acheron Passage	54·28	1·20	18·58	7·64	0·12	4·03	7·54	5·27	0·67	0·42	99·75
13VA206A	III	45°36′44·50"S	166°57′38·45"E	Wet Jacket Arm	49·26	1·44	19·66	9·61	0·14	4·68	9·08	4·54	0·76	0·50	99·67
13VA213A	III	45°37′56·98"S	166°52′46·39"E	Wet Jacket Arm	51·14	1·03	20·68	7·56	0·07	4·72	8·97	4·55	0·61	0·41	99·74
12NZ10A	IV	45°35′55·87"S	166°41′4·96"E	Resolution Island	43·10	1·81	20·27	11·97	0·20	6·21	12·35	2·68	0·62	0·53	99·74
12NZ12B	IV	45°35′52·31"S	166°40′55·35"E	Resolution Island	50·98	1·09	19·80	8·96	0·12	4·33	8·51	4·86	0·90	0·45	100·00
13NZKK27B	IV	45°35′56·41"S	166°41′1·71"E	Resolution Island	53·85	1·14	19·14	7·30	0·12	3·98	8·35	4·85	0·61	0·39	99·73

Location provides latitude and longitude coordinates where samples were collected, as well as the name of the fiord in New Zealand. Oxide values were determined by XRF analysis.

collection day to permit background noise to reach a low baseline. Analyses of amphibole were carried out using a fluence of 5·37 J cm^{-2} at a pulse rate of 10 Hz and a beam diameter of 50 μm. For each analysis, we recorded 20–30 s of background (laser off) and 60 s of signal, in addition to 60 s of background recorded at the beginning and end of each ~40 min run. We recorded two to three analyses of primary analytical standard BHVO-2G at the beginning, middle, and end of each run, as well as two to three analyses of each of the secondary analytical standards BCR-2G and GSC-1G at the beginning and end of each run.

Trace-element data were reduced using Iolite (Paton *et al.*, 2011), and CaO wt% as determined by EMPA was used as an internal standard. We determined precision by repeated analysis of basaltic glass BHVO-2G. Long-term precision ranges from 1·9 to 12·6% and is <8·2% for all analyzed elements excluding Cr. Accuracy as measured for basaltic glass BCR-2G was better than 5% relative for Sc, Ti, Zn, Y, Zr, Nb, La, Ce, Pr, Nd, Sm, Eu, Gd, Tb, Dy, Ho, Er, Tm, Yb, Lu, Hf, Ta, and Th, and 10% for V, Mn, Rb, Sr, Ba, and U. Analyses of P, Cr, and Pb were routinely 15% low and those of Ni and Cu were routinely 20% low. Accuracy as measured for synthetic glass GSC-1G was better than 5% for V, Mn, Ni, Zn, Zr, Th, and U, and 10% relative for Rb, Sr, Ba, La, Ce, Pr, Nd, Sm, Eu, Gd, Tb, Dy, Ho, Er, Yb, Hf, and Pb. Analyses of Ti, Cu, Y, Tm, and Lu were routinely 15% low and those of P, Cr, Nb, Sc, and Ta were routinely 20% low. All laser ablation data including standard information are contained in the Supplementary File (supplementary data are available for downloading at http://www.petrology.oxfordjournals.org).

Amphibole thermometry and barometry

We use two equations from Putirka (2016) for calculating amphibole crystallization temperatures: one pressure-independent [equation (5)], and one pressure-dependent [equation (6)]. Compared with the pressure-independent equation, equation (6) at 1·0 GPa results in temperatures that are 4–10 °C higher, and calculated temperatures at 1·2 GPa are 4–15 °C higher. Because emplacement pressures based on contact aureole data have large uncertainties (1·0–1·5 GPa: Allibone *et al.*, 2009b), we use the pressure-independent equation to calculate amphibole crystallization temperatures and to assign temperature-specific partition coefficients. Calculated crystallization temperatures are reported in the Supplementary File and all measured temperatures are assigned uncertainties of ±30 °C based on the Putirka (2016) calibration.

A variety of empirical and experimental studies have shown a correlation between total Al concentration in hornblende and crystallization pressure in melts associated with quartz, plagioclase, hornblende, biotite, orthoclase, titanite, and magnetite (Hammarstrom & Zen, 1986; Hollister *et al.*, 1987; Johnson & Rutherford, 1989; Blundy & Holland, 1990; Schmidt, 1992). Relict igneous assemblages in the Malaspina Pluton generally contain these phases, although quartz is often minor. The Anderson & Smith (1995) calibration involves a temperature correction and is commonly used in granitic systems where amphibole is a near liquidus phase. The barometer is calibrated for systems where temperatures are <800 °C and when applied to Malaspina amphiboles (all of which have temperatures in excess of 800 °C), the barometer yields a wide range of pressures ranging from 0·2 to 1·0 GPa. The Schmidt (1992) and Hollister *et al.* (1987) barometers do not make temperature corrections, and the Schmidt (1992) experimental calibration extends up to 1·3 GPa and therefore encompasses pressures and temperatures appropriate for this study. Consequently, we report the Schmidt (1992) pressures, and we obtain similar results using the Hollister *et al.* (1987) empirical calibration, although calculated pressures are 0·0–0·09 GPa higher in the latter. Uncertainties on the Schmidt (1992) and Hollister *et al.* (1987) barometers are ±0·06 GPa and ±0·10 GPa, respectively. We also compare the Al-in-hornblende pressures with clinopyroxene–liquid barometry presented by Brackman *et al.* (2019) for the Malaspina Pluton. Collectively, these data allow for independent comparisons with contact aureole pressures (1·0–1·5 GPa: Allibone *et al.*, 2009*b*) and metamorphic pressure estimates based on garnet granulite assemblages and pseudo-section modeling (1·2–1·4 GPa; Stowell *et al.*, 2014).

Partition coefficients and melt calculations

Partition coefficients allow for back-calculation of the chemistry of melt in equilibrium with amphibole as it crystallized, so we apply empirical chemometric equations of Zhang *et al.* (2017) to determine major-element composition of melts in equilibrium with our amphibole grains and the partition coefficients of Nandedkar *et al.* (2016) to determine trace-element compositions.

Zhang *et al.* (2017) provided several equations for calculating major-element oxide values (four equations for SiO_2, two equations for most other oxides). When selecting which chemometric equations to use from Zhang *et al.* (2017), we considered that (1) use of lower standard error values increases accuracy, (2) use of fewer variables reduces propagated analytical uncertainty, and (3) addition of temperature slightly improves precision and reduces standard error values. Taking all that into consideration, we selected the following equations to calculate major oxide values: equation (3), equation (5), equation (8), equation (9), equation (10), equation (13), and equation (14) (SiO_2, TiO_2, FeO, MgO, CaO, K_2O, and Al_2O_3 respectively).

Zhang *et al.* (2017) stated that they were unable to establish a robust method for calculating Na_2O wt%, which they speculated could be caused by data collection errors and/or plagioclase control on Na_2O content. In an attempt to reconcile this problem, we use amphibole-equilibrium melt data from Zhang *et al.*

(2017) and assume that the presence of amphibole necessitates >3 wt% water to crystallize (Carmichael, 2002). Based on the early crystallization of hornblende before plagioclase and experimental studies of hornblende-bearing andesite and dacite (Alonso-Perez *et al.*, 2009; Blatter *et al.*, 2017), we assume 3 wt% H_2O and calculate Na_2O wt% as follows: Na_2O wt% = 100 – (sum of calculated major element oxides + 3 wt% H_2O). This calculation neglects the possibility that other oxides and volatiles make up significant quantities in the melt (e.g. CO_2, Cl, F, MnO, P_2O_5), or that H_2O contents were higher. The effect of incorporation of additional H_2O or these elements would be to decrease the Na_2O concentration in the melt; therefore, our calculated Na_2O melt concentrations are probably maxima.

For the calculated trace-element values, we assign a temperature for each spot after Putirka (2016) equation (5), which makes no assumption about pressure. Because the *D* values from Nandedkar *et al.* (2016) correspond to specific temperatures (860 °C, 890 °C, 920 °C, 950 °C), we defined a temperature range for each, to assign the most appropriate *D* value for each spot. Following this method, temperature values between 845 and 875 °C were assigned the *D* value for 860 °C, for 875–905 °C we used the *D* value for 890 °C, for 905–935 °C the *D* value for 920 °C, and for >935 °C the *D* value for 950 °C. The choice of either Putirka (2016) equation (5) (no assigned pressure) or equation (6) (1·0 or 1·2 GPa) results in similar trace-element melt values and does not affect data interpretation because temperature differences are minor between the calculations. We also calculated trace-element melt compositions using partition coefficients from Schnetzler & Philpotts (1970), Klein *et al.* (1997), and Shimizu *et al.* (2017), and find that calculated values are generally similar to the Nandedkar *et al.* (2016) and choice of these values does not change our overall interpretations.

Bulk-rock Sr- and Nd-isotope analysis

Methods for Sr- and Nd-isotope geochemistry are modified from Stowell *et al.* (2010, 2014). Bulk-rock samples were powdered in an alumina ceramic shatterbox and dissolved in HF in Savillex PFA vials on a hot plate. Sample aliquots were spiked with mixed Sm and Nd Spike B from the University of North Carolina at Chapel Hill. Rare earth element (REE) fractions were separated and concentrated from samples using disposable polyprep BioRad ion chromatography columns. Sm and Nd splits were separated from the REE fractions using methylactic acid (MLA) and custom-designed 23 cm silica glass columns. Sm isotopes were measured as metal and Nd isotopes were measured as oxide using a VG Sector 54 thermal ionization mass spectrometer in the Radiogenic Isotope Laboratory at the University of Alabama. Nd-isotope ratios were normalized to $^{146}Nd/^{144}Nd = 0{\cdot}7219$ and then used with Sm-isotope values to compute final isotope ratios and elemental concentrations by isotope dilution. The JNdi Nd standard was run as an oxide periodically during the data collection with $^{143}Nd/^{144}Nd = 0{\cdot}512117 \pm 0{\cdot}000013$. Initial Nd-isotope ratios were calculated using a crystallization age of 120 Ma and a decay constant of $6{\cdot}540 \times 10^{-12}$ a^{-1} for $\lambda^{147}Sm$ (Begemann *et al.*, 2001).

RESULTS

Petrography

Following the Leake et al. (1997) nomenclature, we refer to our amphiboles as 'hornblende' in hand sample and thin section; in all other cases we use the term 'amphibole' or the precise classification names (e.g. pargasite, magnesiohastingsite, tschermakite). In all samples, hornblende is generally subhedral and is an early crystallizing phase. When clinopyroxene and orthopyroxene are present, they crystallized before or together with amphibole and before plagioclase. Apatite and ilmenite are common co-crystallizing phases with hornblende, and biotite is a late crystallizing phase. Plagioclase inclusions are rare in hornblende and most plagioclase grains appear to have crystallized late with respect to hornblende (Fig. 4). Most samples have a hypersolidus foliation defined by alignment of unstrained, commonly tabular, plagioclase and hornblende.

Zones I and III are the only zones observed in this study to have hornblende–pyroxene diorites, and the common relict igneous mineral assemblage of this rock type is Plag + Cpx + Hbl + Bt + Ilm + Ap ± Opx (Fig. 4a, b and e; Table 1). When both pyroxenes are present (14NZ01C, 14NZ03A, 13VA213A), the two are often intergrown and appear either in nearly equal proportions or with more clinopyroxene than orthopyroxene (Fig. 4a). Zone II samples are biotite–hornblende diorites (Fig. 4c and d). The most common mineral assemblage is Plag + Hbl + Bt + Ilm + Ap, although one sample (14NZ87) also has clinopyroxene (Fig. 4c). In this sample, clinopyroxene is often surrounded by subhedral grains of hornblende. The lack of reaction textures between hornblende rims and the clinopyroxene cores suggests that these hornblendes are primary rather than the products of secondary clinopyroxene replacement. The Resolution Orthogneiss in Zone IV does not have any pyroxene and the common mineral assemblage is Plag + Hbl + Ilm + Ap ± Bt (Fig. 4f).

Bulk-rock geochemistry

Malaspina plutonic rocks are primarily classified as alkalic gabbro, monzogabbro, monzodiorite, and monzonite (Table 2). They are magnesian, calc-alkalic to alkali–calcic, metaluminous, and have molar Mg#s that range from 38·8 to 52·6 [Av. = 44·6 ± 2·8 wt%; molar Mg# = 100MgO/(MgO + FeO)]. Na_2O ranges from 4·2 to 5·6 wt% (Av. = 4·7 ± 0·4 wt%), K_2O ranges from 0·45 to 3·04 wt% (Av. = 1·3 ± 0·6 wt%), and Al_2O_3 ranges from 18·0 to 21·1 wt% (Av. = 18·9 ± 0·9 wt%). Like other samples from the Western Fiordland Orthogneiss, the

Malaspina Pluton shows pronounced positive Ba, K, Pb, and Sr anomalies, and negative Nb and Zr anomalies when compared with normal mid-ocean ridge basalt (N-MORB) values (McCulloch *et al.*, 1987; Decker *et al.*, 2017). For all bulk-rock data, the four zones overlap extensively, and we observe no difference in bulk-rock chemistry between the four igneous zones. As we discuss below, we view bulk-rocks as representing cumulates, and therefore we do not place significance on overall similarities in bulk-rock compositions.

Amphibole compositions

Major-element oxides and amphibole classification

Amphibole structural formulae and names for each spot were assigned according to the Leake *et al.* (1997) classification scheme. All analyzed spots were classified as one of the following calcic amphiboles: pargasite, magnesiohastingsite or tschermakite. All calcic amphiboles are defined by the criteria $(Ca + Na)_B > 1{\cdot}00$ and $Na_B = 0{\cdot}50–1{\cdot}50$, and these three varieties are further defined by $Mg/(Mg + Fe^{2+}) = 0{\cdot}5–1{\cdot}0$ and Si in formula $= 5{\cdot}5–6{\cdot}5$. Overall, the samples range from 0·51 to 0·78 in $Mg/(Mg + Fe^{2+})$, and from 5·79 to 6·39 atoms per formula unit (a.p.f.u.) for Si.

Rocks in all four zones contain all three amphibole types; however, it is uncommon for an individual sample to contain grains of all three (observed only in 14NZ02, 14NZ03A and 14NZ72). Most samples are characterized by just one or two varieties (Table 3). The magnesiohastingsite grains show the widest range in $Mg/(Mg + Fe^{2+})$ values (0·51–0·78), followed by pargasite, and tschermakite (0·59–0·70). The Si contents of pargasite and magnesiohastingsite tend toward lower values (5·79–6·25 a.p.f.u. and 5·80–6·39 a.p.f.u., respectively) whereas in tschermakite Si is slightly higher (5·95–6·37 a.p.f.u.).

In addition to these minor compositional differences, we observe variability in terms of applicable modifiers (i.e. ferrian, potassian, and titanian). The relative abundances of these three amphibole types and their various modifiers are somewhat different for each zone; for example, amphibole in Zone I is dominantly magnesiohastingsite, either ferrian or potassian, whereas in Zone IV it is simply magnesiohastingsite, and in Zones II and IV it is ferrian tschermakite. Detailed compositional descriptions of each amphibole type are given below. Overall, these three calcic amphibole varieties are very similar in terms of major-element compositions, and do not distinguish the zones from one another in any definitive way. A summary of the amphibole results is presented in Table 3, and representative amphibole elemental compositions can be found in Table 4.

Samples 14NZ01C, 14NZ03A, 13VA147A, and 12NZ10A have very narrow ranges in Si (∼0·1 a.p.f.u.), making trends difficult to distinguish (Fig. 5). However, Ti, Al, and K contents generally decrease with increasing Si a.p.f.u. (Fig. 5a, b and f). For Ti and K, there are two separate groups, with samples 14NZ01C, 14NZ03A, 14NZ87, 13NZ38C, and 13VA213A having higher abundances than the other samples (Fig. 5a and f). Mg/(Mg + Fe) of the samples generally increases with increasing Si a.p.f.u., and Mn and Na show no distinct trends (Fig. 5c–e).

Trace-element data

Amphibole trace-element abundances define two categories that we refer to as 'enriched' and 'depleted' based primarily on chondrite-normalized REE patterns and high field strength element (HFSE) concentrations. We use Zr as an index of differentiation, and enriched amphiboles are generally classified as having Zr concentrations higher than 35 ppm and distinctly elevated HFSE, whereas depleted amphiboles have lower Zr and far lower HFSE.

For two Zone I samples (14NZ01C and 14NZ03A) all measured HFSE show an enrichment relative to the other two samples (14NZ02 and 14NZ72) (Fig. 6a and b). Most of the Zone II samples plot with the depleted Zone I samples (14NZ70, 13VA128A and 13VA147A), with the exception of one sample (14NZ87), whose compositions are similar to those of enriched Zone I samples. All Zone III samples group with the enriched Zone I samples, and all samples from Zone IV group are similar to depleted Zone I samples.

Chondrite-normalized REE diagrams (Fig. 7) demonstrate the trace element groupings clearly. Enriched samples show elevated light REE (LREE) contents, ranging from ∼10 to 500 times chondritic values. This enrichment increases from La, and peaks between Ce and Nd for all enriched grains, then decreases through Sm. Enriched samples show slightly positive to slightly negative Eu anomalies, depending on the grain. Middle REE (MREE) and heavy REE (HREE) show slightly concave-up patterns that flatten with increasing atomic number (∼10–70 times chondritic values). In general, the shape of the REE plots of enriched amphibole grains is consistent for all of the enriched samples, although the magnitude of enrichment is variable.

Depleted amphiboles show ∼0·02–3 times chondritic values for La, and normalized REE abundances increase steadily to maximum values between Sm and Eu (∼4–40 times chondritic values). Depleted grains show positive to slight negative Eu anomalies overall. MREE and HREE are generally lower than for enriched amphiboles and show similar flat to slightly increasing patterns with increasing atomic number.

Amphiboles in all zones show similar values for Sr, Pb, Mn, Cu, and Zn, with extensive overlap (e.g. Fig. 6c). Rb, Ba, and Ni, however, also show two groups of relative enrichment and depletion, which mirrors patterns in the HFSE (e.g. Fig. 6d). Although they show some overlap of lower values, the enriched samples (14NZ01C, 14NZ03A, 14NZ87, and all Zone III samples) generally show much wider data ranges that extend to values significantly higher than those of the depleted

Table 3: Summary of amphibole classification results

Sample	Zone	Major-element classification	Trace-element classification	Zr range (ppm)	Zr average (ppm)	La range (ppm)	La average (ppm)	La/Sm	Yb range (ppm)	Yb average (ppm)	*T* range (°C)	Average *T* (°C)
14NZ01C	I	Prg	enriched	56·6–78·7	69·8	23·8–42·7	26·7	1·24	7·08–7·79	7·40	938–913	929
14NZ02	I	Prg, Mhs, Ts	depleted	0·026–60·0	17·8	0·004–0·25	0·080	0·041	0·006–5·95	2·64	904–873	893
14NZ03A	I	Prg, Mhs, Ts	enriched	35·8–91·7	58·8	20·8–37·3	32·7	1·32	4·31–11·6	8·58	923–876	902
14NZ72	I	Prg, Mhs, Ts	depleted	18·3–35·9	24·8	0·014–0·264	0·074	0·014	2·90–4·08	3·45	899–873	885
14NZ70	II	Ts	depleted	4·56–8·91	6·84	0·019–0·194	0·050	0·090	1·62–2·41	1·97	887–844	862
14NZ87	II	Prg, Mhs	enriched	30·5–42·0	35·4	26·9–65·0	33·7	1·72	5·32–7·33	6·35	906–856	888
13VA128A	II	Mhs, Ts	depleted	4·60–13·7	11·7	0·009–1·78	0·152	0·181	1·54–4·22	2·59	900–861	891
13VA147A	II	Prg, Mhs	depleted	18·2–28·3	23·3	0·026–0·134	0·050	0·012	2·89–3·48	3·11	920–886	913
13NZ38C	III	Prg, Mhs	enriched	25·7–82·8	68·0	9·80–58·2	15·1	1·59	2·81–4·17	3·29	964–938	950
13VA206A	III	Ts	enriched	26·0–88·4	67·7	2·98–12·4	7·54	0·784	2·22–4·69	2·98	919–875	904
13VA213A	III	Prg, Mhs	enriched	56·5–112	90·6	12·2–32·3	27·3	1·07	7·05–11·6	9·91	935–903	915
12NZ10A	IV	Prg, Mhs	depleted	13·1–23·1	17·5	0·032–0·141	0·077	0·052	2·07–3·16	2·64	943–929	936
12NZ12B	IV	Ts	depleted	13·1–18·3	16·3	0·239–0·682	0·417	0·091	2·83–4·08	3·34	880–865	872
13NZKK27B	IV	Mhs, Ts	depleted	9·91–18·3	14·6	0·278–0·731	0·473	0·090	2·75–4·31	3·50	895–844	873

Description of analyzed samples in terms of major-element classification after Leake *et al.* (1997); abbreviations are after Whitney & Evans (2010); Mhs, magnesiohastingsite; Prg, pargasite; Ts, tschermakite. Trace-element classification describes relative enrichment and depletion compared with other samples in the study. Trace-element abundances (ppm) were determined by LA ICP-MS. Value ranges and averages for representative elements are provided. Zr (index of differentiation), La (LREE), Yb (HREE), and La/Sm ratio (LREE/MREE ratio). Temperatures were calculated using Putirka (2016) pressure-independent equation (5).

Table 4: Representative amphibole compositions

Zone:	I	I	II	II	III	IV
Classification:	Enriched	Depleted	Enriched	Depleted	Enriched	Depleted
Sample:	14NZ03A	14NZ72	14NZ87	13VA147A	13VA213A	13NZKK27B
Grain, spot:	G4, S5	G3, S9	G3, S7	G2, S4	G3, S5	G1, S5
Position:	rim	rim	rim	rim	rim	rim
Major element oxides (wt%), determined by electron microprobe analysis						
SiO_2	39·89	40·47	41·41	40·18	40·89	40·64
TiO_2	2·52	1·11	1·70	1·24	1·32	0·69
Al_2O_3	14·21	14·93	12·64	15·41	15·08	13·18
MnO	0·31	0·23	0·37	0·28	0·19	0·25
FeO	16·93	17·49	16·48	16·85	15·05	18·69
MgO	9·28	9·29	9·85	9·52	10·71	9·97
CaO	11·46	11·59	11·31	11·81	11·48	12·25
Na_2O	1·29	1·66	1·40	2·10	1·45	1·55
K_2O	2·29	1·15	1·89	1·11	1·98	0·94
Cl	0·07	0·15	0·15	0·15	0·06	0·11
Total	98·25	98·05	97·19	98·65	98·20	98·28
Structual formulae according to Leake et al. (1997)						
T sites						
Si	5·97	6·01	6·23	5·95	6·02	6·05
^{iv}Al	2·03	1·99	1·77	2·05	1·98	1·95
C sites						
^{vi}Al	0·48	0·62	0·48	0·64	0·63	0·36
Ti	0·28	0·12	0·19	0·14	0·15	0·08
Fe^{3+}	0·48	0·73	0·48	0·57	0·65	0·89
Mg	2·07	2·06	2·21	2·10	2·35	2·21
Fe^{2+}	1·64	1·44	1·59	1·52	1·20	1·43
Mn^{2+}	0·04	0·03	0·05	0·04	0·02	0·03
B sites						
Ca	1·84	1·84	1·82	1·87	1·81	1·95
Na	0·16	0·16	0·18	0·13	0·19	0·05
A sites	2·00	2·00		2·00	2·00	2·00
Na	0·21	0·32	0·23	0·48	0·22	0·40
K	0·44	0·22	0·36	0·21	0·37	0·18
Sum cations	17·65	17·54	15·60	17·69	17·60	17·58
Mg/Fe^{2+}	1·27	1·43	1·39	1·38	1·95	1·54
Stoichiometric formulae according to Leake et al. (1997) (a.p.f.u.)						
Si	6·04	6·10	6·30	6·02	6·10	6·17
Ti	0·29	0·13	0·19	0·14	0·15	0·08
Al	2·53	2·65	2·26	2·72	2·65	2·36
Mn^{2+}	0·04	0·03	0·05	0·04	0·02	0·03
Fe^{2+}	2·14	2·20	2·09	2·11	1·88	2·37
Mg	2·09	2·09	2·23	2·13	2·38	2·26
Ca	1·86	1·87	1·84	1·90	1·84	1·99
Na	0·38	0·48	0·41	0·61	0·42	0·46
K	0·44	0·22	0·37	0·21	0·38	0·18
Cl	0·02	0·04	0·04	0·04	0·00	0·00
Sum atoms	15·83	15·82	15·79	15·91	15·82	15·89
Trace element abundances (ppm), determined by LA-ICP-MS						
P	91·90	20·9	n.a.	1382·00	1373·00	1490·00
Sc	64·8	37·1	78·7	43·8	60·6	49·8
Ti	18100	6480	12040	8100	10310	4410
V	581	344	470	389	375	437
Cr	65	23·70	56·3	40·7	48·2	52·7
Mn	2531	2480	3290	2225	1712	1930
Ni	72	44·4	41·6	43·3	73·4	45·6
Cu	5·6	b.d.l.	101	3·21	11·70	24·0
Zn	249	223	365	253	269	188
Rb	24·8	2·22	16·8	3·26	11·33	0·940
Sr	182	86	93·1	98	146	440·0
Y	120·3	33·7	84·8	32·1	122·6	34·4
Zr	67·8	18·3	39·6	26·6	91·8	10·6
Nb	30·6	0·76	22·0	0·959	20·0	3·01
Ba	259	118·5	54·5	121	169	137·0
La	32·8	0·052	28·3	0·063	29·80	0·357
Ce	133·7	0·932	116	1·14	123·4	2·76
Pr	23·7	0·558	19·3	0·638	22·06	0·99
Nd	118·8	6·02	94·5	7·00	107·9	8·6
Sm	32·1	4·51	23·5	4·55	30·60	5·30
Eu	5·71	1·51	4·16	1·43	5·84	2·17
Gd	32·6	5·46	20·0	5·61	28·70	6·24

(continued)

Table 4: Continued

Zone:	I	I	II	II	III	IV
Classification:	Enriched	Depleted	Enriched	Depleted	Enriched	Depleted
Sample:	14NZ03A	14NZ72	14NZ87	13VA147A	13VA213A	13NZKK27B
Grain, spot:	G4, S5	G3, S9	G3, S7	G2, S4	G3, S5	G1, S5
Position:	rim	rim	rim	rim	rim	rim
Tb	3·93	0·96	2·77	0·945	4·36	1·07
Dy	23·0	6·15	15·4	6·38	26·10	6·47
Ho	4·40	1·24	3·01	1·16	4·81	1·30
Er	12·06	3·39	8·23	3·51	13·49	3·39
Tm	1·62	0·494	1·13	0·510	1·840	0·481
Yb	10·51	3·08	6·72	2·93	11·62	3·16
Lu	1·50	0·446	0·960	0·451	1·520	0·453
Hf	2·88	1·08	2·08	1·22	3·75	0·96
Ta	0·932	b.d.l.	1·10	b.d.l.	0·769	0·124
Pb	5·09	1·38	5·24	2·04	3·97	3·21
Th	0·702	0·00	2·05	b.d.l.	0·448	0·01
U	0·118	0·001	0·620	0·037	0·057	0·044

Amphibole grains are representative of each zone, and of the grain size for each sample. Zones I and II each have two representative samples, one enriched (14NZ01C, 14NZ87) and one depleted (14NZ72, 13VA147A). Structural and stoichiometric formulae were calculated using the AMPH-CLASS spreadsheet from Esawi (2004), and structural formula was used to classify the amphiboles according to Leake *et al.* (1997). n.a., not analyzed, b.d.l., below detection limit for the laser system.

samples (14NZ02, 14NZ72, 14NZ70, 13VA128A, 13VA147A, and all Zone IV samples).

Plagioclase compositions

Plagioclase grains were analyzed in samples from all zones except Zone I. Plagioclase compositions are largely albite-rich (Ab $>$ 64 %; Fig. 8). Petrographically, plagioclase displays polysynthetic twinning and zonation is rare. Most grains are oligoclase to andesine, but in 12NZ10A plagioclase grains are andesite and labradorite. This latter sample also appears to be more variable and more calcium-rich on average than the other Zone IV samples. The mean plagioclase composition for all samples (three end-member series: Ab % 68·3, An % 31·3, Or % 0·4; normalized to plagioclase series: Ab % 68·5, An % 31·5) is plotted as a purple star. All analyzed spots are less than 70 % anorthite. Representative plagioclase analyses are presented in Table 5 and all data are provided in the Supplementary File.

Thermometry and barometry

Amphibole temperatures from the Malaspina Pluton range from ~960 to 830 °C (Fig. 9). Zone III has the highest average temperature (Av. = 914 °C), followed by Zone IV (Av. = 888 °C), then Zone I (Av. = 887 °C), and then Zone II with the lowest average value (Av. = 882 °C). Individual samples show intrasample crystallization temperature ranges $\leq$60 °C, and we generally observe no measurably significant core-to-rim variation within analytical uncertainty (1SD). Figure 10 demonstrates this observation for sample 13VA147A, along with Zr values that also show no statistical core-to-rim variation. From all four zones, samples display a wide range of initial crystallization temperatures, with some as high as 958 °C (13NZ38C) and some as low as 869 °C (12NZ12B) (Fig. 9c). The enriched group amphiboles yield essentially the same temperature (Av. = 901 °C) compared with the depleted group (Av. = 884 °C).

Sample average Al-in-hornblende pressures using the Schmidt (1992) calibration range from 0·81 to 1·09 GPa with highest and lowest sample average values located in Zone IV. By zone, pressures are in the range of 0·88–0·96 GPa for Zone I, 0·82–1·0 GPa for Zone II, 0·91–0·96 GPa for Zone III, and 0·81–1·09 GPa for Zone IV. There is no statistically significant difference in pressures between zones and the average pressure for all amphiboles in the Malaspina Pluton is 0·92 $\pm$ 0·09 GPa (1SD, n = 364). Using the Hollister *et al.* (1987) empirical calibration, the average pressure for all amphiboles is 0·97 $\pm$ 0·11 GPa (1SD, n = 364). Brackman *et al.* (2019) calculated crystallization pressures using the calibrated Jd-in-clinopyroxene geobarometer and found that igneous clinopyroxenes in the Malaspina Pluton give pressures of 1·1 GPa assuming 3 wt% H_2O and 0·95 GPa assuming 6 wt% H_2O.

Bulk-rock Sr and Nd isotopes

Three samples were analyzed from each of the four zones in the Malaspina Pluton to evaluate magma sources and determine isotope variations between enriched and depleted samples (Table 6; Fig. 11a). Samples from Zone I have initial $^{143}Nd/^{144}Nd$ values ranging from 0·51253 to 0·51255, and initial $^{87}Sr/^{86}Sr$ values ranging from 0·70415 to 0·70419. In Zone II, samples have initial $^{143}Nd/^{144}Nd$ values ranging from 0·51254 to 0·51256, and initial $^{87}Sr/^{86}Sr$ values ranging from 0·70415 to 0·70424. In Zone III, samples have initial $^{143}Nd/^{144}Nd$ values ranging from 0·51254 to 0·51262, and initial $^{87}Sr/^{86}Sr$ values ranging from 0·70413 to 0·70420. Finally, in Zone IV, samples have initial $^{143}Nd/^{144}Nd$ values ranging from 0·51253 to 0·51254, and initial $^{87}Sr/^{86}Sr$ values ranging from 0·70411 to 0·70417. We

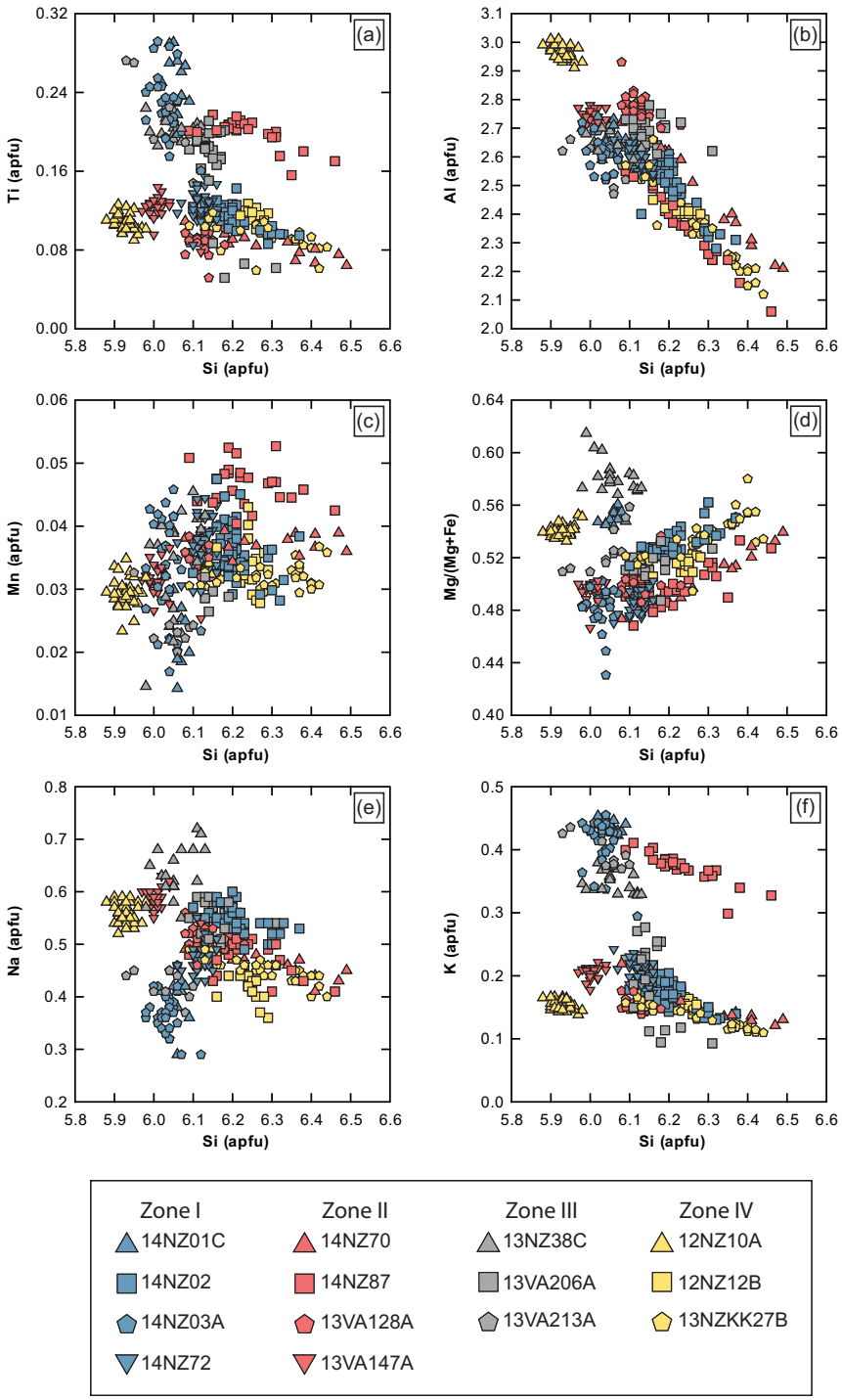

Fig. 5. Bivariate plots of stoichiometric atoms per formula unit values for analyzed amphibole spots using the Esawi (2004) AMPH-CLASS spreadsheet following the Leake *et al.* (1997) classification scheme.

observe no systematic difference between zones or between enriched and depleted samples (see Fig. 11a inset).

DISCUSSION

Melt compositions and sources

In Cordilleran arcs, the lower arc crust is commonly considered to be an important region for the generation of intermediate and silicic magmas via differentiation of primary basaltic magmas by fractional crystallization (e.g. Gill, 1981; Grove & Kinzler, 1986; Musselwhite *et al.*, 1989; Rogers & Hawkesworth, 1989; Müntener *et al.*, 2001; Grove *et al.*, 2002, 2003), and/or through partial melting of older crustal rocks (Smith & Leeman, 1987; Atherton & Petford, 1993; Tepper *et al.*, 1993; Rapp & Watson, 1995; Petford & Atherton, 1996; Chappell & White, 2001; Izbekov *et al.*, 2004). These

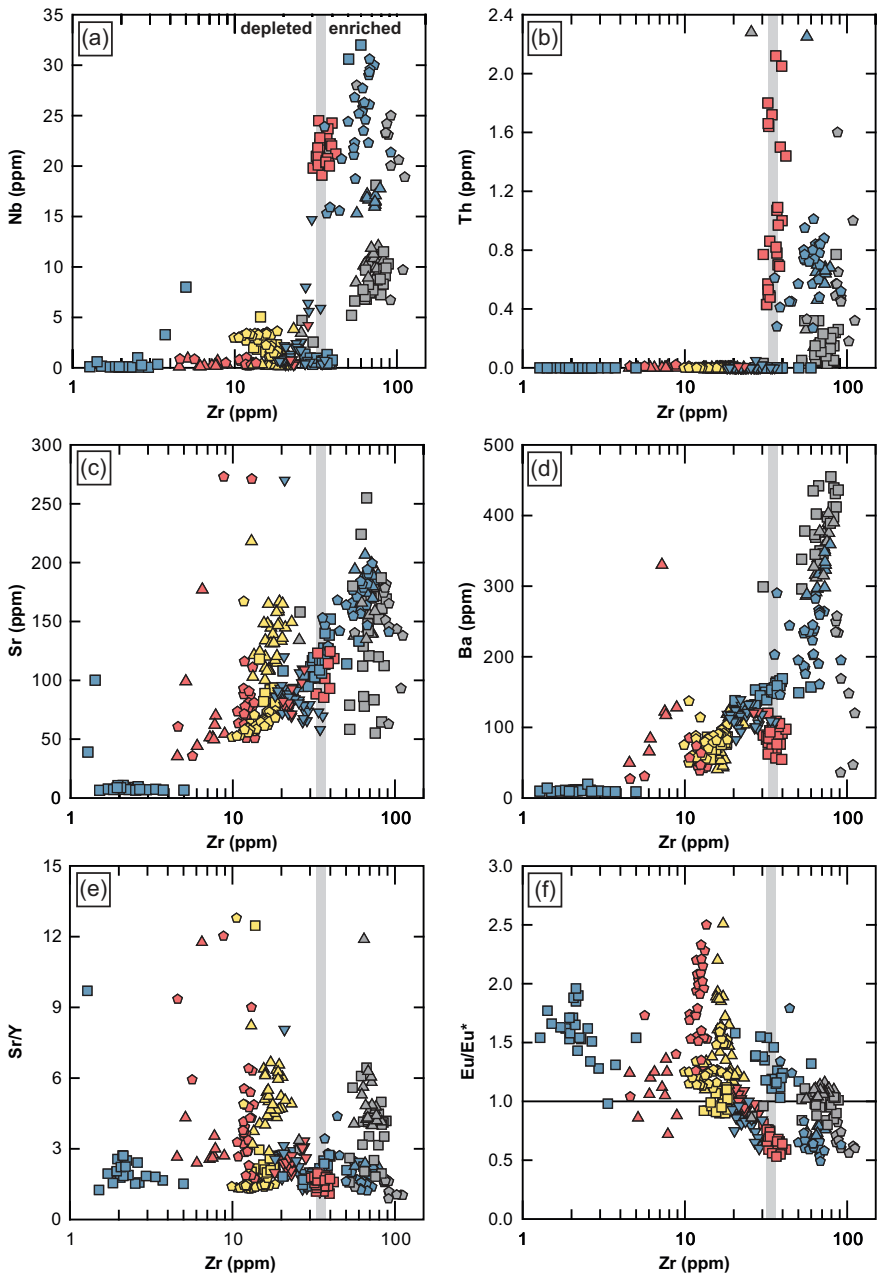

Fig. 6. (a–e) Bivariate plots of amphibole trace-element abundances. (a, b) High field strength elements (Nb and Th); (c, d) large ion lithophile elements (Sr and Ba); (e) ratio of a large ion lithophile element to a high field strength element (Sr/Y). Relative enrichment and depletion is apparent in elements Nb, Th, and Ba; sample values overlap extensively in Sr and Sr/Y ratio. (f) Eu/Eu* = 1 indicates no Eu anomaly; Eu/Eu* is calculated as $(Eu/0{\cdot}058)/[(Sm/0{\cdot}153)(Gd/0{\cdot}2055)]^{0{\cdot}5}$. Trace-element abundances (ppm) were determined by LA-SF-ICP-MS. Gray bars indicate the division between enriched and depleted groups.

processes can occur together as successive batches of melt intrude and crystallize in the lower crust, transferring heat to host rocks whose solidus may be lowered by H_2O liberated from crystallizing basaltic magmas (Petford & Gallagher, 2001; Annen & Sparks, 2002; Collins *et al.*, 2020). In addition to fractionation and remelting of existing crust, various additional factors also contribute to the geochemical diversification of melts in the lower crust including the geometry of the melt or mush reservoir, the thermal architecture of host rocks and intrusive melts, mafic melt replenishment, and rejuvenation or dissolution of pre-existing cumulates. Below, we use amphibole geochemical data from the Malaspina Pluton to explore these melt diversification processes and to place constraints on the geometry and thermal architecture of the Malaspina Pluton during lower-crustal construction.

Amphibole-equilibrium melt compositions

Calculated amphibole-equilibrium melt compositions range from andesite to dacite and show a broad range

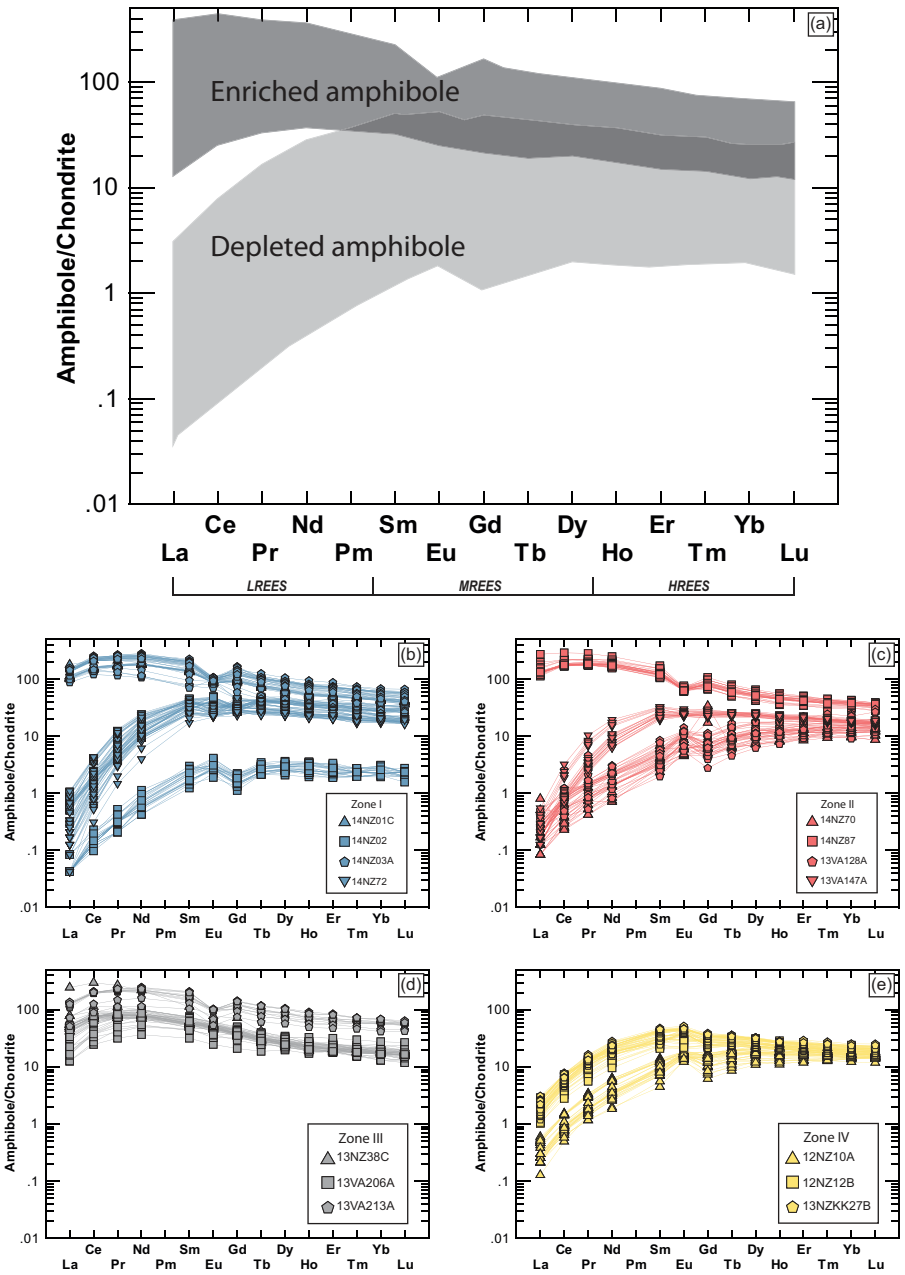

Fig. 7. Rare earth element spider diagrams of amphibole data normalized to chondritic values, after Sun & McDonough (1989). (a) Dark gray field shows all enriched group analyses and light gray field shows all depleted group samples. Individual analyses are plotted by zone (b–e). Trace-element abundances (ppm) were determined by LA-SF-ICP-MS.

in SiO_2 (55–70 wt%) that mirrors compositions of middle to upper continental crust estimates (Fig. 12) (Table 7). Molar Mg#s range from 27 to 46 and confirm that Malaspina melts are geochemically fractionated especially compared with bulk lower continental crust estimates (Fig. 12f). These findings are significant because they demonstrate that evolved arc melts with compositions approximating middle to upper continental crust were produced at deep-crustal levels within the lower crust during arc construction.

Malaspina melts are also classified as calc-alkalic, magnesian to ferroan, and metaluminous to peraluminous in composition (Fig. 13), and they have values that are similar to fractionated amphibole-bearing melts in a variety of Cordilleran arcs (e.g. Werts *et al.*, 2020). We do not observe a significant distinction in the range of calculated SiO_2 or Mg# between the enriched and depleted amphibole-equilibrium melts. This observation is important because it rules out a potential consanguineous relationship between depleted and enriched melts by fractional crystallization.

In detail, calculated amphibole-equilibrium melts decrease monotonically with increasing SiO_2 and decreasing molar Mg# (Fig. 12). They also show two trends that correspond to relatively high- and low-Al_2O_3 groups at constant SiO_2 (see blue and green trend lines in

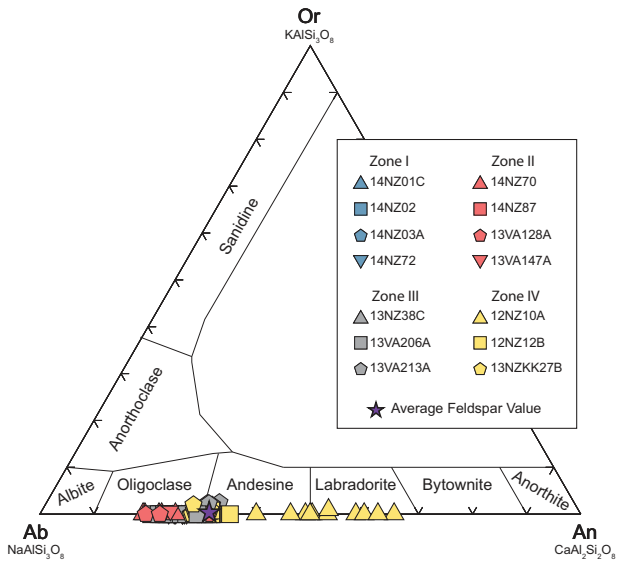

Fig. 8. Ternary feldspar classification diagram. All samples plot as plagioclase feldspars, ranging from albite to bytownite in composition. No samples plot higher than 86% anorthite. An average feldspar value (Ab% 68·3, An% 31·3, Or% 0·4) is shown as a purple star.

Table 5: Representative feldspar compositions

Zone:	II	III	IV
Sample:	13VA147A	13VA213A	12NZ10A
Grain, spot:	G2, S5	G3, S5	G3, S13
SiO_2	61·65	60·52	55·97
Al_2O_3	24·06	25·03	28·46
FeO	0·16	0·00	0·16
CaO	4·91	6·16	9·41
Na_2O	8·52	7·60	5·97
K_2O	0·12	0·37	0·00
Total	99·41	99·68	99·97
Three end-member series normalization			
Ab%	75·32	67·55	53·48
An%	24·01	30·27	46·52
Or%	0·67	2·19	0·00
Plagioclase-series normalization			
Ab%	75·83	69·06	53·48
An%	24·17	30·94	46·52

Feldspar grains are representative of each zone, and a near-average normalization value for their respective zones. Oxide values are in wt%, as determined by EMPA.

Fig. 12b). The high-Al_2O_3 group corresponds to trace-element depleted melts, and conversely, the low-Al_2O_3 group corresponds to trace-element enriched melt group (Fig. 12). Depleted-melt samples are also distinguished by higher average molar Mg#, and lower average FeO, CaO, and TiO_2 at constant SiO_2 values (green trend lines in Fig. 12). Both groups are significantly more fractionated than high-Mg basalts and andesites generated in hydrous peridotite melting experiments (Hirose & Kawamoto, 1995; Hirose, 1997). Amphibole-equilibrium melt compositions also diverge significantly from host bulk-rock values and average lower continental crust estimates for all major-element oxides (see open symbols in Fig. 12, and Table 8 for a comparison between whole-rock data and calculated-melt values). These findings are consistent with those of Werts *et al.* (2020), who also found magmatic arc amphiboles to be in equilibrium with melts that are compositionally distinct and typically more silicic than the bulk-rocks. We return to the discrepancy between amphibole-equilibrium melts and bulk-rocks later.

The highly evolved nature of both enriched and depleted amphibole-equilibrium melts raises the question of whether calculated melts are biased towards more felsic values owing to preselection of amphibole-bearing samples. We find this to be unlikely because the presence of clinopyroxene in some samples does not correlate with high molar Mg#s or lower SiO_2 in calculated amphibole-equilibrium melts. Instead, the presence of clinopyroxene probably indicates slightly different bulk compositions or H_2O contents. In addition, petrographic observations from thin sections show that amphiboles are liquidus or near-liquidus minerals in most of our samples (Fig. 4), and field mapping indicates that amphibole-bearing diorites and amphibole–clinopyroxene diorites make up the majority of relict igneous rock assemblages in the Malaspina Pluton (Klepeis *et al.*, 2007, 2016). These observations support the notion that amphibole-bearing andesites and dacites were the dominant melt composition in the Malaspina Pluton, and they played a major role in lower arc crust construction. Our observations also support numerical simulations that predict the generation of felsic to intermediate melts in the lower crust (Annen *et al.*, 2006; Solano *et al.*, 2012); however, in our study, individual samples show restricted ranges in molar Mg# and SiO_2 (<5 wt% for all samples), indicating limited melt diversification and fractionation in sheeted intrusions at the level of emplacement (see Supplementary File for details). This observation precludes widespread melt connectivity and homogenization, and we return to this problem later.

Although we observe limited evidence for *in situ* fractionation within individual samples, pluton-scale geochemical trends show evidence for significant fractionation and melt diversification in the lower crust. Figure 12 illustrates trends for the enriched- and depleted-melt groups over ~54–70 wt% SiO_2 consistent with extensive fractionation of amphibole + plagioclase ± clinopyroxene from both melt groups. The large green and blue triangles in Fig. 12 represent our parental-melt estimates for the enriched- and depleted-melt groups (~55 wt% SiO_2, 40–45 molar Mg#). These parental-melt compositions are remarkably similar to parental compositions used in fractionation experiments reported by Alonzo-Perez *et al.* (2009), which were conducted on a synthetic andesite modeled on a sample from the Adamello Batholith (see yellow circles in Fig. 12). In their garnet-absent fractionation experiments at 0·8 GPa (hollow blue circles in Fig. 12), liquid lines of descent show similar trends compared with the Malaspina melt data. At temperatures and compositions similar to what we observe in this study (850 °C

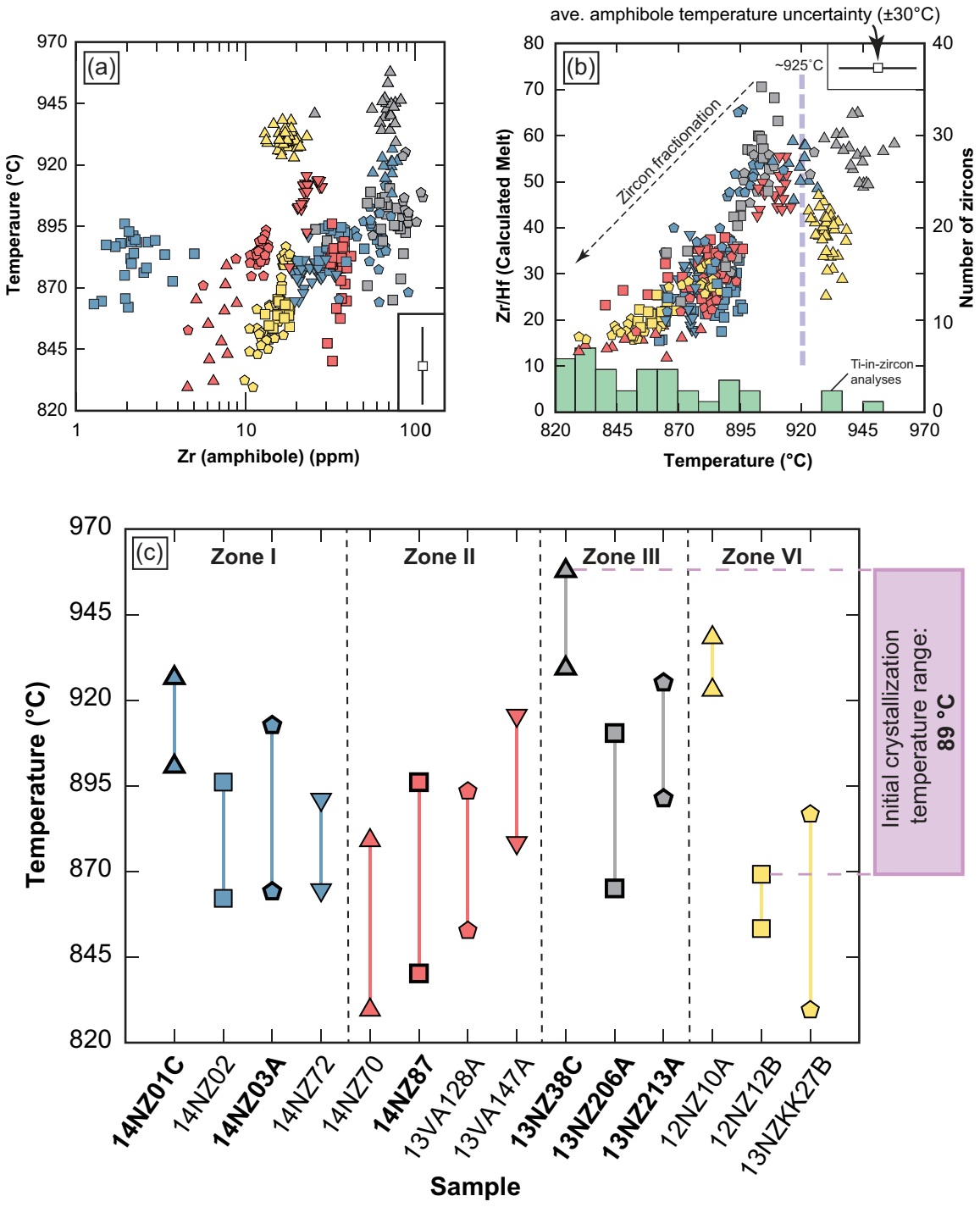

Fig. 9. Bivariate plots of amphibole temperatures calculated using Putirka (2016) pressure-independent equation (5). (a) All samples show a fractionation trend when plotted versus Zr ppm. (b) Zr/Hf calculated-melt values using Nandedkar *et al.* (2016) partition coefficients vs amphibole temperatures; green bars indicate the number of zircons at each temperature from Schwartz *et al.* (2017) as determined by Ti-in-zircon analyses using Ferry & Watson (2007). (c) Crystallization temperature ranges for all samples. Atoms per formula unit were calculated from oxide values measured by EMPA; trace-element abundances (ppm) were determined by LA-SF-ICP-MS.

and ~62·5 wt% SiO_2), closed-system fractionation experiments produce 25 % amphibole, 21 % plagioclase and 1 % ilmenite, and ~54 % derivative melt (see RP40 of Alonzo-Perez *et al.*, 2009). Based on comparison with these experiments, we speculate that the proportion of cumulate to fractionated dacite in the Malaspina system was ~1:1, and much of the derivative melt was lost via vertical migration to higher crustal levels. We return to the fate of the lost melt later in the discussion.

When plotted together, both enriched and depleted amphibole-equilibrium melts display a strong unimodal

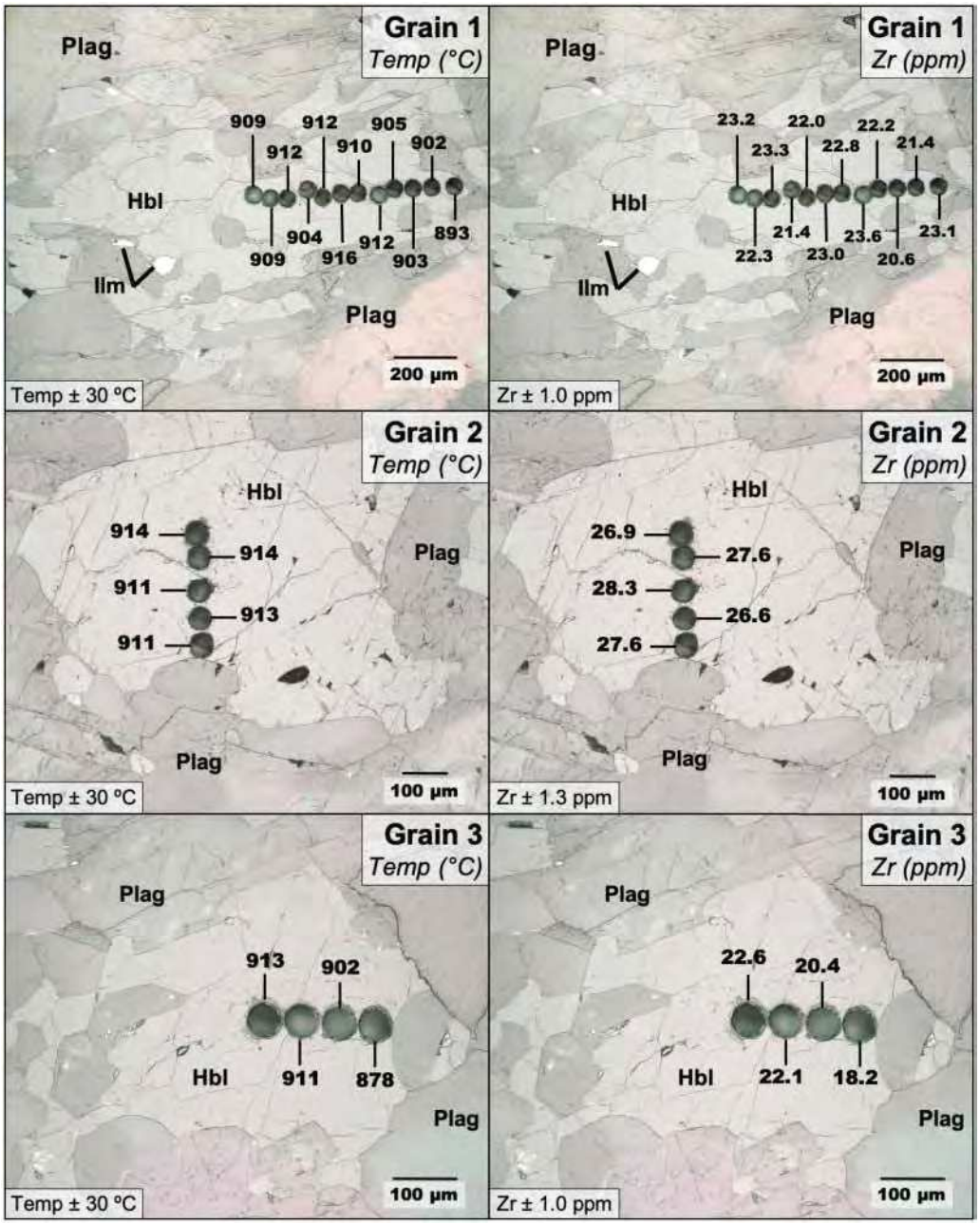

Fig. 10. Reflected-light photomicrographs of 13VA147A analyzed grains with laser ablation pits and temperature (left) and Zr ppm value (right) annotations. Temperature annotations show values calculated using Putirka (2016) pressure-independent equation (5). Trace-element abundances (ppm) were determined by LA-SF-ICP-MS.

SiO_2 peak at 62·5 ± 2·8 wt% (Fig. 13b). Compared with a global compilation of melt inclusions from more than 85 arc volcanoes by Reubi & Blundy (2009), our data lie within a pronounced compositional gap between mafic and felsic compositional end members that have peaks at 54 wt% and 76 wt% SiO_2, respectively (see orange curve in Fig. 13b). Reubi & Blundy (2009) argued that intermediate melts are rare in arc settings, and when they appear they are the result of mingling or mixing processes within bimodal magmatic systems in the upper crust. Our data demonstrate that intermediate compositions are the dominant melt type in lower arc crust, and we do not see convincing evidence for mingling or mixing in our amphibole data. Instead, our data are most consistent with melt diversification primarily by fractionation of amphibole + plagioclase + clinopyroxene from a basaltic andesite parental melt. Below, we explore magma sources and possible contributions from crustal and mantle sources.

Contributions from a hydrous mantle wedge

A key finding in our data is that most amphibole-equilibrium melts are highly fractionated (molar Mg#

Table 6: Whole-rock Nd and Sr isotopes

Sample	Zone	Trace-element classification	[Sm] (ppm)	[Nd] (ppm)	$^{147}Sm/^{144}Nd$	2σ	$^{143}Nd/^{144}Nd$ (m)	2σ	$^{143}Nd/^{144}Nd$ (i)	εNd initial	*t*DM1 (Ma)	Rb (ppm)	Sr (ppm)	$^{87}Sr/^{86}Sr$ (m)	$^{87}Sr/^{86}Sri$	2σ
14NZ01C	I	enriched	3·88	19·68	0·1192	0·0008	0·512631	0·000008	0·512537	–2·0	679	13·9	1246·3	0·70421	0·70415	0·00001
14NZ02	I	depleted	4·11	22·03	0·1129	0·0008	0·512636	0·000011	0·512547	–1·8	630	14·3	1439·7	0·70424	0·70419	0·00001
14NZ72	I	depleted	6·42	34·82	0·1115	0·0008	0·512618	0·000022	0·512530	–2·1	648	19·5	1146·5	0·70425	0·70416	0·00001
14NZ70	II	depleted	3·73	18·54	0·1217	0·0009	0·512635	0·000015	0·512539	–1·9	690	14·3	1235·5	0·70422	0·70416	0·00001
13VA128A	II	depleted	5·05	25·49	0·1197	0·0008	0·512646	0·000010	0·512552	–1·7	659	21·4	1291·3	0·70423	0·70415	0·00001
13VA147A	II	depleted	4·43	24·01	0·1115	0·0009	0·512652	0·000033	0·512564	–1·4	599	19·4	1406·7	0·70431	0·70424	0·00001
13NZ38C	III	enriched	4·17	20·43	0·1234	0·0009	0·512718	0·000036	0·512621	–0·3	569	17·6	1196·9	0·70427	0·70420	0·00001
13VA206A	III	enriched	5·51	26·53	0·1255	0·0009	0·512636	0·000010	0·512537	–2·0	717	22·9	1464·0	0·70422	0·70415	0·00001
13VA213A	III	enriched	3·16	14·60	0·1308	0·0009	0·512644	0·000010	0·512541	–1·9	746	14·3	1356·6	0·70418	0·70413	0·00001
12NZ10A	IV	depleted	5·34	24·59	0·1313	0·0009	0·512630	0·000010	0·512527	–2·2	775	22·8	1210·7	0·70425	0·70415	0·00002
12NZ12B	IV	depleted	4·13	20·84	0·1197	0·0008	0·512637	0·000001	0·512543	–1·9	673	17·4	1289·6	0·70423	0·70417	0·00001
13NZKK27B	IV	depleted	3·71	18·38	0·1221	0·0009	0·512639	0·000010	0·512543	–1·9	686	15·8	1343·2	0·70417	0·70411	0·00002

Age assumed as 120 Ma for calculating initial ratios on initial Nd sheet; 2 σ absolute; m, measured values.

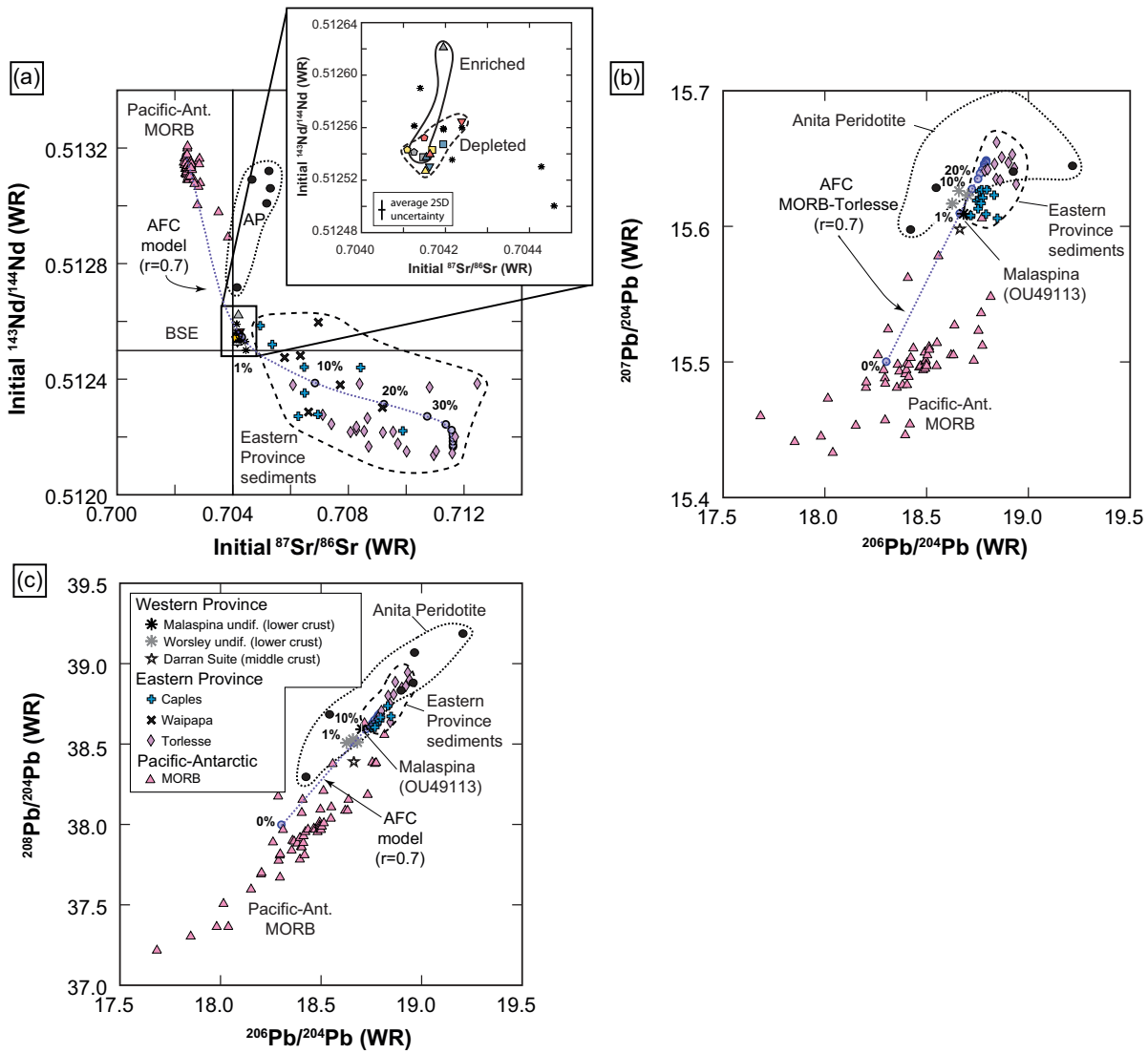

Fig. 11. Malaspina Pluton isotope data. (a) Initial whole-rock Sr- and Nd-isotope data calculated at 120 Ma and compared with Bulk Silicate Earth. Inset shows a close-up of Malaspina data. (b, c) Bulk-rock Pb-isotope data for the pluton. Blue dashed lines indicate assimilation and fractional crystallization model. Data for Pacific–Antarctic MORB were compiled from Vlastelic *et al.* (1999). Eastern Province sediment data were compiled from Adams *et al.* (2005) and Graham *et al.* (1992). Zealandia Pb-isotope data were compiled from Mattinson *et al.* (1986).

<50), andesitic to dacitic in composition, and are much more evolved than bulk lower continental crust or primitive basalts and andesites predicted to have formed from hydrous melting of mantle-wedge peridotite beneath an arc (see Fig. 12) (primary magmas SiO_2 ~50–60 wt%; molar Mg# = 66–75: Roeder & Emslie, 1970; Green, 1971). Malaspina melts also show Fe depletion and alkali enrichment associated with calc-alkaline magmas (Fig. 13), which raises a fundamental issue for both the depleted and evolved melt groups: did the calc-alkaline signature and evolved nature of Malaspina melts originate from a mantle source (Carmichael, 1991), by magmatic fractionation (Bowen, 1929), and/or through contamination and mixing with a Si-rich, Fe-poor crustal material (Grove *et al.*, 1982)?

In the case of the depleted-melt group, chondrite-normalized REE patterns show flat MREE to HREE patterns and depletions in LREE (Fig 14a). Compared with N-MORB and Pacific–Antarctic MORB, depleted melts show prominent positive anomalies in fluid-mobile large ion lithophile elements (LILE) such as Ba, U, K, Pb and Sr, and sub-N-MORB values for elements typically considered immobile in aqueous fluids such as high field strength elements (HFSE: Th, Nb, Zr, and HREE) (Figs 14b and 15a–d). Depleted melts also show prominent negative Nb, Ta, and sometimes Ti anomalies, which are often recognized as related to subduction-related fluids and/or melts (see Izu arc data in Fig. 14b). These features are common in arc magmas derived from a previously depleted mantle wedge that was enriched by a slab-derived fluid component, and they support the interpretation that depleted-group melts were sourced from an oxidized depleted mantle with a subduction-related fluid component.

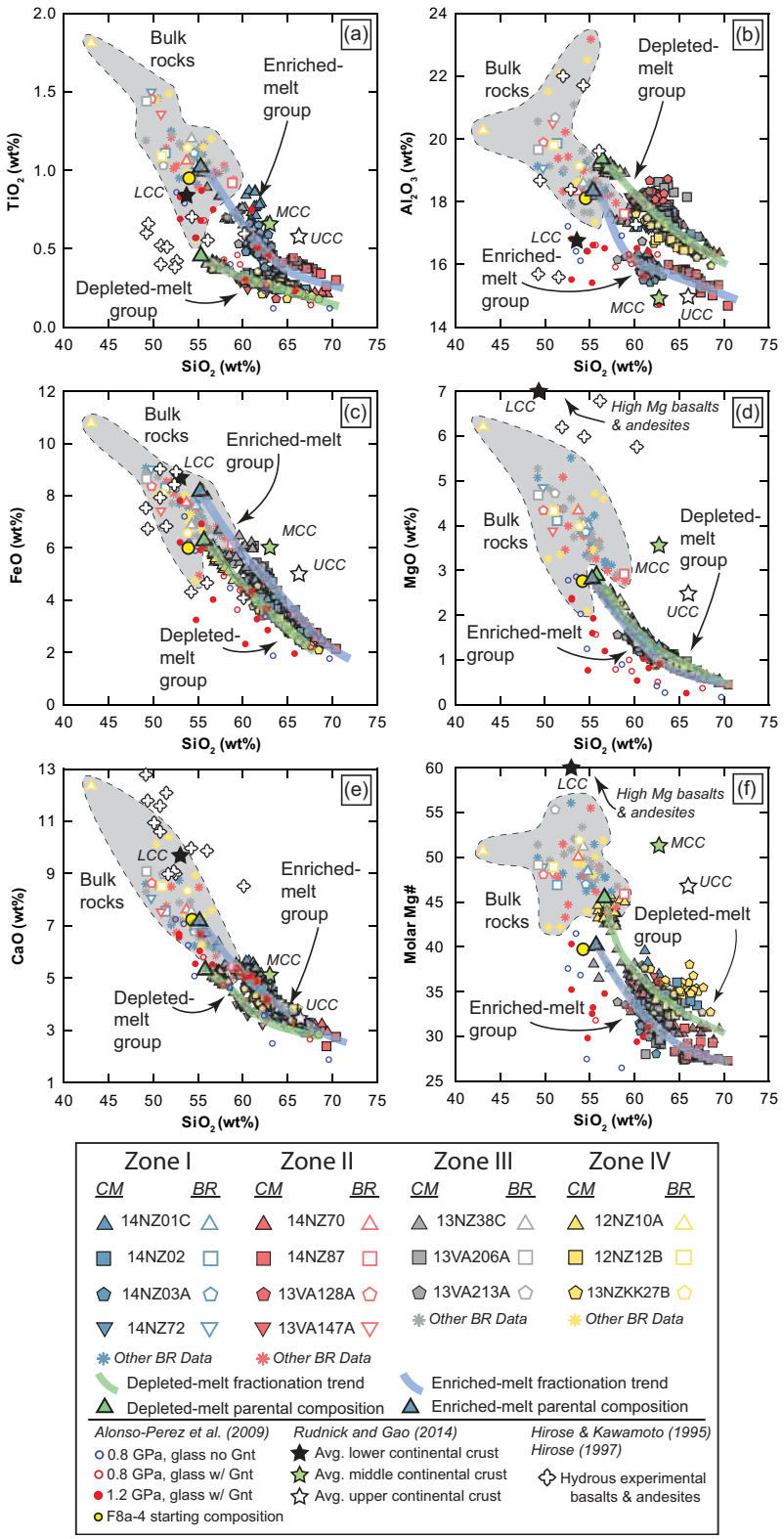

Fig. 12. Major-element oxides of melts calculated from amphibole compositions compared with bulk-rock data. All oxides except MgO (d) show two distinct trends in the calculated-melt data. Green and blue lines indicate trend lines for depleted and enriched melts, respectively. In all cases, bulk-rock data are distinct from the calculated-melt data with little to no overlap. White, green, and black stars show average upper-, middle-, and lower-crustal values respectively (Rudnick & Gao, 2013). High-Mg basalts and andesites from hydrous peridotite melting experiments are shown as hollow crosses (Hirose & Kawamoto, 1995; Hirose, 1997). Circles indicate values from Alonso-Perez *et al.* (2009) experimental glasses at 0·8 GPa without garnet as a fractionating phase (open blue circles), 0·8 GPa with garnet as a fractionating phase (open red circles), and 1·2 GPa where garnet was always present as a fractionating phase (filled red circles). Oxide values were derived using the chemometric equations of Zhang *et al.* (2017). Molar Mg# = 100MgO/(MgO + FeO + 0·8998Fe_2O_3). BR, bulk-rock data; CM, calculated amphibole-equilibrium melt.

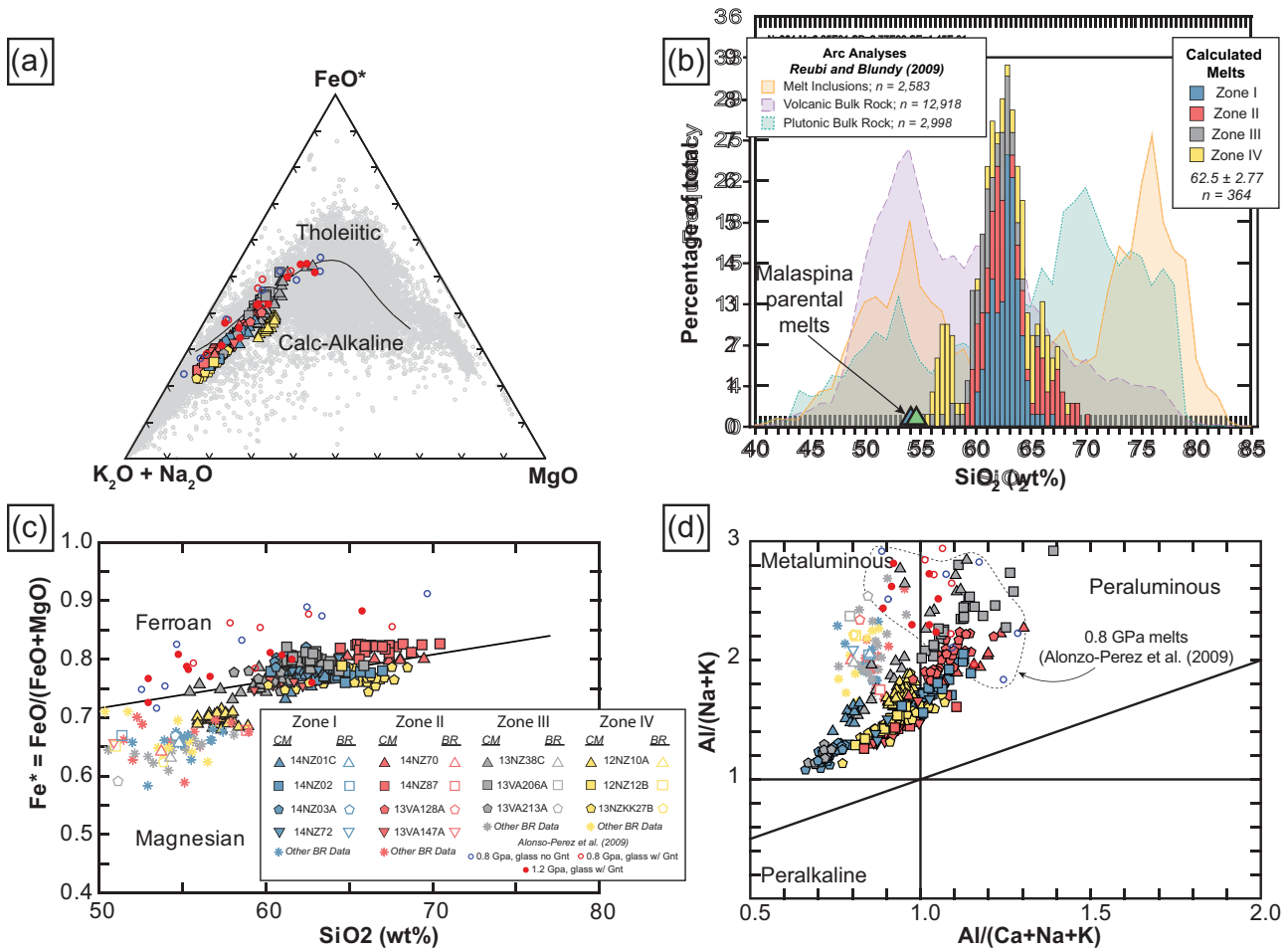

Fig. 13. Comparison of calculated-melt values with compiled melt inclusion and bulk-rock data. (a) Triangular AFM diagram showing that samples from this study follow the calc-alkaline trend; other data are from the GEOROC database precompiled files of melt inclusions, as in the study by Reubi & Blundy (2009); FeO* = FeO + (0·8998 Fe_2O_3). (b) Histogram of calculated melt SiO_2 wt% values overlain on plots of compiled arc SiO_2 data; modified from Reubi & Blundy (2009). (c) Melt data straddle the line between ferroan and magnesian, whereas bulk-rocks are exclusively magnesian. (d) Melts range from metaluminous to peraluminous, whereas bulk-rocks are exclusively metaluminous. Circles indicate values from Alonso-Perez *et al.* (2009) experimental glasses at 0·8 GPa without garnet as a fractionating phase (open blue circles), 0·8 GPa with garnet as a fractionating phase (open red circles), and 1·2 GPa where garnet was always present as a fractionating phase (filled red circles). Melt oxide values were derived using the chemometric equations of Zhang *et al.* (2017), approximating maximum Na_2O values as Na_2O wt% =100 – (sum calculated oxides + 3 wt% H_2O). BR, bulk-rock data; CM, calculated amphibole-equilibrium melt.

Depleted melts are also distinguished by moderate to high Sr/Nd values (30 to >1000), high-positive europium anomalies (Eu/Eu* >1·0), and high Al_2O_3 concentrations (up to 19 wt%) (Figs 12b and 15f). These values are unusually high for fractionated arc andesites and dacites because early crystallization of plagioclase preferentially sequesters Al, Sr relative to Nd, and Eu^{2+} relative to Eu^{3+}. The net result of plagioclase fractionation is that evolved arc melts commonly display low Al_2O_3 (<17 wt%), Sr/Nd (<100), and Eu/Eu* (<1·0). In the Malaspina Pluton, depleted amphibole-equilibrium melts show elevated values for these geochemical parameters, and they generally decrease as function of increasing SiO_2 (see Fig. 12b). Petrographic observations of the Malaspina rocks also indicate that plagioclase crystallized with or shortly after amphibole, which would result in decreasing Al_2O_3 (<17 wt%), Sr/Nd (<100), and Eu/Eu* (<1·0). Therefore, the unusually high Sr/Nd and Eu/Eu* values are primary features of the depleted melts and these values probably decreased with plagioclase fractionation.

One explanation for the unusually high Sr/Nd and Eu/Eu* values is that depleted melts formed as primary melts from diapirs of subducted basaltic melt that traversed the mantle wedge but did not chemically equilibrate with residual mantle peridotite (e.g. Marsh, 1976; Myers *et al.*, 1985, 1986*a*, 1986*b*; Brophy & Marsh, 1986; Johnston & Wyllie, 1988). This interpretation is unlikely because we observe no direct evidence for garnet as a residual phase in depleted melts. Similarly, dehydration melting of underplated basalt or gabbro at lower-crustal conditions (e.g. McCulloch *et al.*, 1987; Muir *et al.*, 1995) would result in residual garnet, which is inconsistent with our results. Another problematic issue with dehydration partial melting models is that studies of heat transfer show that arc basalts emplaced into the base of

Table 7: Melt values calculated from representative amphibole compositions

Zone:	I	I	II	II	III	IV
Classification:	Enriched	Depleted	Enriched	Depleted	Enriched	Depleted
Sample:	14NZ01C	14NZ72	14NZ87	13VA147A	13NZ38C	13NZKK27B
Grain, spot:	G2, S7	G3, S10	G3, S7	G2, S5	G4, S3	G1, S1
Major element oxides (wt%), calculated using chemometric equations from Zhang et al. (2017*)*						
SiO_2, equation (3)	61·77	62·57	67·39	60·94	60·87	62·17
TiO_2, equation (5)	0·65	0·31	0·37	0·32	0·56	0·21
FeO, equation (8)	4·34	3·99	2·7	4·4	4·58	3·38
MgO, equation (9)	1·06	1·09	0·63	1·38	1·57	0·91
CaO, equation (10)	4·77	3·91	3·3	3·71	5·41	3·8
K_2O, equation (13)	3·06	2·39	2·94	2·35	2·02	2·74
Al_2O_3, equation (14)	15·42	17·3	15·1	17·94	16·73	16·66
Temperatures used to assign partition coefficients, from Putirka (2016) pressure-independent equation (5)						
Calculated *T* (°C)	903	882	865	913	901	853
Trace element abundances (ppm), calculated using partition coefficients from Nandedkar et al. *(2016)*						
Sc	4·62	2·64	5·61	3·12	4·32	3·55
Ti	4271	1529	2841	1911	2433	1041
V	83·5	49·5	67·6	55·9	53·9	62·8
Sr	537	255	275	289	429	1298
Y	38·3	10·7	27·0	10·2	39·0	10·9
Zr	139	37·5	81·1	54·5	188·1	21·7
Nb	62·2	1·53	44·7	1·95	40·7	6·12
Ba	1704	780	359	793	1111	901
La	173	0·27	148·9	0·33	156·8	1·88
Ce	329	2·30	285	2·80	303·9	6·80
Nd	106·0	5·37	84·3	6·24	96·3	7·69
Sm	15·18	2·13	11·1	2·15	14·47	2·51
Eu	2·59	0·69	1·89	0·65	2·65	0·99
Gd	10·96	1·84	6·72	1·89	9·65	2·10
Tb	1·15	0·28	0·81	0·28	1·28	0·31
Dy	6·48	1·73	4·35	1·80	7·36	1·82
Ho	1·23	0·35	0·84	0·32	1·34	0·36
Er	3·60	1·01	2·46	1·05	4·03	1·01
Tm	0·52	0·16	0·36	0·16	0·59	0·15
Yb	3·69	1·08	2·36	1·03	4·07	1·11
Lu	0·58	0·17	0·37	0·18	0·59	0·18
Hf	2·59	0·97	1·87	1·10	3·37	0·86
Ta	2·07	0·00	2·44	0·00	1·71	0·27
Pb	86·3	23·4	88·8	34·6	67·3	54·4
Th	30·5	0·03	89·1	0·00	19·48	0·47
U	6·94	0·06	36·5	2·18	3·36	2·58

the crust cannot provide enough heat to melt amphibolitic lower crust extensively because of the high dehydration melting temperature of amphiboles in mafic rocks (~950°C) (see Petford & Gallagher 2001; Annen & Sparks, 2002; Walker *et al.*, 2015; Decker *et al.*, 2017). The production of volumetrically extensive depleted-group melts indicates that significant amounts of depleted melts were emplaced over a brief 3 Myr interval, and this is difficult to attribute to dehydration melting alone unless significant volumes of aqueous fluids were added to the arc root, potentially driving rapid fluid-fluxed melting (Collins *et al.*, 2020).

Another possibility is that depleted melts formed by extensive fractionation of more primitive arc magmas (molar Mg#>50) in which early crystallization of plagioclase was suppressed by high initial H_2O contents (>4 wt%). Suppression of plagioclase saturation would have resulted in increasing Al_2O_3, Sr/Nd, and Eu/Eu* during crystallization of plagioclase-free cumulates (e.g. Baker & Eggler, 1983, 1987; Kelemen *et al.*, 1990; Sisson & Grove, 1993*a*, 1993*b*; Müntener *et al.*, 2001). In this model, depleted-group melts would represent highly evolved hydrous melts formed via fractionation of a high-pressure Mg-rich, garnet-poor assemblage consisting primarily of clinopyroxene, orthopyroxene, and amphibole. The fractionated nature of the Malaspina melts is illustrated in Fig. 12, whereby Malaspina melts have high SiO_2 and much lower MgO and Mg#s compared with hydrous experimental basalts and andesites (Hirose & Kawamoto, 1995; Hirose, 1997). One problem with this model is that plagioclase in equilibrium with a hydrous basaltic to andesitic system is typically An-rich whereas those in the Malaspina Pluton are generally An-poor.

Although it is clear that Malaspina melts are evolved relative to hydrous experimental basalts and andesites, another explanation for their high Sr/Nd and Eu/Eu* values is that they formed in part from rejuvenation of plagioclase-rich cumulates via melt–rock interaction with a hydrous mantle-derived melt (e.g. Mazzucchelli *et al.*, 1992). Although partial melting and melt–rock reactions would enrich the resulting liquids in Sr/Nd, Eu/Sm, and Eu/Eu*, both processes would also result in high-Sr concentrations because plagioclase is highly

Table 8: Major-element oxide ranges of calculated melts compared with ranges of whole-rocks

Oxide	Calculated melts	Whole-rock
SiO_2	*55·4–70·4*	43·1–53·9
TiO_2	0·18–0·98	*0·56–1·81*
FeO	2·09–8·05	*4·75–10·77*
MgO	0·45–2·81	*2·09–6·21*
CaO	2·39–7·01	*5·05–12·35*
K_2O	*1·37–3·12*	0·45–3·04
Al_2O_3	14·7–19·3	*17·3–23·2*
Mg#	27·3–45·7	*42·2–56·1*

Values in italics are higher data-value ranges.

enriched in Sr relative to Eu (Severs *et al.*, 2009). Calculated amphibole-equilibrium melts from the depleted-melt group show only modest Sr concentrations, typically up to 300 ppm, and have lower average concentrations compared with enriched melts, which show much lower average Sr/Nd and Eu/Eu* values (Fig. 15c and 16a–c). These considerations appear to preclude plagioclase dissolution or partial melting alone; however, coupled dissolution of apatite associated with plagioclase cumulates would also strongly enrich the depleted melts in Eu but would not contribute significant Sr. Rejuvenation of cumulates at the base of the Malaspina Pluton is well documented in the Breaksea area where Malaspina and related melts disrupted the Breaksea Orthogneiss, an older high-pressure arc cumulate. In these rocks, apatite is a common accessory phase in omphacitic granulites (Clarke *et al.*, 2005; De Paoli *et al.*, 2009; Stowell *et al.*, 2017). Thus, we view the compositions of the depleted melts as being primarily derived from () an oxidized depleted mantle with a subduction-related fluid component, which was then modified by (2) melt–rock interactions in the lower crust with pre-existing plagioclase + apatite cumulates. We discuss field observations for melt–rock interactions with cumulates in the following section.

Contributions from crustal sources (subducted sediments)

Evidence for contamination and/or mixing with a crustal source is prevalent in the enriched-melt group, which is characterized by enrichment in HFSE and LREE (Fig. 14c and d). Compared with N-MORB, enriched melts have prominent positive anomalies in fluid-mobile LILE such as Ba, U, K, Pb and Sr, and are also enriched in HFSE such as Th, Nb, Ta, and Zr, which are commonly considered immobile in aqueous fluids (Figs 14d and 15a–d). Grove *et al.* (2002) suggested that >99 % of the incompatible trace element budget in the Shasta andesites was supplied by a sediment-dominated fluid-rich component. Compared with arc andesites and dacites from Mt Shasta, Malaspina melts display even greater enrichment in both LILE and HFSE (Fig. 14c and d). Whereas a subduction-fluid component can explain the observed enrichment in LILE, enrichment in HFSE is difficult to attribute to a subduction fluid alone, owing to their immobility in most fluids (Grove *et al.*, 2003). High concentrations of Th (and other HFSE) in the enriched group are attributable to the incorporation of sediment melt because Th is enriched in continental sediments (Plank, 2005), and experimental studies of peridotite/fluid and eclogite/fluid partioning show that it is insoluble in aqueous fluids (Brenan *et al.*, 1995a, 1995*b*, 1996; Ayers *et al.*, 1997; Kogiso *et al.*, 1997; Tatsumi & Kogiso, 1997; Stalder *et al.*, 1998; Johnson & Plank, 1999). Hermann & Rubatto (2009) also showed that the stability of accessory phases in subducted sediment profoundly influences the trace-element characteristics of hydrous melts and their stability is primarily a function of temperature. Thus, elevated concentrations of HFSE indicate that enriched melts require a crustal contribution, and because these elements are typically mobile only in silicate melts (rather than fluids), the source of the trace-element enrichment points towards a sediment–melt component.

The enriched-melt group is also characterized by flat MREE to HREE patterns in chondrite-normalized REE plots, and relative to the depleted-melt group, they have similar Dy/Yb_N and relatively lower Sr/Nd (Figs 14c, d and 16a). Compared with primitive andesites from the Aleutians, where garnet is proposed to have played an important role as a residual phase (Kelemen *et al.*, 2014), Dy/Yb_N values are generally lower, and Sr/Y values are also low compared with melts in equilibrium with garnet as a residual or fractionating phase (Fig. 15e). One sample, 13VA206A, shows a weak trend towards higher Dy/Yb_N and higher Sr/Y, although average REE abundance patterns show flat MREE to HREE patterns. It is possible that minor garnet was present in this sample as a fractionating phase, or that the sample represents a hybrid with garnet-bearing melt (Fig. 15e and 16a). Enriched-melt samples also have very high average La/Yb and Th/Yb values at low Sr/Nd values, which lends support to the presence of a sediment component (Fig. 16b and d).

Radiogenic isotopes are particularly sensitive indicators of crustal contamination and offer the potential to quantify relative contributions of crust and sediment in arc magmas. Bulk-rock Sr-, Nd-, and Pb-isotope data are shown in Fig. 11a and c together with Pacific–Antarctic MORB, data from the Anita Peridotite, and data from Eastern Province sediments of New Zealand, which represent parts of the Mesozoic accretionary prism. In Sr–Nd space, Malaspina bulk-rocks plot near Bulk Silicate Earth and show little isotopic variation (Fig. 11a). When enriched and depleted samples are plotted together, we observe no distinction between the two groups despite differences in amphibole-equilibrium melt trace-element concentrations (Fig. 11a inset).

We modeled possible melt sources via assimilation–fractional crystallization modeling in Fig. 11. Results show that both melt groups of the Malaspina Pluton can be described as mixtures between Pacific–Antarctic MORB and Eastern Province sediments. Pb-isotope modeling of Malaspina and other lower-crustal rocks of

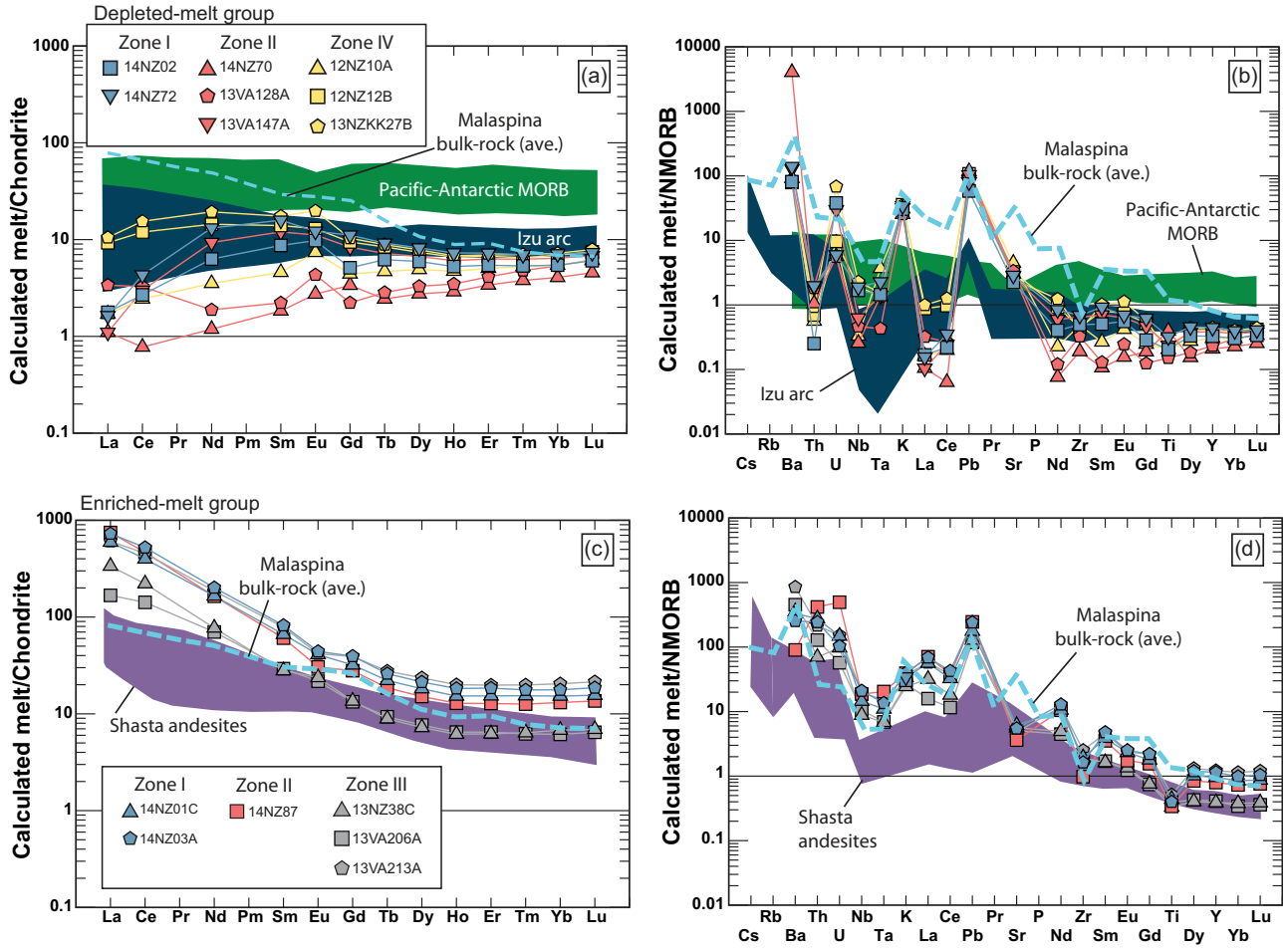

Fig. 14. Rare earth element diagrams of calculated-melt data averages normalized to chondritic values and N-MORB values, after Sun & McDonough (1989). (a, b) Depleted-melt group samples 14NZ02, 14NZ72, 13VA128A, 13VA147A, 12NZ10A, 12NZ12B, and 13NZKK27B. (c, d) Enriched-melt group samples 14NZ01C, 14NZ03A, 14NZ87, 13VA206A, 13VA213A, and 13NZ38C. Melt values were derived for each amphibole spot using partition coefficients from Nandedkar *et al.* (2016) at temperatures calculated using Putirka (2016) pressure-independent equation (5) and then plotted as an average value for each sample. Pacific–Antarctic MORB are from Hamelin *et al.* (2010), Izu arc data from Kimura *et al.* (2010), and Shasta data from Grove et *al.* (2002).

the Western Fiordland Orthogneiss shows similar results (Fig. 11b and c) and gives sediment contribution values ranging from ~1 to 10 %. Although data are limited, similarities in Pb isotopes between lower- and middle-crustal rocks throughout Fiordland suggest that contamination of Eastern Province sediments was an important source of radiogenic isotopes in Mesozoic magmas throughout the Median Batholith, not only the Malaspina Pluton (Fig. 11b and c). Although relative contributions of sediment are dependent on various parameters including Sr, Nd, and Pb concentrations and relative mass crystallized/mass assimilated (*r* value), our modeling results demonstrate that small degrees of sediment contribution (~1–10 %) can explain the observed variation in radiogenic isotope compositions of both enriched- and depleted-group melts. These results are also consistent with zircon Hf- and O-isotope modeling that demonstrates that Malaspina melts were predominantly mantle-derived and were contaminated with 10–20 % recycled subducted trench sediments (Decker *et al.*, 2017; Schwartz *et al.*, 2021).

A surprising feature of the Malaspina Sr–Nd whole-rock isotope data is that radiogenic isotopes show very little variation between enriched- and depleted-melt groups despite stark differences in amphibole-equi librium melt trace-element compositions. This homogeneity points to a common isotopic source and suggests that stable- and radiogenic-isotope signatures were acquired in the melt source region. The most likely possibility to explain the homogeneity in both groups is that they were sourced from partial melting of a metasomatized asthenospheric mantle that obtained its enriched isotopic signature from the same subducted sediment source (e.g. Fig. 1). Thus, we view the Malaspina melts as having at least three distinct components: (1) an oxidized depleted mantle source that produced a hydrous mafic to intermediate melt with N-MORB-like characteristics; (2) a sediment fluid and sediment melt with isotopic characteristics similar to those of Eastern Province sediments; (3) a plagioclase + apatite cumulate that was rejuvenated by melt–rock interaction with the hydrous melts.

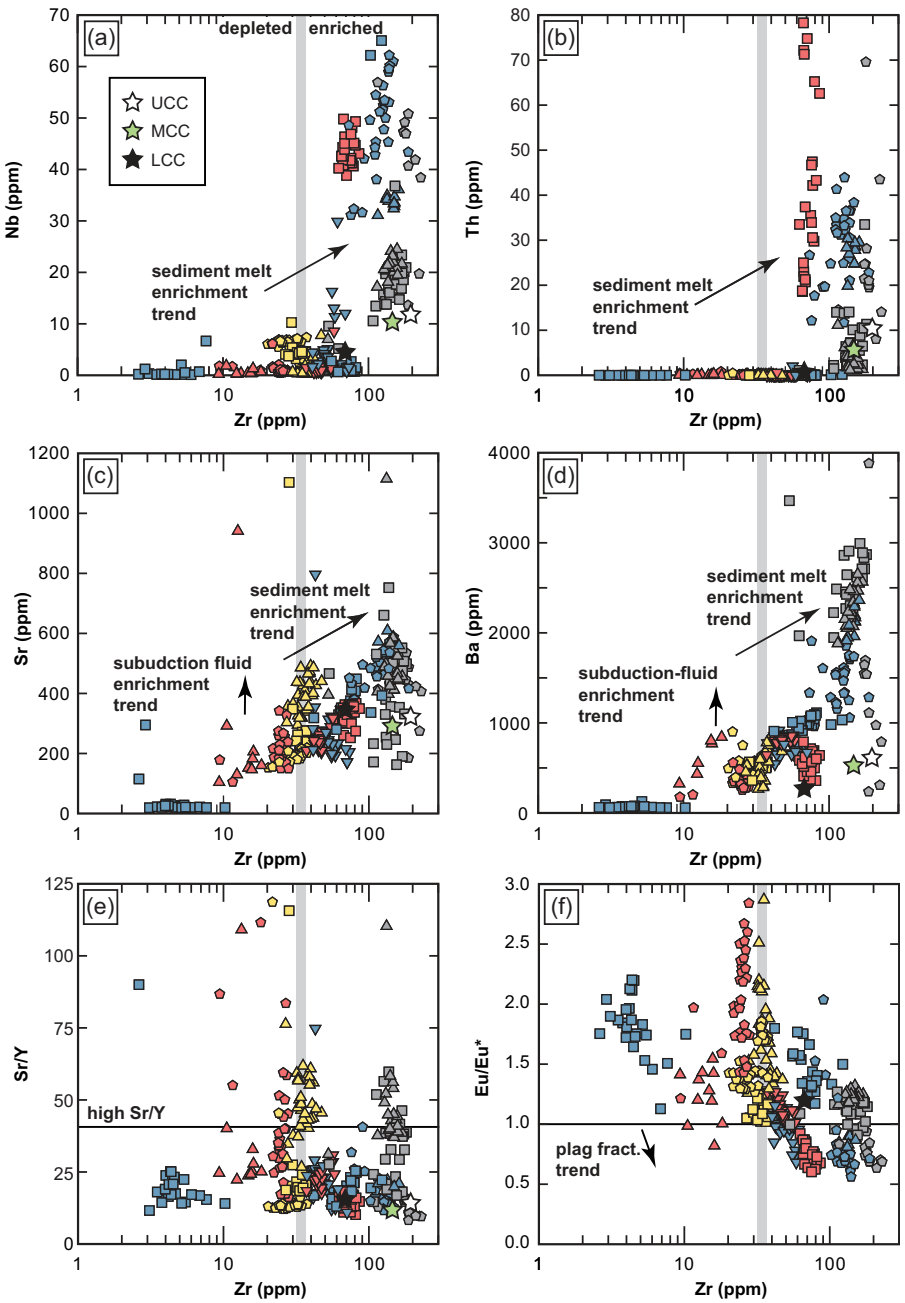

Fig. 15. (a–e) Bivariate plots of trace-element abundances for calculated melts. (a, b) High field strength elements (Nb and Th); (c, d) large ion lithophile elements (Sr and Ba). Relative enrichment and depletion is apparent in elements Nb, Th, and Ba; sample values overlap extensively in Sr. (e) Ratio of a large ion lithophile element to a high field strength element (Sr/Y). Sr/Y $>$ 40 is the defining criterion for the adakite signature, in accordance with Defant & Drummond (1990). (f) Eu/Eu* $=$ 1 indicates no Eu anomaly; Eu/Eu* is calculated as $(Eu/0{\cdot}058)/[(Sm/0{\cdot}153)(Gd/0{\cdot}2055)]^{1/2}$. Results are the same as if Eu/Eu* is calculated as $(Eu/0{\cdot}058)/[(Sm/0{\cdot}153)^2(Tb/0{\cdot}0374)]^{1/3}$. Melt values were derived for each amphibole spot using partition coefficients from Nandedkar *et al.* (2016) at temperatures calculated using Putirka (2016) pressure-independent equation (5). Gray bars indicate the division between enriched and depleted groups. UCC, upper continental crust; MCC, middle continental crust; LCC, lower continental crust [all values from Rudnick & Gao (2003)].

Evidence for the possible origin of deep lithospheric melts beneath the arc is preserved in the Anita Peridotite (northwestern Fiordland; Fig. 2), where a unique section of the upper mantle lithosphere is preserved. Czertowicz *et al.* (2016) proposed that metasomatized peridotites in this region were formed by melt–rock interactions between a mafic silicate melt and depleted mantle peridotite, and they suggested that these melts were associated with construction of lower arc crust and the Western Fiordland Orthogneiss. In Sr–Nd space, the Anita Peridotites is distinct from the Malaspina Pluton with higher Sr- and Nd-isotope values (Fig. 11a). They are also more radiogenic in Sr isotopes relative to Pacific–Antarctic MORB, and they do not fall

along our two-component AFC model (Fig. 11a). Peridotites also display similarities to OIB-type melts (Czertowicz *et al.*, 2016), although we do not see OIB characteristics in the Malaspina bulk-rocks nor in amphibole chemistry. Bulk-rock Pb isotopes in the Anita Peridotite do overlap those in the Malaspina Pluton; however, the peridotite compositions also extend towards much more radiogenic values and show far greater variability compared with the Malaspina Pluton and the Western Fiordland Orthogneiss (Fig. 11b and c). Although amphiboles in the Anita Peridotite have low concentrations of HFSE and would be considered 'depleted' according to our classification, they are also distinct in major element compositions from amphiboles in the Malaspina Pluton, being predominantly tremolitic with high Si values ranging from 6·5 to 8 a.p.f.u. Although there are many differences between the melts that fluxed through the Anita Peridotite and those we observe in the Malaspina Pluton, the preservation of the upper mantle lithosphere beneath Fiordland warrants further investigation between these upper mantle rocks and the lower crust in the Median Batholith.

Homogeneity, interconnectivity, and magma chamber geometry

Conceptual and numerical models commonly envision that emplacement and melt diversification occur via successive emplacement of sills into pre-existing crust and crystal mush (Annen *et al.*, 2006; Solano *et al.*, 2012), yet there are few constraints from field observations on the architecture of lower-crustal melt storage regions (see schematic illustration in Fig. 1). Similarly, we know relatively little about the efficiency and length-scale of melt homogenization in these lower-crustal regions. Field observations and igneous amphibole geochemical data from the Malaspina Pluton provide rare insights into these processes including mechanisms of melt emplacement, melt diversification, and the degree of melt interconnectivity in the lower crust. As discussed above, our data reveal that igneous amphiboles form two chemically distinct groups (enriched and depleted), implying that lower-crustal melts were inefficiently homogenized, and had no long-range interconnectivity (Fig. 3b). At the kilometer-scale, amphiboles in the melt feeder zone (Zone I) are both enriched and depleted and can be as closely spaced as ~1 km apart (see 14NZ01C to 14NZ02 to 14NZ72 in Fig. 3b), although sub-kilometer spacing is lacking in our dataset. The spatial locations and diverse amphibole compositions of our samples are inconsistent with formation in a large system of well-mixed magmas and instead support field observations for incremental growth by batchwise intrusion of sills with little post-emplacement communication (Klepeis *et al.*, 2016).

In addition to trace-element data, the mineralogy of igneous sheets also supports sequential intrusion and limited long-range melt communication. For example, sheets in Zones I and III consist of hornblende + plagioclase ± clinopyroxene ± orthopyroxene ± biotite, whereas sheets in Zones II and IV lack pyroxenes and the dominant magmatic assemblage consists exclusively of hornblende + plagioclase ± biotite (Figs 3b and 4; Table 1). This distribution in igneous modal mineralogy is also inconsistent with widespread melt homogenization, and the spatial distribution of samples also precludes simple lateral flow from a single subvertical feeder zone (Fig. 3c). These observations, especially the presence of enriched and depleted types in Zone I, provide further evidence that melts were sourced from more than one melt reservoir where variations in composition and/or H_2O content led to the presence or absence of pyroxene (e.g. Blatter *et al.*, 2017).

Although melts in the Malaspina Pluton do not appear to have been efficiently homogenized at the kilometer-scale, our data do show spatial organization indicated by groupings of primarily enriched melts in Zone I and Zone III, and depleted melts in Zones II and IV. This geographical distribution could reflect interconnectivity of melts within these zones, or, more probably, an underlying network of melt-transportation channels tapping deeper melt-storage reservoirs. The latter suggestion is supported by the orientation of magmatic foliations and lineations, which shows that most exposures of the Malaspina Pluton, with the exception of Zone IV, represent the uppermost portion of the plutonic complex along with a feeder zone and roof, which consists of magmatic sheets structurally below the Deep Cove Gneiss (Fig. 3c) (Klepeis *et al.*, 2016). Sheets emanating from the subvertical feeder zone define a mushroom-shaped igneous body (Klepeis *et al.*, 2016); however, because only the uppermost structure of the Malaspina Pluton and roof are exposed in Zones I–III, it is plausible that there were additional melt conduits at deeper levels beneath Zones II and III, and they may have once fed sheeted intrusions with trace-element depleted and enriched melts, respectively. Because the geographical distribution of melts cannot be explained by magmatic flow from a single feeder zone, we conclude that multiple feeder zones are required to explain the spatial and chemical distribution of melts in the Malaspina Pluton.

Structural mapping of the Malaspina Pluton shows that roof and base are exposed, and this permits investigation of processes that resulted in melt diversification at multiple vertical levels within the lower crust (e.g. Klepeis *et al.*, 2016). The base of the Malaspina Pluton is preserved in Zone IV where trace-element depleted amphiboles crystallized in sheets that were injected into a pre-existing dense root composed predominantly of garnet pyroxenite, pyroxenite, and garnet granulite. This garnet-rich pyroxenite root crystallized at *c.* 124 Ma and *c.* 1·8 GPa, and predated emplacement of Malaspina-related melts by 9–6 Myr (Tulloch & Kimbrough, 2003; De Paoli *et al.*, 2009; Klepeis *et al.*, 2016; Milan *et al.*, 2016; Schwartz *et al.*, 2017; Stowell *et al.*, 2017). The intrusion of Malaspina melts into the base of the arc functioned to thermally and

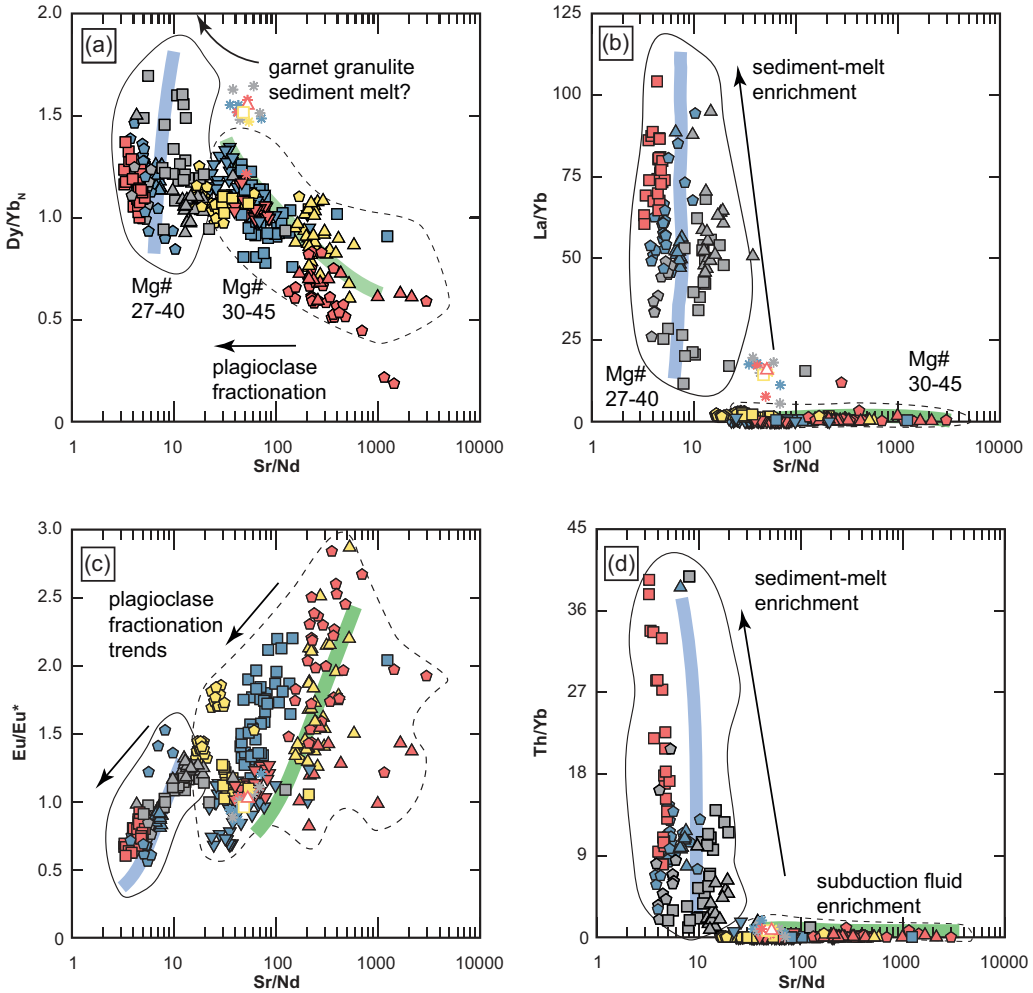

Fig. 16. Bivariate plots of calculated-melt data for trace-elemental ratios vs Sr/Nd. Green and blue lines indicate trend lines. Continuous lines show enriched-melt group, and dashed lines show the depleted-melt group. Dy/Yb_N is chondrite-normalized Dy/Yb using C1 chondrite values from Sun & McDonough (1989). Eu/Eu* calculated as $(Eu/0{\cdot}058)/[(Sm/0{\cdot}153)(Gd/0{\cdot}2055)]^{1/2}$.

mechanically disrupt pre-existing cumulates, resulting in crustal anatexis, eclogite- or granulite-facies metamorphism, and vertical flow of hot, partially molten lower crust. The upward vertical flow of melts and the entrainment of the garnet-pyroxenite xenolithic material from the Breaksea Orthogneiss represents another mechanism of melt transport, which facilitated vertical transport of melt from deeper storage regions in the arc root (Betka & Klepeis, 2013; Klepeis *et al.*, 2016).

Crustal anatexis in this region primarily involved partial melting of plagioclase-rich garnet granulites of the Breaksea Orthogneiss, which were still hot but solid enough to break and become entrained within Malaspina melts (Klepeis *et al.*, 2016). In contrast, field observations from contact aureoles of the Malaspina Pluton show little evidence for partial melting of metasedimentary wall rock, and metamorphic temperature estimates show that rocks outside the contact aureole were insufficiently heated to produce large volumes of melt (Allibone *et al.*, 2009*b*; Daczko *et al.*, 2009). The limited involvement of metasedimentary host rocks in magma evolution is also supported by zircon O- and Hf-isotope modeling of assimilation, which indicates 10–20% contamination by high-$\delta^{18}O$ metasedimentary rocks (Decker *et al.*, 2017; Schwartz *et al.*, 2021).

Amphibole crystallization temperatures also provide insights into the thermal architecture of the Malaspina Pluton during melt emplacement, storage, and crystallization. We find that throughout the Malaspina Pluton amphibole temperatures range from ~960 to 830 °C, and there is no apparent difference between temperatures of enriched and depleted amphiboles nor is there any difference in intrasample crystallization ranges (see bold versus non-bold symbols in Fig. 9c). Although there is no overall difference in temperature between the two groups, we do observe variations in temperature between closely spaced samples, which suggest that there was heterogeneity in the initial temperatures of melt intrusions. For example, samples 12NZ10A (938–923 °C) and 12NZ12B (869–854 °C) were collected in Zone IV in close proximity and barely overlap when considering analytical uncertainties in individual measurements (~30 °C) (Fig. 9c). We also do not observe a difference in temperature between

amphiboles at the roof of the pluton (Zones I–III) versus amphiboles from the base of the pluton in the disrupted cumulate zone (Zone IV). These features indicate that Malaspina melts were emplaced as distinct sheets emanating from several deeper reservoirs, each with different thermal and chemical characteristics. Emplacement of these melt batches probably occurred into a crystal-rich mush zone whereby melts cooled as discrete batches with little apparent communication with other batches.

Crystallization pressures and the role of garnet in arc root production

Al-in-hornblende pressures for the Malaspina Pluton (0·92 GPa) are consistent with a deep-crustal origin, and high-pressure crystallization experiments of andesitic melts also show that garnet becomes stable as a crystallizing phase at similar, although slightly higher pressures (~1·0–1·2 GPa: Alonso-Perez *et al.*, 2009; Ulmer *et al.*, 2018). Thus, a key question in our study is whether geochemical data from igneous amphibole are consistent with garnet in the source or as a crystallizing phase, and to what extent did the Malaspina Pluton produce a garnet-bearing arclogite (garnet + clinopyroxene) root. Our data show that amphibole-equilibrium melts provide little evidence for garnet in the petrogenesis of Malaspina melts (see Figs 12, 16 and 17a, b). Because HREE and yttrium are compatible in garnet, concentrations of these elements in melts in equilibrium with garnet should be low, and MREE to HREE ratios should be high, resulting in high Sr/Y (>40), La/Yb (>6) and Dy/Yb_N (>1·5) (e.g. Davidson *et al.*, 2007). In contrast to these predictions, chondrite-normalized REE abundance patterns in amphibole-equilibrium melts show flat chondrite-normalized HREE patterns, low La/Yb (<4·0) and Dy/Yb_N (<1·5), and Sr/Y values generally do not exceed 40 (Figs 14–17). Rare earth element data from igneous zircons in the Malaspina Pluton also show steep MREE to HREE patterns in chondrite-normalized plots, which also does not support co-crystallization of zircon and garnet in the temperature range of 950–750 °C (Schwartz *et al.*, 2017).

Malaspina amphibole-equilibrium melt compositions also trend from metaluminous to peraluminous compositions (Fig. 13) and these results are consistent with experimental results at pressures ranging from 0·7 to 1·2 GPa, whereas at higher pressures, garnet precipitation inhibits melt evolution towards peraluminous compositions (Sisson & Grove, 1993; Müntener *et al.*, 2001; Müntener & Ulmer, 2006; Alonso-Perez *et al.*, 2009). In experiments of andesite fractionation, Alonso-Perez *et al.* (2009) noted that amphibole fractionation is dominantly responsible for controlling major-element characteristics of derivative melts, resulting in trends towards high SiO_2 contents and peraluminous compositions like those we observe (Fig. 13d). Garnet, on the other hand, has high Fe/Mg solid/liquid partition coefficients and hence tends to produce 'high-Mg' liquids. Malaspina melts have very low MgO values (<3 wt%) and low molar Mg#s (<45) (Table 8). These features are consistent with amphibole and/or pyroxene fractionation because these minerals have considerably lower Fe/Mg solid/liquid K_D values, and therefore extract Mg more efficiently, leading to lower FeO*/MgO liquids at a given SiO_2 content (Alonso-Perez *et al.*, 2009). Thus, our results are in line with experimental studies of andesite or dacite crystallization at 0·8–0·9 GPa, but contrast with experiments at >1·2 GPa, which contain garnet and lack amphibole except at high H_2O contents (>6 wt%) (Müntener *et al.*, 2001; Alonso-Perez *et al.*, 2009; Blatter *et al.*, 2017; Ulmer *et al.*, 2018).

Although bulk-rock geochemical data have been used to argue for garnet involvement, field studies of the Malaspina Pluton rarely show evidence for garnet as a primary igneous crystallizing phase (e.g. Oliver, 1977, 1980; Ward, 1984; Davids, 1999; Klepeis *et al.*, 2007, 2016; Allibone *et al.*, 2009*a*; his study). The one exception is in the Malaspina Pluton in Acheron Passage (Zone III, Fig. 3a), where Chapman *et al.* (2016) reported possible igneous garnet in high-strain, garnet-bearing diorites. In this same area, Allibone *et al.* (2009*a*) and Klepeis *et al.* (2016) also reported xenolithic rafts of garnet pyroxenite enveloped with Malaspina orthogneiss (see location of sample 13NZ38C; Fig. 3b). Similar garnet-bearing pyroxenitic rafts are reported in the nearby Resolution Orthogneiss where Malaspina-related melts rejuvenated and disrupted high-pressure cumulates once occupied by the older Breaksea Orthogneiss (Betka & Klepeis, 2013; Klepeis *et al.*, 2016). Thus, it is unclear whether garnet reported in this region is related to Malaspina crystallization or disruption and entrainment of garnet pyroxenite from the older Breaksea Orthogneiss during vertical flow of melts from deeper levels (Betka & Klepeis, 2013). This location withstanding, our amphibole-equilibrium melt data, Al-in-hornblende pressure estimates, and phase equilibria considerations all support the notion that Malaspina melts were dominantly hydrous andesites or dacites that differentiated by fractionation of amphibole + clinopyroxene + plagioclase from ~960 to 830 °C at pressures of ~0·9–1·0 GPa. Garnet does not appear to have been stable as a primary igneous phase and there is no significant evidence for garnet in the source region. An implication of this observation is that fractionation of Malaspina melts would not have produced a thick garnet-bearing ultramafic root at the level of emplacement, and there is no geochemical evidence for deeper garnet fractionation either. This observation implies that there was little production of a dense and gravitationally unstable root from the crystallization of the Malaspina Pluton. Consequently, our results predict limited arc-root foundering after emplacement of the Malaspina Pluton as suggested by Chapman *et al.* (2017) based on other metamorphic phase transformation considerations.

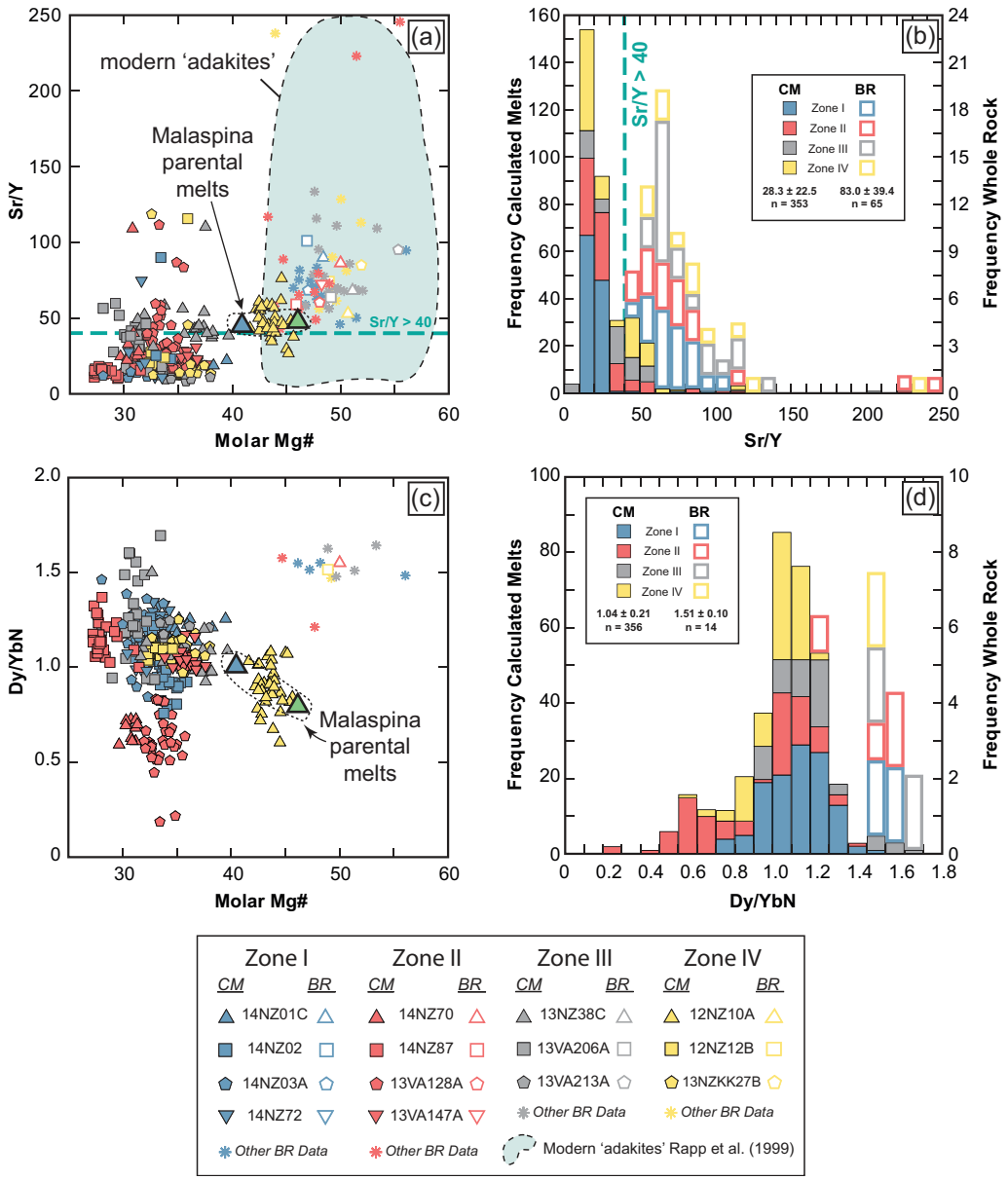

Fig. 17. Comparison of whole-rock data and calculated-melt data for trace-elemental ratios. (a) Bivariate plot of melt Sr/Y vs molar Mg#; modern adakite field was compiled from Rapp *et al.* (1999) and Decker *et al.* (2017). (b) Histogram of Sr/Y for calculated-melt and whole-rock data. Sr/Y > 40 is the defining criterion for the adakite signature, in accordance with Defant & Drummond (1990). (c) Bivariate plot of melt Dy/Yb_N vs molar Mg#; Dy/Yb_N is chondrite-normalized Dy/Yb using C1 chondrite values from Sun & McDonough (1989). (d) Histogram of Dy/Yb_N for calculated-melt and whole-rock data. Molar Mg# is calculated from melt oxide values derived using the chemometric equations of Zhang *et al.* (2017); molar Mg# = 100MgO/(MgO + FeO + 0·8998Fe_2O_3), where the oxides are first divided by their molecular weights. Melt trace-element values were derived for each amphibole spot using partition coefficients from Nandedkar *et al.* (2016) at temperatures calculated using Putirka (2016) pressure-independent equation (5). BR, bulk-rock data; CM, calculated amphibole-equilibrium melt.

Reconciling discrepancies between bulk-rocks and amphibole-equilibrium melts: are bulk-rocks cumulates?

Although previous workers have used the bulk-rock geochemistry of the Malaspina Pluton to evaluate the magmatic evolution of the lower crust and the production of a garnet-bearing arc root (e.g. McCulloch *et al.*, 1987; Muir *et al.*, 1995; Tulloch & Kimbrough, 2003; Chapman *et al.*, 2016), amphibole-equilibrium melts in this study diverge significantly from bulk-rock compositions both in terms of major-element oxides and trace elements, and especially Sr/Y and Dy/Yb (Table 8; Figs 12, 14, 15 and 17). The latter are key geochemical parameters that have been used to argue for the production of a thick garnet-bearing root in the Early Cretaceous, an interpretation that we dispute here (Fig. 17). We find that calculated amphibole-equilibrium melt compositions are much more felsic than corresponding bulk-rock data and as discussed above they have lower Sr/Y and Dy/Yb values that do not support

the involvement of garnet as a fractionating phase (Figs 15e and 17a–d). Estimated parental melt compositions are also on average more felsic than bulk-rocks, and they have lower Sr/Y and Dy/Yb compared with bulk-rocks. The compositional discrepancy between calculated melts and bulk-rock data raises the question of whether chemometric equations and partition-coefficient calculations faithfully approximate melt compositions, or whether bulk-rocks represent cumulates from which melt has been extracted (Werts *et al.*, 2020).

Although the Zhang *et al.* (2017) chemometric equations are relatively new and require further corroboration from experimental and field studies, one way to evaluate equilibrium between measured amphibole compositions and calculated melts is to calculate Fe–Mg exchange coefficients [$K_D(Fe–Mg)^{Amph\text{-}liq}$] and compare them with the known range of experimental values (Putirka, 2016). Using amphibole-equilibrium melt compositions, we calculate Fe–Mg exchange coefficients ranging from 0·3 to 0·6, which overlap experimental values (0·1–0·4: Putirka, 2016). The broad range we observe is skewed towards higher Fe–Mg K_D values compared with experiments and may reflect a slight systematic underabundance of calculated FeO_{melt} or an overabundance of calculated MgO_{melt} values. In contrast, Fe–Mg exchange coefficients calculated using bulk-rock values give unreasonable values ranging from 0·8 to 1·0, indicating that bulk-rock values cannot be considered in equilibrium with amphiboles. Magmatic clinopyroxenes are also not in equilibrium with bulk-rock values, but are in equilibrium with amphibole-equilibrium melts (Brackman *et al.*, 2019). Thus, Fe–Mg exchange coefficient data from two separate mineral phases indicate that amphibole-equilibrium melts are a close approximation to liquid compositions from which igneous amphiboles and clinopyroxenes crystallized and this is supported by phase equilibria considerations discussed above.

Independently determined amphibole crystallization temperatures also provide a means of evaluating amphibole melt conditions (Fig. 9). Amphiboles in equilibrium with basaltic to andesitic melts such as those predicted by bulk-rock values are expected to crystallize at temperatures in excess of 1050 °C (Müntener *et al.*, 2001). In contrast, Malaspina amphibole temperatures range from 960 to 830 °C and are consistent with crystallization from dominantly andesitic to dacitic melts like those we observe in calculated-melt data (Table 7). Thus, amphibole thermometry and Fe–Mg exchange coefficient considerations from major element data collectively indicate that chemometric equations produce reasonable melt compositions and bulk-rock compositions are probably not in equilibrium with igneous amphiboles nor clinopyroxenes.

Calculated trace-element compositions in amphi bole-equilibrium melts are also at odds with bulk-rock values, and so we explored a number of amphibole–melt partition coefficients (Schnetzler & Philpotts, 1970; Klein *et al.*, 1997; Nandedkar *et al.*, 2016; Shimizu *et al.*, 2017). Results of our calculations indicate that bulk-rock values are always significantly different from calculated values. For example, calculated-melt values are always higher in Y concentrations (up to 60 ppm) yielding low-Sr/Y values (<40) compared with bulk-rock values (>40). Calculated-melt values also show flat MREE to HREE abundances in chondrite-normalized REE plots and have low Dy/Yb_N (<1·5) in contrast to bulk-rock values (Tulloch & Kimbrough, 2003). These calculated values are difficult to attribute to garnet as an important crystallizing or residual phase. Brackman *et al.* (2019) observed the same geochemical discrepancy between bulk-rocks and igneous clinopyroxene compositions in the Malaspina Pluton, and they concluded that bulk-rocks are predominantly cumulates. Amphibole data support these findings, and we view bulk-rock as primarily reflecting plagioclase + clinopyroxene + amphibole accumulation rather than melt compositions.

Evidence to support crystal accumulation and melt loss also comes from zircon saturation thermometry (Watson & Harrison, 1983). Calculated Zr/Hf values in amphibole-equilibrium melts indicate that zircon was a fractionating phase for all samples from ~925 to 830 °C (Fig. 9a and b). These temperatures overlap Ti-in-zircon temperatures, which indicate that zircon was a crystallizing phase from 975 to 825 °C (green histograms in Fig. 9b) (Schwartz *et al.*, 2017). In contrast, bulk-rock data yield zircon saturation temperatures ranging from 760 to 615 °C. Isochemical pseudosection modeling of Malaspina bulk-rock data show that these values are at or below the wet solidus (760–700 °C) for pressures ranging from 0·5 to 1·5 GPa (Stowell *et al.*, 2014). Moreover, for zircon to be saturated in Malaspina bulk-rock compositions at 925 °C, melts would require 1200–2000 ppm Zr, which is 5–45 times greater than observed bulk-rock zirconium concentrations (33–233 ppm: Supplementary File). Although Malaspina bulk-rock compositions are at the lower limit of experimental compositions in the Watson & Harrison (1983) study, these calculations serve to show that bulk-rock Zr data are far too low to precipitate zircon in these rocks [see also Barnes *et al.* (2020) for discussion of zircon saturation and cumulates]. In contrast, saturation of zircon in amphibole-equilibrium melts requires much less Zr in the melt and this is consistent with our trace-element compositions. Thus, we conclude that Malaspina bulk-rock values are unlikely to represent liquid compositions and they are best viewed as cumulates.

Construction of lower continental arc crust

A model for the chemical architecture of the Malaspina Pluton is illustrated in Fig. 18, which shows the construction of the lower crust via batchwise sill emplacement. In this model, enriched and depleted melts were emplaced at 118–115 Ma as a series of 100–2000 m thick andesitic to dacitic sheets into a pre-existing cumulate zone that was once occupied by the older Breaksea

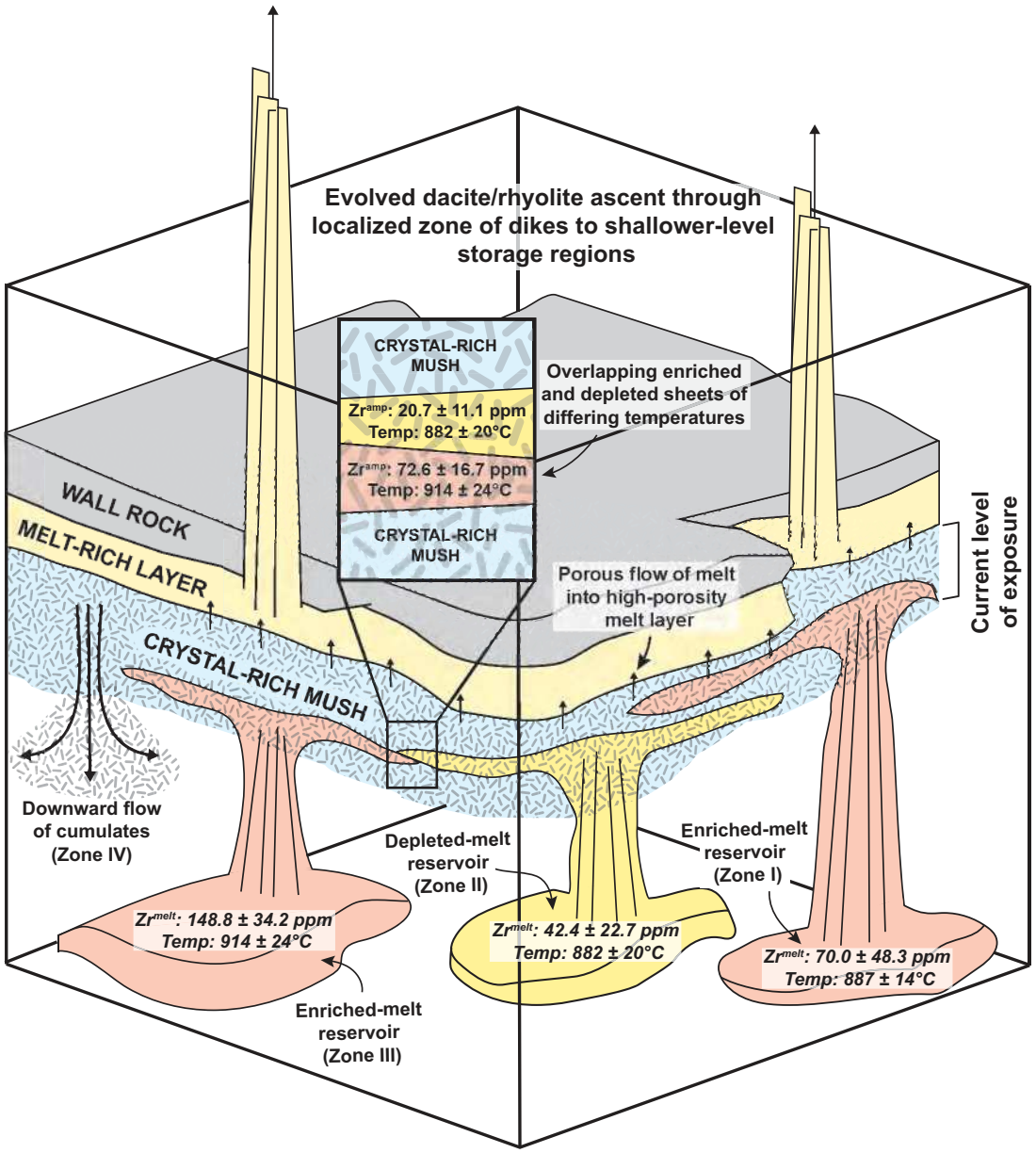

Fig. 18. Malaspina MASH zone schematic illustration displaying deeper storage reservoirs for the zones from this study with average amphibole crystallization temperatures [Putirka, 2016, pressure-independent equation (5)] and calculated-melt Zr concentrations, crystal–liquid segregation into melt-rich and crystal-rich layers, melt transport through porous layers, cumulate downflow, and zones of vertical ascent. Current level of exposure is shown to include the crystal mush (present-day Malaspina Pluton), preserved subvertical melt transport in Zone I, preserved subhorizontal structures in Zones II and III, and portions of the intruded wall rock (Deep Cove Gneiss). Current level of exposure is approximate, as the melt-rich layer was not preserved in the geological record. Inset shows one simplified example of layered sequences and their thermal and chemical differences, using amphibole Zr concentrations. After Solano *et al.* (2012).

Orthogneiss (*c.* 124 Ma) (Klepeis *et al.*, 2016). More primitive melts are less common, although we speculate that parental melts were basaltic andesites and they produced a significant amphibole + clinopyroxene + plagioclase cumulate root (Fig. 12). The roof of the MASH or hot zone was capped by the Paleozoic Deep Cove Gneiss, and the base consisted of disrupted and rejuvenated older cumulates consisting of garnet-pyroxenite, pyroxenite, and garnet granulite (De Paoli *et al.*, 2009; Clarke *et al.*, 2013; Klepeis *et al.*, 2016; Stowell *et al.*, 2017). Melts were fed from multiple feeder zones that tapped deeper melt-storage regions, which were variably enriched in fluids and melt derived from subducted trench sediments. Successive emplacement of melts into the lower crust created a crystal-rich mush zone with ambient temperatures ranging from at least 960 to 750 °C for *c.* 3 Myr. Within the accumulating crystal-mush zone, melts were emplaced in batches such that there was no long-range (kilometer-scale) chemical homogenization as opposed to a large melt-rich magma body that was well mixed from convective stirring.

We speculate that melts may have migrated out of the crystal-rich zone into an overlying melt-rich layer via diking (Klepeis *et al.*, 2004; Marcotte *et al.*, 2005) or porous flow as documented in portions of the lower crust in northern Fiordland (Stuart *et al.*, 2018). Although we specifically avoided textures associated with porous reactive flow (see Methods above), it is likely that melt migration occurred during compaction, and melts may have temporarily pooled in an ephemeral melt-rich layer where chemical interconnectivity and hybridization would have been enhanced. Modeling of lower-crustal hot zones by Solano *et al.* (2012) observed that lower-crustal sills exist dominantly as a crystal mush, which consists mostly of solid crystals with small amounts of interstitial residual melt. As crystals accumulate via compaction and density filtering, melts migrate upward along grain boundaries and pool as high-porosity layers above the crystal cumulates. This movement alters the composition of the melts as they chemically equilibrate with the matrix crystals at successively decreasing temperatures. Modeling results also show that residual melts can induce partial melting of the surrounding crust and assimilate small amounts of this melt, leading to further diversification of magmas (Annen *et al.*, 2006; Solano *et al.*, 2012). Direct evidence for the migration of liquids in a crystal mush is observed in the Malaspina Pluton, where some dikes show hypersolidus foliations concordant with host diorite indicating crystal coupling in a melt-poor region (see fig. 8a and b of Klepeis *et al.*, 2016). In other cases, flow inside the dike wall is decoupled from the crystal-rich host, indicating efficient flow within the dike under melt-rich conditions (see fig. 8c of Klepeis *et al.*, 2016). Geochemically, the low bulk-rock Zr concentrations in the Malaspina Pluton also require that incompatible-enriched melts were lost at some point, and they probably fed overlying melt storage regions. The discrepancy in trace element characteristics between the bulk-rocks and calculated melts also suggests that these melts were lost, and the bulk-rocks are a poor proxy for melt compositions in this system. Porous flow is also observed in the Pembroke Granulite, northern Fiordland, where Stuart *et al.* (2017, 2018) documented melts travelling along pre-existing foliations and high-strain zones in surrounding rocks, inducing partial melting, and altering melt chemistry.

Vertical migration of melts out of the melt-rich layer to higher-crustal levels was also aided by intra-arc transpression and crystal-plastic deformation along mylonitic shear zones, which led to the emplacement of various evolved magma chambers in the middle and upper crust in Fiordland (Klepeis *et al.*, 2004; Marcotte *et al.*, 2005; Buriticá *et al.*, 2019). Coeval granodioritic to granitic plutons are represented in central, eastern, and southern Fiordland and comprise the Separation Point Suite, which was emplaced at pressures of 0·2–0·6 GPa (Allibone *et al.*, 2007, 2009*a*, 2009*b*; Scott *et al.*, 2011) (see light green plutons in Fig. 2). Thus, the Malaspina Pluton and these coeval plutons collectively comprise a rare, natural example of an exhumed transcrustal magmatic system (Cashman *et al.*, 2017) that occupied much of the crust in Fiordland in the Early Cretaceous (see Fig. 1). The presence of highly evolved enriched and depleted melts in the lower crust of this transcrustal magma system highlights the fact that andesitic to dacitic melts with middle to upper continental crust characteristics were the dominant melt composition during construction of the lower crust. Our results demonstrate that the lower crust of Cordilleran arcs is a key location in the diversification of arc melts and the production of continental crust.

CONCLUSIONS

Igneous amphibole data from the lower crust of the Median Batholith reveal the magmatic structure of a deep-crustal MASH or hot zone and document the construction of continental crust during a magmatic flare up. We find the following.

1. Lower-crustal melts were emplaced as a series of sheets that were fed by multiple feeder zones. Melts consist of two geochemical groups consisting of trace-element 'depleted' and 'enriched' melt groups. Amphiboles in both groups were in equilibrium with andesitic to dacitic melts and crystallized over ∼100 °C from ∼960 to 830 °C. Trace-element data show little evidence for extensive fractionation at the level of emplacement; therefore, geochemical diversification must have occurred prior to emplacement in deeper melt reservoirs below the Malaspina Pluton, in either the lower crust or upper mantle.
2. The geochemical diversity of melts and the wide range of crystallization temperatures and trace-element compositions indicates that melts were not well mixed and instead were emplaced as discrete sheets into a crystal-mush zone with limited to no long-range geochemical connectivity. Our data do not support widespread trace-element homogenization in the lower crust of the Median Batholith.
3. Depleted-group melts are defined by low HFSE and LREE concentrations. Relative to N-MORB, they display pronounced enrichments in fluid-mobile elements (e.g. K, Ba, Sr), and probably represent highly fractionated, hydrous mantle-wedge melts enriched by a sediment-derived fluid-rich component.
4. Enriched-group melts show strong enrichment in HFSE, indicating the presence of a crustal component. Elevated Th and Zr concentrations suggest that sediment melt was involved in the petrogenesis of the enriched-melt group.
5. Neither melt group shows geochemical evidence for significant garnet as a fractionating or residual phase. Phase-equilibria data suggest that Malaspina melts were emplaced at $\leq$1·0 GPa, and there is no evidence for the production of a significant garnet-rich mafic root via fractional crystallization or partial melting.

6. Bulk-rock Sr- and Nd-isotope data for the enriched and depleted groups are remarkably homogeneous and show no apparent difference between enriched ($\varepsilon Nd_i = 0{\cdot}1$ to $-0{\cdot}1$; $^{87}Sr/^{86}Sr_i = 0{\cdot}70420$–$0{\cdot}70413$) and depleted groups ($\varepsilon Nd_i = 0{\cdot}3$ to $-0{\cdot}4$; $^{87}Sr/^{86}Sr_i = 0{\cdot}70424$–$0{\cdot}70411$). These data point to a common isotopic source for both groups and suggest that isotope homogenization occurred prior to emplacement in the lower crust and not at the level of emplacement.
7. We speculate that isotope similarities in bulk-rock data reflect hybridization between mantle-wedge melts and a fluid-rich, subducted sediment source. We attribute variations in trace-element abundances in the depleted- and enriched-melt groups to relative contributions of sediment–fluid in the depleted group, and sediment–melt in the enriched-melt group.
8. Malaspina bulk-rocks and calculated amphibole-equilibrium melts show large discrepancies in major- and trace-element compositions. We attribute these differences to accumulation of plagioclase + amphibole + clinopyroxene in bulk-rocks, and we conclude that bulk-rocks poorly approximate melt compositions and therefore should be used with caution in modeling melt evolution in lower-crustal arc rocks.
9. Compared with estimates for continental crust, Malaspina bulk-rock compositions are similar to average lower continental crust values, implying that crystal accumulation of lower-crustal melts hybridized with subducted sediment can generate bulk lower continental crust compositions. In contrast, amphibole-equilibrium melts are more evolved than lower continental crust values, and they generally approximate average middle continental crust estimates. We speculate that extraction of andesitic to dacitic melts from the lower crust resulted in the emplacement of tonalitic to granodioritic plutons that make up the bulk of the middle and upper crust in Fiordland.

ACKNOWLEDGEMENTS

We thank Mandy and Richard Abernethy (Fiordland Expeditions), and Seán Ellis and Maria Kuster (Pure Salt) for assistance with sampling. The New Zealand Department of Conservation, Te Anau office is also thanked for allowing access and sampling in Fiordland. Jade Star Lackey and Jonathan Harris are thanked for assistance with XRF analyses. Zhan Peng is thanked for LA-ICP-MS assistance. Reviews by James Scott, Antonio Acosta-Vigil and an anonymous reviewer significantly improved the paper.

FUNDING

Financial support for this project was provided by the National Science Foundation grant EAR-40015228 to J.J.S.

SUPPLEMENTARY DATA

Supplementary data are available at *Journal of Petrology* online.

REFERENCES

Adams, C. J., Pankhurst, R. J., Maas, R. & Millar, I. L. (2005). Nd and Sr isotopic signatures of metasedimentary rocks around the South Pacific margin and implications for their provenance. In: Vaughan, A. P. M., Leat, P. T., Pankhurst, R. J. (eds.). *Terrane processes at the margins of Gondwana, London*, Geological Society of London, 113–141.

Allibone, A. H., Turnbull, I. M., Tulloch, A. J. & Cooper, A. F. (2007). Plutonic rocks of the Median Batholith in southwest Fiordland, New Zealand: Field relations, geochemistry, and correlation. *New Zealand Journal of Geology and Geophysics* **50**, 283–314.

Allibone, A. H., Jongens, R., Turnbull, I. M., Milan, L. A., Daczko, N. R., De Paoli, M. C. & Tulloch, A. J. (2009a). Plutonic rocks of western Fiordland, New Zealand: Field relations, geochemistry, correlation, and nomenclature. *New Zealand Journal of Geology and Geophysics* **52**, 379–415.

Allibone, A. H., Milan, L. A., Daczko, N. R. & Turnbull, I. M. (2009b). Granulite facies thermal aureoles and metastable amphibolite facies assemblages adjacent to the Western Fiordland Orthogneiss in southwest Fiordland, New Zealand. *Journal of Metamorphic Geology* **27**, 349–369.

Alonso-Perez, R., Müntener, O. & Ulmer, P. (2009). Igneous garnet and amphibole fractionation in the roots of island arcs: Experimental constraints on andesitic liquids. *Contributions to Mineralogy and Petrology* **157**, 541–558.

Anderson, J. L. & Smith, D. R. (1995). The effects of temperature and fO_2 on the Al-in-hornblende barometer. *American Mineralogist* **80**, 549–559.

Annen, C. & Sparks, R. S. J. (2002). Effects of repetitive emplacement of basaltic intrusions on thermal evolution and melt generation in the crust. *Earth and Planetary Science Letters* **203**, 937–955.

Annen, C., Blundy, J. D. & Sparks, R. S. J. (2006). The genesis of intermediate and silicic magmas in deep crustal hot zones. *Journal of Petrology* **47**, 505–539.

Atherton, M. P. & Petford, N. (1993). Generation of sodium-rich magmas from newly underplated basaltic crust. *Nature* **362**, 144–146.

Ayers, J. C., Dittmer, S. K. & Layne, G. D. (1997). Partitioning of elements between peridotite and H_2O at 2·0–3·0 GPa and 900–1100 °C, and application to models of subduction zone processes. *Earth and Planetary Science Letters* **150**, 381–398.

Baker, D. R. & Eggler, D. H. (1983). Fractionation paths of Atka (Aleutians) high-alumina basalts: Constraints from phase relations. *Journal of Volcanology and Geothermal Research* **18**, 387–404.

Baker, D. R. & Eggler, D. H. (1987). Compositions of anhydrous and hydrous melts coexisting with plagioclase, augite, and olivine or low-Ca pyroxene from 1 atm to 8 kbar: Application to the Aleutian volcanic center of Atka. *American Mineralogist* **72**, 12–28.

Barboni, M., Annen, C. & Schoene, B. (2015). Evaluating the construction and evolution of upper crustal magma reservoirs with coupled U/Pb zircon geochronology and thermal modeling: A case study from the Mt. Capanne pluton (Elba, Italy). *Earth and Planetary Science Letters* **432**, 436–448.

Barnes, C. G., Ernst, W. G., Berry, R. & Tsujimori, T. (2016a). Petrology and geochemistry of an upper crustal pluton: a

view into crustal-scale magmatism during arc to retro-arc transition. *Journal of Petrology* **57**, 1361–1388.

Barnes, C. G., Memeti, V. & Coint, N. (2016b). Deciphering magmatic processes in calc-alkaline plutons using trace element zoning in hornblende. *American Mineralogist* **101**, 328–342.

Barnes, C. G., Berry, R., Barnes, M. A. & Ernst, W. G. (2017). Trace element zoning in hornblende: tracking and modeling the crystallization of a calc-alkaline arc pluton. *American Mineralogist* **102**, 2390–2405.

Barnes, C. G., Werts, K., Memeti, V. & Ardill, K. (2020). Most granitoid rocks are cumulates: deductions from hornblende compositions, and zircon saturation. *Journal of Petrology* 1–25.

Begemann, F., Ludwig, K. R., Lugmair, G. W., Min, K., Nyquist, L. E., Patchett, P. J., Renne, P. R., Shih, C.-Y., Villa, I. M. & Walker, R. J. (2001). Call for an improved set of decay constants for geochronological use. *Geochimica et Cosmochimica Acta* **65**, 111–121.

Bergantz, G. W. (1992). Conjugate solidification and melting in multicomponent open and closed systems. *International Journal of Heat and Mass Transfer* **35**, 533–543.

Bergantz, G. W. (2000). On the dynamics of magma mixing by reintrusion: implications for pluton assembly processes. *Journal of Structural Geology* **22**, 1297–1309.

Betka, P. M. & Klepeis, K. A. (2013). Three-stage evolution of lower crustal gneiss domes at Breaksea Entrance, Fiordland, New Zealand. *Tectonics* **32**, 1084–1106.

Blatter, D. L., Sisson, T. W. & Hankins, W. B. (2017). Voluminous arc dacites as amphibole reaction-boundary liquids. *Contributions to Mineralogy and Petrology* **172**, 1–37.

Blundy, J. D. & Holland, T. J. B. (1990). Calcic amphibole equilibria and a new amphibole-plagioclase geothermometer. *Contributions to Mineralogy and Petrology* **104**, 208–224.

Bowen, N. L. (1929). The Evolution of Igneous Rocks. *Nature* **124**, 474–475.

Brackman, A. J., Schwartz, J. J. & Carty, K. (2019). Evaluating High Sr/Y Geochemical Signature in Lower-Arc Crust Using Pyroxene Major and Trace Element. *Geological Society of America Abstracts with Programs* **51**, doi: 10.1130/abs/2019AM-340647

Bradshaw, J. Y. (1989). Origin and metamorphic history of an Early Cretaceous polybaric granulite terrain, Fiordland, southwest New Zealand. *Contributions to Mineralogy and Petrology* **103**, 346–360.

Bradshaw, J. Y. (1990). Geology of crystalline rocks of northern Fiordland: details of the granulite facies Western Fiordland Orthogneiss and associated rock units. *New Zealand Journal of Geology and Geophysics* **33**, 465–484.

Brenan, J. M., Shaw, H. F. & Ryerson, F. J. (1995a). Experimental evidence for the origins of lead enrichment in convergent-margin magmas. *Nature* **378**, 54–56.

Brenan, J. M., Shaw, H. F., Ryerson, F. J. & Phinney, D. L. (1995b). Mineral–aqueous fluid partitioning of trace elements at 900 °C and 2·0 GPa: Constraints on the trace element chemistry of mantle and deep crustal fluids. *Geochimica et Cosmochimica Acta* **59**, 3331–3350.

Brenan, J. M., Shaw, H. F., Ryerson, F. J. & Phinney, D. L. (1996). Erratum to "Experimental determination of trace-element partitioning between pargasite and a synthetic hydrous andesitic melt". *Earth and Planetary Science Letters* **140**, 287–288.

Brophy, J. G. & Marsh, B. D. (1986). On the origin of high-alumina arc basalt and the mechanics of melt extraction. *Journal of Petrology* **27**, 763–789.

Buriticá, L. F., Schwartz, J. J., Klepeis, K. A., Miranda, E. A., Tulloch, A. J., Coble, M. A. & Kylander-Clark, A. R. C. (2019). Temporal and spatial variations in magmatism and transpression in a Cretaceous arc, Median Batholith, Fiordland, New Zealand. *Lithosphere* **11**, 652–682.

Caricchi, L., Annen, C., Rust, A. & Blundy, J. D. (2012). Insights into the mechanisms and timescales of pluton assembly from deformation patterns of mafic enclaves. *Journal of Geophysical Research B: Solid Earth* **117**, 1–18.

Carmichael, I. S. E. (1991). The redox states of basic and silicic magmas: a reflection of their source regions? *Contributions to Mineralogy and Petrology* **106**, 129–141.

Carmichael, I. S. E. (2002). The andesite aqueduct: perspectives on the evolution of intermediate magmatism in west–central (105–99°W) Mexico. *Contributions to Mineralogy and Petrology* **143**, 641–663.

Cashman, K. V., Sparks, R. S. J. & Blundy, J. D. (2017). Vertically extensive and unstable magmatic systems: a unified view of igneous processes. *Science* **355**, eaag3055.

Chapman, T., Clarke, G. L., Daczko, N. R., Piazolo, S. & Rajkumar, A. (2015). Orthopyroxene–omphacite and garnet–omphacite-bearing magmatic assemblages, Breaksea Orthogneiss, New Zealand: oxidation state controlled by high-*P* oxide fractionation. *Lithos* **216–217**, 1–16.

Chapman, T., Clarke, G. L. & Daczko, N. R. (2016). Crustal differentation in a thickened arc—evaluating depth dependences. *Journal of Petrology* **57**, 595–620.

Chapman, T., Clarke, G.L., Piazolo, S., and Daczko, N.. (2017). Evaluating the importance of metamorphism in the foundering of continental crust. *Scientific Reports* **7**, 13039, https://doi .org/10.1038/s41598-017-13221-6.

Chappell, B. W. & White, A. J. R. (2001). Two contrasting granite types: 25 years later. *Australian Journal of Earth Sciences* **48**, 489–499.

Clarke, G. L., Daczko, N. R. & Miescher, D. (2013). Identifying relic igneous garnet and clinopyroxene in eclogite and granulite, Breaksea Orthogneiss, New Zealand. *Journal of Petrology* **54**, 1921–1938.

Clarke, G. L., Daczo, N. R., Klepeis, K. A. & Rushmer, T. (2005). Roles for fluid and/or melt advection in forming high-P mafic migmatites, Fiordland, New Zealand. *Journal of Metamorphic Geology* **23**, 557–567.

Coint, N., Barnes, C. G., Yoshinobu, A. S., Barnes, M. A. & Buck, S. (2013a). Use of trace element abundances in augite and hornblende to determine the size, connectivity, timing, and evolution of magma batches in a tilted batholith. *Geosphere* **9**, 1747–1765.

Coint, N., Barnes, C. G., Yoshinobu, A. S., Chamberlain, K. R. & Barnes, M. A. (2013b). Batch-wise assembly and zoning of a tilted calc-alkaline batholith: Field relations, timing, and compositional variation. *Geosphere* **9**, 1729–1746.

Collins, W. J., Murphy, B., Johnson, T. E. & Huang, H.-Q. (2020). Critical role of water in the formation of continental crust. *Nature Geoscience* **13**, 331–338.

Czertowicz, T. A., Scott, J. M., Waight, T. E., Palin, J. M., Van der Meer, Q. H. A., Le Roux, P., Münker, C. & Piazolo, S. (2016). The Anita Peridotite, New Zealand: ultra-depletion and subtle enrichment in sub-arc mantle. *Journal of Petrology* **57**, 717–750.

Daczko, N. R., Klepeis, K. A. & Clarke, G. L. (2001). Evidence of early Cretaceous collisional-style orogenesis in Northern Fiordland, New Zealand and its effects on the evolution of the lower crust. *Journal of Structural Geology* **23**, 693–713.

Daczko, N. R., Klepeis, K. A. & Clarke, G. L. (2002). Thermomechanical evolution of the crust during convergence and deep crustal pluton emplacement in the western province of Fiordland. *Tectonics* **21**, 4–1–4-18.

Daczko, N. R., Milan, L. A. & Halpin, J. A. (2009). Metastable persistence of pelitic metamorphic assemblages at the root of a

Cretaceous magmatic arc—Fiordland, New Zealand. *Journal of Metamorphic Geology* **27**, 233–247.

Davids, C. (1999). *A Thermochronological Study of Southern Fiordland, New Zealand*. Canberra, ACT: Australian National University.

Davidson, J. P., Turner, S., Handley, H., Macpherson, C. G. & Dosseto, A. (2007). Amphibole "sponge" in arc crust? *Geology* **35**, 787–790.

Decker, M. F. I., Schwartz, J. J., Stowell, H. H., Klepeis, K. A., Tulloch, A. J., Kitajima, K., Valley, J. W. & Kylander-Clark, A. R. C. (2017). Slab-triggered arc flare-up in the Cretaceous Median Batholith and the growth of lower arc crust, Fiordland, New Zealand. *Journal of Petrology* **58**, 1145–1171.

Defant, M. J. & Drummond, M. S. (1990). Derivation of some modern arc magmas by melting of young subducted lithosphere. *Nature* **347**, 662–665.

De Paoli, M. C., Clarke, G. L., Klepeis, K. A., Allibone, A. H. & Turnbull, I. M. (2009). The eclogite–granulite transition: mafic and intermediate assemblages at Breaksea Sound, New Zealand. *Journal of Petrology* **50**, 2307–2343.

Ducea, M. N., Bergantz, G. W., Crowley, J. L. & Otamendi, J. (2017). Ultrafast magmatic buildup and diversification to produce continental crust during subduction. *Geology* **45**, 235–238.

Dufek, J. & Bergantz, G. W. (2005). Lower crustal magma genesis and preservation: A stochastic framework for the evaluation of basalt-crust interaction. *Journal of Petrology* **46**, 2167–2195.

Edmonds, M., Cashman, K. V., Holness, M. & Jackson, M. D. (2019). Architecture and dynamics of magma reservoirs. *Philosophical Transactions of the Royal Society of London, Series A* **377**, 1–29.

Esawi, E. K. (2004). AMPH-CLASS: An Excel spreadsheet for the classification and nomenclature of amphiboles based on the 1997 recommendations of the International Mineralogical Association. *Computers & Geosciences* **30**, 753–760.

Ferry, J. M. & Watson, E. B. (2007). New thermodynamic models and revised calibrations for the Ti-in-zircon and Zr-in-rutile thermometers. *Contributions to Mineralogy and Petrology* **154**, 429–437.

Gazel, E., Hayes, J. L., Hoernle, K., Kelemen, P., Everson, E., Holbrook, W. S., Hauff, F., van den Bogaard, P., Vance, E. A., Chu, S., Calvert, A. J., Carr, M. J. & Yogodzinski, G. M. (2015). Continental crust generated in oceanic arcs. *Nature Geoscience* **8**, 321–327.

Gibson, G. M. (1992). Medium–high-pressure metamorphic rocks of the Tuhua Orogen, western New Zealand, as lower crustal analogues of the Lachlan Fold Belt. *Tectonophysics* **214**, 145–157.

Gibson, G. M. & Ireland, T. R. (1995). Granulite formation during continental extension in Fiordland, New Zealand. *Nature* **375**, 479–482.

Gill, J. (1981). *Orogenic Andesites and Plate Tectonics*. Berlin: Springer, 390 pp.

Glazner, A. F., Bartley, J. M., Coleman, D. S., Gray, W. & Taylor, R. Z. (2004). Are plutons assembled over millions of years by amalgamation from small magma chambers? *GSA Today* **5173**, 4–11.

Graham, I. J., Gulson, B. L., Hedenquist, J. W. & Mizon, K. (1992). Petrogenesis of Late Cenozoic volcanic rocks from the Taupo Volcanic Zone, New Zealand, in the light of new lead isotope data. Geochimica et *Cosmochimica Acta* **56**, 2797–2819.

Green, D. H. (1971). Composition of basaltic magmas as indicators of conditions of origin: application to oceanic volcanism. *Philosophical Transactions of the Royal Society of London* **268**, 707–725.

Grove, T. L. & Kinzler, R. J. (1986). Petrogenesis of Andesites. *Annual Review of Earth and Planetary Sciences* **14**, 417–454.

Grove, T. L., Gerlach, D. C. & Sando, T. W. (1982). Origin of calc-alkaline series lavas at Medicine Lake Volcano by fractionation, assimilation and mixing. *Contributions to Mineralogy and Petrology* **80**, 160–182.

Grove, T., Parman, S., Bowring, S., Price, R. & Baker, M. (2002). The role of an H_2O-rich fluid component in the generation of primitive basaltic andesites and andesites from the Mt. Shasta region, N California. *Contributions to Mineralogy and Petrology* **142**, 375–396.

Grove, T. L., Elkins-Tanton, L. T., Parman, S. W., Chatterjee, N., Müntener, O. & Gaetani, G. A. (2003). Fractional crystallization and mantle-melting controls on calc-alkaline differentiation trends. *Contributions to Mineralogy and Petrology* **145**, 515–533.

Hacker, B. R., Kelemen, P. B. & Behn, M. D. (2011). Differentiation of the continental crust by relamination. *Earth and Planetary Science Letters* **307**, 501–516.

Hamelin, C., Dosso, L., Hanan, B., Barrat, J. A. & Ondréas, H. (2010). Sr–Nd–Hf isotopes along the Pacific Antarctic Ridge from 41 to 53°S. *Geophysical Research Letters* **37**. doi: 10.1029/2010GL042979.

Hammarstrom, J. M. & E-an Zen E. (1986). Aluminum in hornblende: An empirical igneous geobarometer. *American Mineralogist* **71**, 1297–1313.

Hawkesworth, C. J. & Kemp, A. I. S. (2006). Evolution of the continental crust. *Nature* **443**, 811–817.

Hawkesworth, C. J., Kempton, P. D., Rogers, N. W., Ellam, R. M. & van Calsteren, P. W. (1990). Continental mantle lithosphere, and shallow level enrichment processes in the Earth's mantle. *Earth and Planetary Science Letters* **96**, 256–268.

Hermann, J. & Rubatto, D. (2009). Accessory phase control on the trace element signature of sediment melts in subduction zones. *Chemical Geology* **265**, 512–526.

Hildreth, W. & Moorbath, S. (1988). Crustal contributions to arc magmatism in the Andes of Central Chile. *Contributions to Mineralogy and Petrology* **98**, 455–489.

Hirose, K. (1997). Melting experiments on lherzolite KLB-1 under hydrous conditions and generation of high-magnesian andesitic melts. *Geology* **25**, 42–44.

Hirose, K. & Kawamoto, T. (1995). Hydrous partial melting of lherzolite at 1 GPa: The effect of H_2O on the genesis of basaltic magmas. *Earth and Planetary Science Letters* **133**, 463–473.

Hollis, J. A., Clarke, G. L., Klepeis, K. A., Daczko, N. R. & Ireland, T. R. (2004). The regional significance of Cretaceous magmatism and metamorphism in Fiordland, New Zealand, from U–Pb zircon geochronology. *Journal of Metamorphic Geology* **22**, 607–627. doi:10.1111/j.1525-1314.2004.00537.x

Hollister, L. S., Grissom, G. C., Peters, E. K., Stowell, H. H. & Sisson, V. B. (1987). Confirmation of the empirical correlation of Al in hornblende with pressure of solidification of calc-alkaline plutons. *American Mineralogist* **72**, 231–239.

Izbekov, P., Gardner, J. E. & Eichelberger, J. C. (2004). Comagmatic granophyre and dacite from Karymsky volcanic center, Kamchatka: experimental constraints for magma storage conditions. *Journal of Volcanology and Geothermal Research* **131**, 1–18.

Johnson, M. C. & Plank, T. (1999). Dehydration and melting experiments constrain the fate of subducted sediments. *Geochemistry, Geophysics, Geosystems* **1**, 1–26.

Johnson, M. C. & Rutherford, M. J. (1989). Experimental calibration of the aluminium-in-hornblende geobarometer with application to Long Valley caldera. *Geology* **17**, 837–841.

Johnston, A. D. & Wyllie, P. J. (1988). Constraints on the origin of Archean trondhjemites based on phase relationships of Nûk gneiss with H_2O at 15 kbar. *Contributions to Mineralogy and Petrology* **100**, 35–46.

Kelemen, P. B. (1995). Genesis of high Mg# andesites and the continental crust. *Contributions to Mineralogy and Petrology* **120**, 1–19.

Kelemen, P. B., Joyce, D. B., Webster, J. D. & Holloway, J. R. (1990). Reaction Between Ultramafic Rock and Fractionating Basaltic Magma II. Experimental Investigation of Reaction Between Olivine Tholeiite and Harzburgite at 1150–1050 °C and 5 kb. *Journal of Petrology* **31**, 99–134.

Kelemen, P. B., Hanghøj, K. & Greene, A. R. (2014). One View of the Geochemistry of Subduction-Related Magmatic Arcs, with an Emphasis on Primitive Andesite and Lower Crust. In: Roberta L. Rudnick (ed.) *Treatiseon Geochemistry*, **4**. Amsterdam: Elsevier, pp. 749–806.

Kimura, J. I., Kent, A. J., Rowe, M. C., Katakuse, M., Nakano, F., Hacker, B. R., van Keken, P. E., Kawabata, H. & Stern, R. J. (2010). Origin of cross-chain geochemical variation in Quaternary lavas from the northern Izu arc: Using a quantitative mass balance approach to identify mantle sources and mantle wedge processes. *Geochemistry, Geophysics, Geosystems* **11**. doi:10.1029/2010GC003050.

Klein, M., Stosch, H.-G. & Seck, H. A. (1997). Partitioning of high field-strength and rare-earth elements between amphibole and quartz-dioritic to tonalitic melts: An experimental study. *Chemical Geology* **138**, 257–271.

Klepeis, K. A., Clarke, G. L., Gehrels, G. & Vervoort, J. (2004). Processes controlling vertical coupling and decoupling between the upper and lower crust of orogens: results from Fiordland, New Zealand. *Journal of Structural Geology* **26**, 765–791. doi:10.1029/2006TC002003.

Klepeis, K. A., Schwartz, J. J., Stowell, H. H. & Tulloch, A. J. (2016). Gneiss domes, vertical and horizontal mass transfer, and the initiation of extension in the hot lower-crustal root of a continental arc, Fiordland, New Zealand. *Lithosphere* **8**, 116–140.

Kogiso, T., Tatsumi, Y. & Nakano, S. (1997). Trace element transport during dehydration processes in the subducted oceanic crust: 1. Experiments and implications for the origin of ocean island basalts. *Earth and Planetary Science Letters* **148**, 193–205.

Lackey, J. S., Cecil, M. R., Windham, C. J., Frazer, R. E., Bindeman, I. N. & Gehrels, G. E. (2012). The Fine Gold Intrusive Suite: The roles of basement terranes and magma source development in the Early Cretaceous Sierra Nevada batholith. *Geosphere* **8**, 292–313.

Leake, B. E. (1997). Nomenclature of Amphiboles: Report of The Subcommittee on Amphiboles of The International Mineralogical Association, Commission on New Minerals and Mineral Names. *Canadian Mineralogist* **35**, 219–246.

Leake, b. E. et al. (1997). Nomenclature of amphiboles: report of the subcommittee on amphiboles of the international mineralogical association, commission on new minerals and mineral names. *The Canadian Mineralogist* **35**, 219–246.

Marcotte, S. B., Klepeis, K. A., Clarke, G. L., Gehrels, G. E. & Hollis, J. A. (2005). Intra-arc transpression in the lower crust and its relationship to magmatism in a Mesozoic magmatic arc. *Tectonophysics* **407**, 135–163.

Marsh, B. D. (1976). Some Aleutian Andesites: Their Nature and Source. *Journal of Geology* **84**, 27–45.

Mattinson, J. M., Kimbrough, D. L. & Bradshaw, J. Y. (1986). Western Fiordland orthogneiss: Early Cretaceous arc magmatism and granulite facies metamorphism, New Zealand. *Contributions to Mineralogy and Petrology* **92**, 383–392.

Mazzucchelli, M., Rivalenti, G., Vannucci, R., Bottazzi, P., Ottolini, L., Hofmann, A. W. & Parenti, M. (1992). Primary positive Eu anomaly in clinopyroxenes of low-crust gabbroic rocks. *Geochimica et Cosmochimica Acta* **56**, 2363–2370.

McCulloch, M. T., Bradshaw, J. Y. & Taylor, S. R. (1987). Sm–Nd and Rb–Sr isotopic and geochemical systematics in Phanerozoic granulites from Fiordland, southwest New Zealand. *Contributions to Mineralogy and Petrology* **97**, 183–195.

Memeti, V., Paterson, S. R., Matzel, J., Mundil, R. & Okaya, D. (2010). Magmatic lobes as "snapshots" of magma chamber growth and evolution in large, composite batholiths: An example from the Tuolumne intrusion, Sierra Nevada, California. *Geological Society of America Bulletin* **122**, 1912–1931.

Milan, L. A., Daczko, N. R., Clarke, G. L. & Allibone, A. H. (2016). Complexity of *in-situ* zircon U–Pb–Hf isotope systematics during arc magma genesis at the roots of a Cretaceous arc, Fiordland, New Zealand. *Lithos* **264**, 296–314.

Milan, L. A., Daczko, N. R. & Clarke, G. L. (2017). Cordillera Zealandia: a Mesozoic arc flare-up on the palaeo-Pacific Gondwana margin. *Science Reports* **7**, doi:10.1038/s41598-017-00347-w.

Miller, C. F., Furbish, D. J., Walker, B. A., Claiborne, L. L., Koteas, G. C., Bleick, H. A. & Miller, J. S. (2011). Growth of plutons by incremental emplacement of sheets in crystal-rich host: Evidence from Miocene intrusions of the Colorado River region, Nevada, USA. *Tectonophysics* **500**, 65–77.

Miranda, E. A. & Klepeis, K. A. (2016). The interplay and effects of deformation and crystallized melt on the rheology of the lower continental crust, Fiordland, New Zealand. *Journal of Structural Geology* **93**, 91–105.

Mortimer, N., Tulloch, A. J., Spark, R. N., Walker, N. W., Ladley, E. B., Allibone, A. H. & Kimbrough, D. L. (1999). Overview of the Median Batholith, New Zealand: A new interpretation of the geology of the Median Tectonic Zone and adjacent rocks. *Journal of African Earth Sciences* **29**, 257–268.

Muir, R. J., Weaver, S. D., Bradshaw, J. D., Eby, G. N. & Evans, J. A. (1995). The Cretaceous Separation Point batholith, New Zealand: granitoid magmas formed by melting of mafic lithosphere. *Journal of the Geological Society, London* **152**, 689–701.

Müntener, O. & Ulmer, P. (2006). Experimentally derived high-pressure cumulates from hydrous arc magmas and consequences for the seismic velocity structure of lower arc crust. *Geophysical Research Letters* **33**. doi: 10.1029/2006GL027629.

Müntener, O., Kelemen, P. B. & Grove, T. L. (2001). The role of H_2O during crystallization of primitive arc magmas under uppermost mantle conditions and genesis of igneous pyroxenites: an experimental study. *Contributions to Mineralogy and Petrology* **141**, 643–658.

Musselwhite, D. S., DePaolo, D. J. & McCurry, M. (1989). The evolution of a silicic magma system: isotopic and chemical evidence from the Woods Mountains Volcanic Center, eastern California. *Contributions to Mineralogy and Petrology* **101**, 19–29.

Myers, J. D., Marsh, B. D. & Sinha, A. K. (1985). Strontium isotopic and selected trace element variations between two Aleutian volcanic centers (Adak and Atka): implications for

the development of arc volcanic plumbing systems. *Contributions to Mineralogy and Petrology* **91**, 221–234.

Myers, J. D., Frost, C. D. & Angevine, C. L. (1986a). A Test of a Quartz Eclogite Source for Parental Aleutian Magmas: A Mass Balance Approach. *Journal of Geology* **94**, 811–828.

Myers, J. D., Marsh, B. D. & Sinha, A. K. (1986b). Geochemical and strontium isotopic characteristics of parental Aleutian Arc magmas: evidence from the basaltic lavas of Atka. *Contributions to Mineralogy and Petrology* **94**, 1–11.

Nandedkar, R. H., Hürlimann, N., Ulmer, P. & Müntener, O. (2016). Amphibole–melt trace element partitioning of fractionating calc-alkaline magmas in the lower crust: an experimental study. *Contributions to Mineralogy and Petrology* **171**, 1–25.

Oliver, G. J. H. (1976). *High Grade Metamorphic Rocks of Doubtful Sound, Fiordland, New Zealand: A Study of the Lower Crust*. PhD Thesis. University of Otago, Dunedin, New Zealand.

Oliver, G. J. H. (1977). Feldspathic hornblende and garnet granulites and associated anorthosite pegmatites from Doubtful Sound, Fiordland, New Zealand. *Contributions to Minera logy and Petrology* **65**, 111–121.

Oliver, G. J. H. (1980). Geology of the granulite and amphibolite facies gneisses of Doubtful Sound, Fiordland, New Zealand. *New Zealand Journal of Geology and Geophysics* **23**, 27–41.

Paterson, S. R., Memeti, V., Mundil, R. & Zák, J. (2016). Repeated, multiscale, magmatic erosion and recycling in an upper-crustal pluton: Implications for magma chamber dynamics and magma volume estimates. *American Mineralogist* **101**, 2176–2198.

Paton, C., Hellstrom, J., Paul, B., Woodhead, J. & Hergt, J. (2011). Iolite: Freeware for the visualisation and processing of mass spectrometric data. *Journal of Analytical Atomic Spectrometry* **26**, 2508–2518.

Pearce, J. A. (1983). Role of the sub-continental lithosphere in magma genesis at active continental margins. In: Hawkesworth, C. J. & Norry, M. J. (eds) *Continental Basalts and Mantle Xenoliths*. Nantwich: Shiva, pp. 230–249.

Petford, N. & Atherton, M. (1996). Na-rich Partial Melts from Newly Underplated Basaltic Crust: the Cordillera Blanca Batholith, Peru. *Journal of Petrology* **37**, 1491–1521.

Petford, N. & Gallagher, K. (2001). Partial melting of mafic (amphibolitic) lower crust by periodic influx of basaltic magma. *Earth and Planetary Science Letters* **193**, 483–499.

Plank, T. (2005). Constraints from thorium/lanthanum on sediment recycling at subduction zones and the evolution of the continents. *Journal of Petrology* **46**, 921–944.

Putirka, K. D. (2016). Amphibole thermometers and barometers for igneous systems and some implications for eruption mechanisms of felsic magmas at arc volcanoes. *American Mineralogist* **101**, 841–858.

Rapp, R. P., Shimizu, N., Norman, M. D. & Applegate, G. S. (1999). Reaction between slab-derived melts and peridotite in the mantle wedge: Experimental constraints at 3·8 GPa. *Chemical Geology* **160**, 335–356.

Rapp R. P., Watson, E. B. (1995). Dehydration Melting of Metabasalt at 8–32 kbar: Implications for Continental Growth and Crust-Mantle Recycling, *Journal of Petrology* **36**, 891–931, https://doi.org/10.1093/petrology/36.4.891.

Reubi, O. & Blundy, J. D. (2009). A dearth of intermediate melts at subduction zone volcanoes and the petrogenesis of arc andesites. *Nature* **461**, 1269–1273.

Ringwood, M., Schwartz, J. J., Turnbull, R. E. & Tulloch, A. J. (2021). Phanerozoic Record of mantle-dominated arc magmatic surges in the Zealandia Cordillera. *Geology*, doi: 10.1130/G48916.1.

Roeder, P. L. & Emslie, R. F. (1970). Olivine–Liquid Equilibrium. *Contributions to Mineralogy and Petrology* **29**, 275–289.

Rogers, G. & Hawkesworth, C. J. (1989). A geochemical traverse across the North Chilean Andes: evidence for crust generation from the mantle wedge. *Earth and Planetary Science Letters* **91**, 271–285.

Rudnick, R. L. (1995). Making continental crust. *Nature* **378**, 571–578.

Rudnick, R. L. & Gao, S. (2003). Composition of the Continental Crust. In: *Treatise on Geochemistry*, **3**. Amsterdam: Elsevier, pp. 1–64.

Rudnick, R. L. & Gao, S. (2013). Composition of the Continental Crust. In: Holland, H. D. & Turekian, K. K. (eds) *Treatise on Geochemistry*, 2nd edn. Amsterdam: Elsevier, pp. 1–51.

Schmidt, M. W. (1992). Amphibole composition in tonalite as a function of pressure: an experimental calibration of the Al-in-hornblende barometer. *Contributions to Mineralogy and Petrology* **110**, 304–310.

Schnetzler, C. C. & Philpotts, J. A. (1970). Partition coefficients of rare-earth elements between igneous matrix material and rock-forming mineral phenocrysts—II. *Geochimica et Cosmochimica Acta* **34**, 331–340.

Schwartz, J. J., Stowell, H. H., Klepeis, K. A., Tulloch, A. J., Kylander-Clark, A. R. C., Hacker, B. R. & Coble, M. A. (2016). Thermochronology of extensional orogenic collapse in the deep crust of Zealandia. *Geosphere* **12**, 647–677.

Schwartz, J. J., Klepeis, K. A., Sadorski, J. F., Stowell, H. H., Tulloch, A. J. & Coble, M. A. (2017). The tempo of continental arc construction in the Mesozoic Median Batholith, Fiordland, New Zealand. *Lithosphere* **9**, 343–365.

Schwartz, J. J., Andico, S., Turnbull, R., Klepeis, K. A., Tulloch, A. J., Kitajima, K. & Valley, J. (2021). Stable and Transient Isotopic Trends in the Crustal Evolution of Zealandia Cordillera. *American Mineralogist* **106**, 1369–1387, doi: 10.2138/am-2021-7626.

Scott, J. M., Cooper, A. F., Tulloch, A. J. & Spell, T. L. (2011). Crustal thickening of the Early Cretaceous paleo-Pacific Gondwana margin. *Gondwana Research* **20**, 380–394.

Severs, M. J., Beard, J. S., Fedele, L., Hanchar, J. M., Mutchler, S. R. & Bodnar, R. J. (2009). Partitioning behavior of trace elements between dacitic melt and plagioclase, orthopyroxene, and clinopyroxene based on laser ablation ICPMS analysis of silicate melt inclusions. *Geochimica et Cosmo chimica Acta* **73**, 2123–2141.

Shimizu, K., Liang, Y., Sun, C., Jackson, C. R. M. & Saal, A. E. (2017). Parameterized lattice strain models for REE partitioning between amphibole and silicate melt. *American Mineralogist* **102**, 2254–2267.

Sisson, T. W. & Grove, T. L. (1993a). Experimental investigations of the role of H_2O in calc-alkaline differentiation and subduction zone magmatism. *Contributions to Mineralogy and Petrology* **113**, 143–166.

Sisson, T. W. & Grove, T. L. (1993b). Temperatures and H_2O contents of low-MgO high-alumina basalts. *Contributions to Mineralogy and Petrology* **113**, 167–184.

Smith, D. J. (2014). Clinopyroxene precursors to amphibole sponge in arc crust. *Nature Communications* **5**, 1–6.

Smith, D. R. & Leeman, W. P. (1987). Petrogenesis of Mount St. Helens dacitic magmas. *Journal of Geophysical Research: Solid Earth* **92**, 10313–10334.

Solano, J. M. S., Jackson, M. D., Sparks, R. S. J., Blundy, J. D. & Annen, C. (2012). Melt segregation in Deep Crustal Hot Zones: A Mechanism for Chemical Differentiation, Crustal Assimilation and the Formation of Evolved Magmas. *Journal of Petrology* **53**, 1999–2026.

Stalder, R., Foley, S. F., Brey, G. P. & Horn, I. (1998). Mineral–aqueous fluid partitioning of trace elements at

900–1200 °C and 3·0–5·7 GPa: New experimental data for garnet, clinopyroxene, and rutile, and implications for mantle metasomatism. *Geochimica et Cosmochimica Acta* **62**, 1781–1801.

Stowell, H. H., Parker, K. O., Gatewood, M., Tulloch, A. J. & Koenig, A. (2014). Temporal links between pluton emplacement, garnet granulite metamorphism, partial melting and extensional collapse in the lower crust of a Cretaceous magmatic arc, Fiordland, New Zealand. *Journal of Metamorphic Geology* **32**, 151–175.

Stowell, H. H., Schwartz, J. J., Klepeis, K. A., Hout, C., Tulloch, A. J. & Koenig, A. (2017). Sm–Nd garnet ages for granulite and eclogite in the Breaksea Orthogneiss and widespread granulite facies metamorphism of the lower crust, Fiordland magmatic arc, New Zealand. *Lithosphere* **9**, 953–975.

Stuart, C. A., Daczko, N. R. & Piazolo, S. (2017). Local partial melting of the lower crust triggered by hydration through melt–rock interaction: an example from Fiordland, New Zealand. *Journal of Metamorphic Geology* **35**, 213–230.

Stuart, C. A., Meek, U., Daczko, N. R., Piazolo, S. & Huang, J. X. (2018). Chemical signatures of melt–rock interaction in the root of a magmatic arc. *Journal of Petrology* **59**, 321–340.

Sun, S.-S. & McDonough, W. F. (1989). Chemical and isotopic systematics of oceanic basalts: Implications for mantle composition and processes. In: Saunders, A. D. & Norry, M. J. (eds) *Magmatism in the Ocean Basins. Geological Society, London, Special Publications* **42**, 313–345.

Tatsumi, Y. & Kogiso, T. (1997). Trace element transport during dehydration processes in the subducted oceanic crust: 2. Origin of chemical and physical characteristics in arc magmatism. *Earth and Planetary Science Letters* **148**, 207–221.

Taylor, S. R. & McLennan, S. M. (1985). *The Continental Crust: its Composition and Evolution. An Examination of the Geochemical Record Preserved in Sedimentary Rocks*. Oxford: Blackwell Scientific.

Taylor, S. R. & McLennan, S. M. (1995). The geochemical evolution of the continental crust. *American Geophysical Union* **33**, 241–265. doi:10.1029/95RG00262.

Tepper, J. H., Nelson, B. K., Bergantz, G. W. & Irving, A. J. (1993). Petrology of the Chilliwack batholith, North Cascades, Washington: generation of calc-alkaline granitoids by melting of mafic lower crust with variable water fugacity. *Contributions to Mineralogy and Petrology* **113**, 333–351.

Tulloch, A. J. & Kimbrough, D. L. (2003). Paired plutonic belts in convergent margins and the development of high Sr/Y magmatism: Peninsular Ranges batholith of Baja California and Median batholith of New Zealand. In: Scott E. Johnson, Scott R. Paterson, John M. Fletcher, Gary H. Girty, David L. Kimbrough, Arturo Martín-Barajas (eds.) Tectonic evolution of northwestern Mexico and the Southwestern USA, *Geological Society of America, Special Papers* **374**, 275–295.

Tulloch, A. J., Ramezani, J., Kimbrough, D. L., Faure, K. & Allibone, A. H. (2009). U–Pb geochronology of mid-Paleozoic plutonism in western New Zealand: Implications for S-type granite generation and growth of the east Gondwana margin. *Geological Society of America Bulletin* **121**, 1236–1261.

Turnbull, R. E., Weaver, S., Tulloch, A. J., Cole, J., Handler, M. & Ireland, T. R. (2010). Field and geochemical constraints on mafic–felsic interactions, and processes in high-level arc magma chambers: An example from the Halfmoon Pluton, New Zealand. *Journal of Petrology* **51**, 1477–1505.

Turner, S. J., Langmuir, C. H., Dungan, M. A. & Escrig, S. (2017). The importance of mantle wedge heterogeneity to subduction zone magmatism and the origin of EM1. *Earth and Planetary Science Letters* **472**, 216–228.

Ulmer, P., Kaegi, R. & Müntener, O. (2018). Experimentally derived intermediate to silica-rich arc magmas by fractional and equilibrium crystallization at 1·0 GPa: An evaluation of phase relationships, compositions, liquid lines of descent and oxygen fugacity. *Journal of Petrology* **59**, 11–58.

Vlastelic, I., Aslanian, D., Dosso, L., Bougault, H., Olivet, J. L. & Geli, L. (1999). Large-scale chemical and thermal division of the Pacific mantle. *Nature* **399**, 345–350.

Walker, B. A., Bergantz, G. W., Otamendi, J. E., Ducea, M. N. & Cristofolini, E. A. (2015). A MASH zone revealed: the mafic complex of the Sierra Valle Fértil. *Journal of Petrology* **56**, 1863–1896.

Ward, C. M. (1984). *Geology of the Dusky Sound Area, Fiordland, with Emphasis on the Structural–Metamorphic Development of Some Porphyroblastic Staurolite Pelites*. PhD dissertation. University of Otago.

Watson, E. B. & Harrison, T. M. (1983). Zircon saturation revisited: temperature and composition effects in a variety of crustal magma types. *Earth and Planetary Science Letters* **64**, 295–304.

Werts, K., Barnes, C. G., Memeti, V., Ratschbacher, B., Williams, D. & Paterson, S. R. (2020). Hornblende as a tool for assessing mineral–melt equilibrium and recognition of crystal accumulation. *American Mineralogist* **105**, 77–91.

Whitney, D. L. & Evans, B. W. (2010). Abbreviations for names of rock-forming minerals. *American Mineralogist* **95**, 185–187.

Winter, J. D. (2001). *An Introduction to Igneous and Metamorphic Petrology*. Upper Saddle River, NJ: Prentice Hall, 702 pp.

Zhang, J., Humphreys, M. C. S., Cooper, G. F., Davidson, J. P. & Macpherson, C. G. (2017). Magma mush chemistry at subduction zones, revealed by new melt major element inversion from calcic amphiboles. *American Mineralogist* **102**, 1353–1367.